UQAC
Université du Québec
à Chicoutimi

Development of durable, ecologic and corrosion resistant non-chromate coatings for aluminum

Par

Redouane Farid

Thèse présentée à l'Université du Québec à Chicoutimi en vue de l'obtention du grade de doctorat en ingénierie

Québec, Canada

Development of durable, ecologic and corrosion resistant non-chromate coatings for aluminum

Ph.D. Thesis

Redouane Farid

University of Quebec At Chicoutimi

Jury

Dr. Dilip Kumar Sarkar (Director)	University of Quebec At Chicoutimi
Dr. Saleema Noormohammed (Examiner)	National Research Council of Canada, Saguenay
Dr. Raghavan Subasri (Examiner)	International Advanced Research Centre for Powder Metallurgy and New Materials (ARCI)
Dr. Zhan Zhang (Examiner)	University of Quebec At Chicoutimi
Dr. Xiao Grant Chen (President-Examiner)	University of Quebec At Chicoutimi

Dedicated to the memory of my aunt

RÉSUMÉ

Le présent travail fournit un aperçu sur le développement d'alternatives écologiques aux revêtements à base de chrome pour la protection de l'aluminium contre la corrosion. Des films minces de silicate de sodium, de silicate de zirconium et de stéarate de zirconium ont été fabriqués sur des surfaces en alliage de l'aluminium AA6061. D'autre part, le silicate de sodium, le sulfate de manganèse monohydraté et le métavanadate d'ammonium ont été étudiés en tant qu'inhibiteurs de corrosion pour l'aluminium.

Dans la première partie, du silicate de sodium de qualité industriel a été utilisé pour fabriquer des films minces sur des surfaces en alliage de l'aluminium. L'objectif était de mieux comprendre le mécanisme de corrosion de l'aluminium et d'étudier son comportement en matière de protection contre la corrosion à l'aide de films minces à base de silicate.

La deuxième partie de ce travail porte sur l'étude du comportement du silicate de sodium, du sulfate de manganèse monohydraté et du métavanadate d'ammonium en tant qu'inhibiteurs de corrosion pour l'aluminium dans une solution de NaCl.

La troisième partie concerne la fabrication de films minces de silicate de zirconium par le procédé sol-gel. Le choix du zirconium a été inspiré par son excellente résistance à la corrosion dans les environnements agressifs. L'objectif principal de cette partie était de déterminer les conditions de fonctionnement optimales nécessaires à la production d'un excellent gel et ses fonctions en matière de protection contre la corrosion.

La dernière partie a été consacrée à l'étude du comportement des films minces superhydrophobes au stéarate de zirconium contre la corrosion. L'objectif principal était de fabriquer des films minces de stéarate de zirconium par un procédé d'électrodéposition sur des

surfaces en alliage de l’aluminium. Les propriétés hydrofuges, la morphologie, la composition chimique et les propriétés de corrosion ont été soigneusement étudiées pour déterminer les conditions optimales de fonctionnement.

ABSTRACT

This work provides an insight into the development of environmentally friendly alternatives to chromium-based coatings for the protection of aluminum against corrosion. Sodium silicate, zirconium silicate, and zirconium-stearate thin films were fabricated on laminated AA6061-T6 aluminum alloy substrates. On the other hand, sodium silicate, manganese sulfate monohydrate, and ammonium metavanadate were studied as corrosion inhibitors for laminated AA6061-T6 aluminum alloy.

In the first part, industrial graded sodium silicate was used to fabricate thin films on aluminum substrates. The objective was to develop a better understanding on the corrosion mechanism of aluminum and study its corrosion protection behavior using silicate-based thin films.

The second part of this work focuses on the study of the behavior of sodium silicate, manganese sulfate monohydrate, and ammonium metavanadate as corrosion inhibitors for laminated AA6061-T6 aluminum alloy in NaCl solution.

The third part involves the fabrication of zirconium silicate thin films by sol-gel process. The choice of zirconium was inspired by its excellent corrosion resistance in aggressive environments. The main objective of this part was to determine the optimal operating conditions needed to produce an excellent gel and its functions towards corrosion protection.

The final part was dedicated to investigating the zirconium-stearate superhydrophobic thin films behavior against corrosion. The focus was to fabricate zirconium-stearate thin films by electrodeposition process on aluminum substrates. The water-repellent properties, morphology,

chemical composition, and corrosion properties were studied carefully to determine the optimal operating conditions.

ACKNOWLEDGMENTS

Words are not enough to express my sincere gratitude and respect to Professor Dilip Kumar Sarkar, my thesis advisor. His invaluable comments and suggestions throughout the experimental and thesis work contributed to the success of this research.

My sincere thanks also go to Professor Debasis De from the Energy Institute of Bangalore, India. He generously gave his time to offer valuable comments toward improving this research. Also, Dr. Zhang Zhan for his invaluable help and advice on the use of Scanning Electron Microscopy (SEM) and image analysis. Additionally, I would like to thank Dr. Sofiene Amira and Dr. David Levasseur from the Quebec metallurgy Center at Trois-Rivières for their collaboration. Furthermore, I would like to acknowledge Dave Girard, Dany Racine, and Samuel Dessureault for their technical support.

I would also like to take this rare opportunity to thank my friends and collogues, notably: Henry Agbe, Karthikeyan Rajan, Wei Xu, and Xingli Chen, for their friendship, their help and insight in scientific discussions. Furthermore, I would like to express my gratitude to all CURAL members at the University of Quebec at Chicoutimi, in particular: Anil, Mohammad Reza, Xiaoming, Siamak, Ali, Lanfeng, and Ahmed, for the moments we shared during the last years.

I am also indebted to my friends: Jabril, Mahdiyeh, Mustapha, and Zahira, for their support and help during the period of my study. They made my life easier and more fun.

Importantly, my endless thanks also go to my beloved parents (Houssine and Malika), and my little sister Hanaa. Also, I deeply thank my brother Hicham, and his family; Sheila, Gabe, and

Mika, for the unconditional love, support, and encouragement, without you, this study would not have been accomplished. Last but not least, I would like to thank my loving and supportive wife Farah, whose faithful support during my study is highly appreciated. Thank you!

Finally, I would like to acknowledge the Fonds Natural Science and Engineering Research Council of Canada (NSERC), the University of Quebec at Chicoutimi (UQAC) and Aluminum Research Centre (REGAL) for their financial support.

TABLE OF CONTENT

LIST OF TABLES

LIST OF FIGURES

CHAPTER 1

INTRODUCTION

CHAPTER 1 : INTRODUCTION

1.1 Introduction

Metals and metal alloys are unavoidable in the modern world due to their tremendous contributions in applications such as household products, transportations, packaging, constructions, etc. [1–3], in which, aluminum metals and metal alloys are attractive because of their lightweight nature, good physical properties, greater stiffness and high strength to weight ratios. However, they are susceptible to corrosion in aggressive environments [4]. Generally, corrosion is defined as the deterioration of materials due to interaction with environments, which results in a loss of the materials. Corrosion causes degradation to the metal's surfaces in addition to major energy loss to the material. It was accounted that each year 20% of energy loss, which is roughly 4.2 % of the gross national product (GNP) of the United States was affected due to corrosion [5]. The associated economic impact of corrosion is estimated to be greater than a trillion dollars annually in the United States [6]. So, the protection of aluminum against corrosion is regarded as an important topic in materials science for many years.

1.2 Definition of the problem

Several methods have been employed for the protection of aluminum against corrosion. Chromium-based conversion coatings have been widely used in various fields on account of their decorative, corrosion protective performance, and good wear resistance [7]. These coatings are based on the conversion of the aluminum alloys surfaces from the natural oxide layer to a more environmental protective layer [8]. They effectively reduce the rate of oxygen reduction over

cathodes and moderately hinder the anodic dissolution kinetics. Furthermore, chromate-based coatings release soluble Cr^{+6} into the local environment, which is responsible for the 'self-healing' properties in the defected area of the material's surface. However, the carcinogenic effect and the high toxicity of hexavalent chromate causes the ban of this technology in many countries [9,10].

Therefore, many researches are in progress to find environmentally-friendly alternatives that offer the same level of protection and reliability as chromate-based coatings. Among them, green coatings are considered as suitable alternatives. Vanadate [11], permanganate [12], silicates [13], titanate [14], among many others, are some examples of such coatings.

1.3 Objectives

The corrosion behavior of aluminum is one of the major problems in industrial applications. The use of protective thin films or corrosion inhibitors could reduce the corrosion rate of aluminum in corrosive environments.

The main objective of this work is to protect aluminum against corrosion using environmentally-friendly techniques. The main objective can be sub-categorized as follows:

1. Fabrication of environmentally friendly sodium silicate (Na_2SiO_3) thin films on aluminum alloy substrates and study their corrosion properties.
2. Study of the behavior of sodium silicate (Na_2SiO_3), manganese sulfate monohydrate ($MnSO_4.H_2O$) and ammonium metavanadate (NH_4VO_3) as corrosion inhibitors for aluminum alloy.
3. Fabrication of zirconium silicate ($ZrSiO_4$) thin films on aluminum alloy substrates by sol-gel process and study their corrosion properties.

4. Electrodeposition of zirconium-stearate (Zr-SA) superhydrophobic thin films on AA6061 aluminum alloy substrates and study their corrosion properties.

1.4 Methodology

A brief summary of the methodology used is given bellow. Details of the experimental work is provided in each chapter to follow.

1. Sodium silicate thin films were fabricated on laminated AA6061-T6 aluminum alloy using a simple ultrasonic dip-coating process with varied concentrations of sodium silicate in aqueous solutions of 0.1, 0.5, and 1 M. The corrosion resistance of the fabricated thin films was tested in corrosive environment of 0.6 M (3.5 wt.%) NaCl.

2. The behavior of sodium silicate (Na_2SiO_3), manganese sulfate monohydrate ($MnSO_4.H_2O$) and ammonium metavanadate (NH_4VO_3) as corrosion inhibitors for laminated AA6061-T6 aluminum alloy was investigated in corrosive environment of 0.1 M wt.% NaCl.

3. Fabrication of zirconium silicate thin films using sol-gel process was carried out using zirconium (IV) n-propoxide $Zr(OCH_2CH_2CH_3)_4$ and tetraethyl orthosilicate (TEOS) $Si(OC_2H_5)_4$ as precursors. The thin films were applied on aluminum alloy substrates using spin-coating process and their corrosion properties were tested in 0.6 M (3.5 wt.%) NaCl aqueous solution.

4. Zirconium-stearate superhydrophobic thin films were fabricated using electrodeposition process, a method where laminated AA6061-T6 aluminum alloy substrates were immersed

in an electrolytic solution of zirconium (IV) n-propoxide and ethanolic stearic acid at a specific value of applied deposition potential. The corrosion properties of the fabricated thin films were tested in 0.6 M (3.5 wt.%) NaCl aqueous solution.

This thesis includes eight chapters, where chapter 2 is for literature review and that discusses the corrosion mechanism of aluminum and the toxicity of chromium-based coatings. In addition, the alternatives for chromate-based coatings were also reviewed. Furthermore, the detailed description of the experimental procedures is provided in Chapter 3. The rest of the thesis is structured as follows:

(i) Chapter 4 will discuss the improvement of the corrosion protection of aluminum using sodium silicate (Na_2SiO_3) thin films fabricated by a simple ultrasonication process.

(ii) Chapter 5 will provide a detailed discussion on the use of sodium silicate (Na_2SiO_3), manganese sulfate monohydrate ($MnSO_4.H_2O$), and ammonium metavanadate (NH_4VO_3) as corrosion inhibitors for aluminum in NaCl solution.

(iii) Chapter 6 will detail the use of zirconium silicate thin films fabricated by sol-gel process for the protection of aluminum against corrosion.

(iv) Chapter 7 will discuss the effect of zirconium-stearate thin films fabricated by electrodeposition process on the corrosion protection properties of aluminum.

(v) Chapter 8 will provide the overall conclusion of the thesis, though each contributing chapter includes its own conclusion.

References

[1] W.D. Compton, N.A. Gjostein, Materials for Ground Transportation, Sci. Am. 255 (1986) 92–100.

[2] H. Ohno, P. Nuss, W.-Q. Chen, T.E. Graedel, Deriving the Metal and Alloy Networks of Modern Technology, Environ. Sci. Technol. 50 (2016) 4082–4090.

[3] M. Liu, Y. Guo, J. Wang, M. Yergin, Corrosion avoidance in lightweight materials for automotive applications, Npj Mater. Degrad. 2 (2018) 24.

[4] J.-P. Immarigeon, R.T. Holt, A.K. Koul, L. Zhao, W. Wallace, J.C. Beddoes, Lightweight materials for aircraft applications, Mater. Charact. 35 (1995) 41–67.

[5] T.N. Nguyen, J.B. Hubbard, G.B. McFadden, A mathematical model for the cathodic blistering of organic coatings on steel immersed in electrolytes., J. Coatings Technol. (1991).

[6] T.L. Metroke, R.L. Parkhill, E.T. Knobbe, Passivation of metal alloys using sol–gel-derived materials — a review, Prog. Org. Coatings. 41 (2001) 233–238.

[7] A. Liang, Y. Li, H. Liang, L. Ni, J. Zhang, A favorable chromium coating electrodeposited from Cr(III) electrolyte reveals anti-wear performance similar to conventional hard chromium, Mater. Lett. 189 (2017) 221–224.

[8] Q. Boyer, M.R. Ortega Vega, C. de Fraga Malfatti, S. Duluard, F. Ansart, Correlation between morphology and electrochemical behavior of chromium-free conversion coatings for aluminum alloys corrosion protection, Surf. Coatings Technol. 351 (2018) 115–127.

[9] C. Pellerin, S.M. Booker, Reflections on hexavalent chromium: Health hazards of an

industrial heavyweight, Environ. Health Perspect. 108 (2000) 402–407.

[10] H.J. Gibb, P.S. Lees, P.F. Pinsky, B.C. Rooney, Lung cancer among workers in chromium chemical production., Am. J. Ind. Med. 38 (2000) 115–26.

[11] D.S. Kharitonov, J. Sommertune, C. Örnek, J. Ryl, I.I. Kurilo, P.M. Claesson, J. Pan, Corrosion inhibition of aluminium alloy AA6063-T5 by vanadates: Local surface chemical events elucidated by confocal Raman micro-spectroscopy, Corros. Sci. 148 (2019) 237–250.

[12] S.B. Madden, J.R. Scully, Inhibition of AA2024-T351 Corrosion Using Permanganate, J. Electrochem. Soc. 161 (2014) 162–175.

[13] N. Asrar, A.U. Malik, S. Ahmed, Corrosion prevention with sodium silicate, Al-Jubail, 1998.

[14] S. Verdier, N. van der Laak, F. Dalard, J. Metson, S. Delalande, An electrochemical and SEM study of the mechanism of formation, morphology, and composition of titanium or zirconium fluoride-based coatings, Surf. Coatings Technol. 200 (2006) 2955–2964.

CHAPTER 2

LITERATURE REVIEW

CHAPTER 2 : LITERATURE REVIEW

2.1 **Corrosion of aluminum**

Corrosion is defined as the deterioration of materials due to the reaction with their extraneous environments. It affects various classes of materials including metals, polymers, and ceramics [1]. Metals are produced from their natural ores and have the tendency to return to their most thermodynamically stable state, a phenomenon considered as corrosion. The corrosion of materials can be physical, chemical or electrochemical [2].

Aluminum (Al) and its alloys exhibit fascinating properties such as low density, high ductility, excellent strength to weight ratio, and high stiffness [3]. These properties make their use beneficial in several applications including aerospace [4], aircraft [5], automobiles [6], marine industry [7], computer components, food packaging [8], and construction [9]. Al is considered as a very reactive metal and therefore reacts with atmospheric oxygen to form a passive and stable protective oxide layer (Al_2O_3). This oxide layer stabilizes the Al surface and immune it from further reactions with the environment. However, when Al is exposed to aggressive environments such as aqueous salts, the corrosion resistance can be reduced.

When the Al metal alloy reacts with a corrosive aqueous solution, the corrosion process begins with rate controlled by both the anodic and cathodic reactions. The anodic and cathodic reactions are given by Equations (2-1) and (2-5), respectively.

$$\mathrm{Al} \rightarrow Al^{3+} + 3e^- \tag{2-1}$$

$$3H^+ + 3e^- \rightarrow + \frac{3}{2} H_2 \tag{2-2}$$

$$O_2 + 2H_2O + 4e^- \rightarrow 4OH^- \tag{2-3}$$

$$O_2 + 4H^+ + 4e^- \rightarrow 2H_2O \quad (2\text{-}4)$$

$$Al + 3H_2O \rightarrow Al(OH)_3 + \frac{3}{2} H_2 \quad (2\text{-}5)$$

The Al metal, with zero-oxidation state reacts in the solution and becomes an aluminum cation Al^{3+} by losing three electrons. The electrons resulting from oxidation of the aluminum metal are picked up by the hydrogen ions H^+ to form hydrogen gas at the cathodic site as described in Equation (2-2). On the other hand, the reduction of oxygen to hydroxide in alkaline or neutral media is described in Equation (2-3), while the reduction of oxygen in acidic media is given by Equation (2-4). Therefore, the redox reaction resulting from aluminum metal in aqueous media is the sum of both the anodic reaction and the cathodic reaction (Equation (2-5)).

There are many types of corrosion, resulting from different corrosion mechanisms, and various other factors. The following section discusses some of the forms of corrosion.

2.2 **Types of corrosion**

Some of the most common forms of corrosion are uniform corrosion, galvanic corrosion, pitting corrosion, and stress corrosion cracking. The type of corrosion depends on the elemental composition of aluminum alloy and also the surrounding environment [10,11].

2.2.1 Uniform corrosion

Uniform corrosion is characterized by corrosive attack over the entire or large surface area of the metal. Generally, the thickness of the sample will slowly decrease until the failure. This is

considered as one of the most important forms of corrosion. The identification and prediction of uniform corrosion are relatively easier, hence the disasters resulting from uniform corrosion are rare.

Figure 2.1: Image of uniform corrosion on metal [12]

Many techniques are used to protect metals from uniform corrosion. Examples include cathodic protection, coatings or paintings. Figure 2.1 shows an metallic pipeline near a marine environment undergoing uniform corrosion [12].

2.2.2 Galvanic corrosion

Galvanic corrosion is an electrochemical interaction between two different metals in the presence of an electrolyte. Galvanic corrosion is illustrated by the presence of the corrosion products accumulation at the joints between two or more different metals. Generally, one metal acts as anode and corrodes faster, while the other metal acts as a cathode and corrodes slower than

it would alone. The noble behavior of metals could be predicted according to their standard reduction potentials [12].

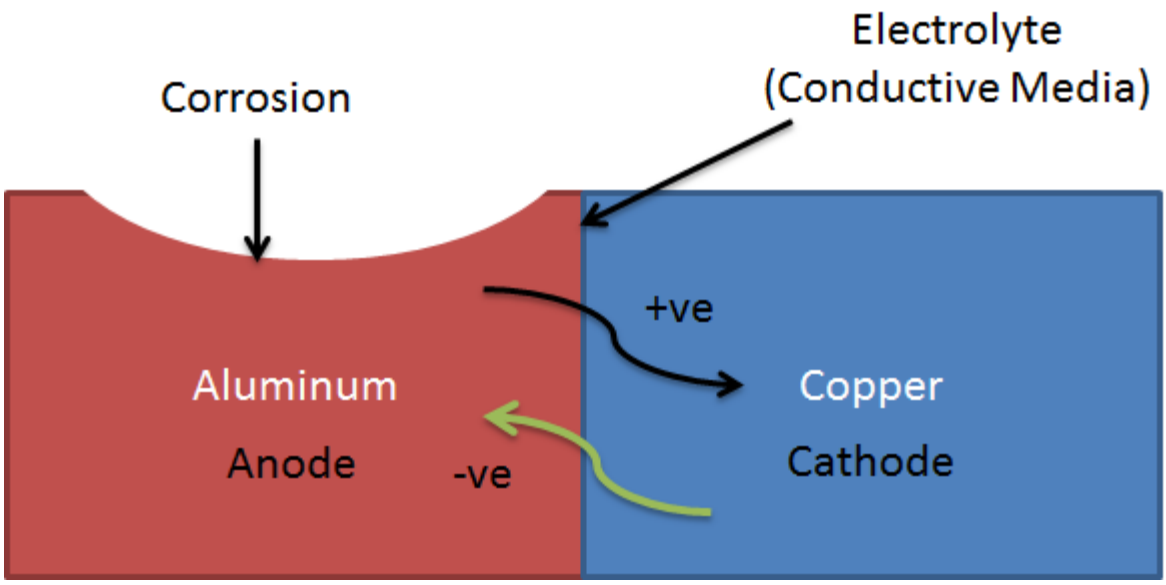

Figure 2.2: Galvanic corrosion mechanism when two metals (aluminum and copper in the image) are in contact [12].

Figure 2.2 presents the galvanic corrosion process of aluminum in contact with copper. In the presence of an electrically conductive path between the two metals, the ions move from the more anodic metal to more cathodic metal leaving behind electrons. The driving force for this dissolution is the potential difference between the two metals. Table 2.1 gives the electrode potential values of metals against saturated calomel electrode in seawater at 25 ˚C. Generally, when aluminum comes into contact with a more cathodic material it acts as a sacrificial anode and becomes susceptible to corrosion.

Table 2.1: Electrode potentials against saturated calomel electrode in seawater at 25 ˚C [13].

Metal	**Electrode Potential Volts**
Magnesium and its alloys	−1.60
Zinc die casting alloy	−1.10
Zinc plating on steel	−1.10
Zinc coated galvanized steel	−1.05
Aluminum cast and wrought	−0.75
Aluminum alloy	−0.60
Steel, carbon non-corrosion resisting	−0.7
Steel, stainless	−0.35
Lead	−0.55
Tin/Lead Solder	−0.50
Tin plate	−0.50
Copper, brass, bronze	−0.25
Nickel-copper alloys	−0.25
Nickel plating on steel	−0.15
Silver solder	−0.20
Silver	0
Silver plating on copper	−0.5
Titanium	0
Gold	+0.1
Platinum	+0.15

As can be seen from the table, aluminum is one of the most electronegative metals (-0.60 V) compared to cooper with an electrode potential value of -0.25 V [13]. Consequently, aluminum corrodes faster than copper in corrosive environments.

2.2.3 Pitting corrosion

Pitting corrosion is considered as a localized form of corrosion, which causes cavities in the material. The small area and small material removal caused by the pit make the detection difficult [14]. Generally, acidity, high chloride concentration, and low dissolved oxygen concentrations are the main factors that cause the breakdown of the protective layer. Pits can occur at different sites or sites of poor protective coatings.

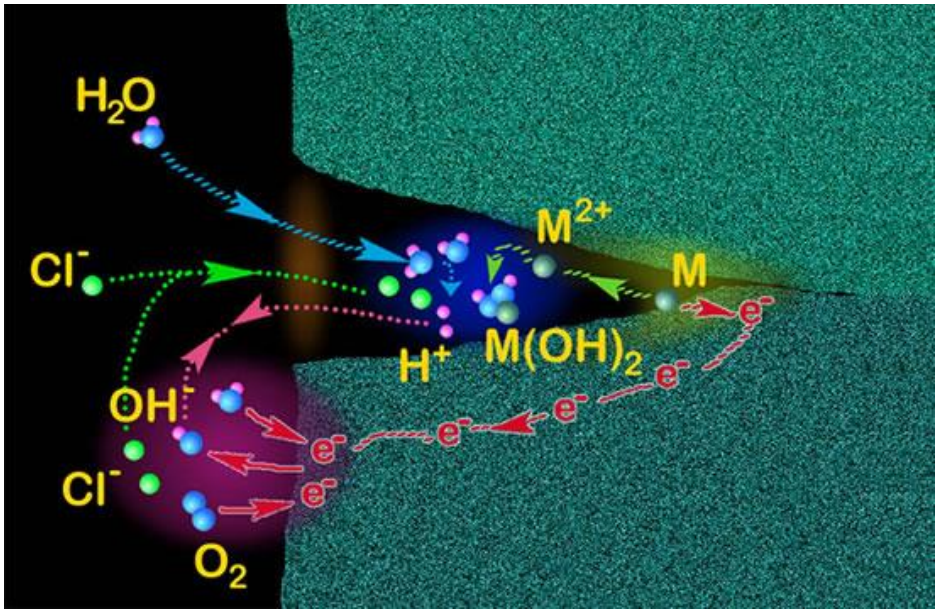

Figure 2.3: Schematic illustration of the mechanism of pitting corrosion on metals [14].

Figure 2.3 shows the pitting process of metal in the presence of chloride ions [14]. The process occurs inside and outside the pit according to the Equation (2-6) and Equation (2-7) below:

$$\text{Anodic reactions: } M \rightarrow M^{n+} + ne^- \quad (2\text{-}6)$$

$$\text{Cathodic reactions: } O_2 + 2H_2O + 4e^- \rightarrow 4OH^- \quad (2\text{-}7)$$

At the bottom of the pit, aluminum oxidizes into aluminum ions (Equation (2-6)). On the other hand, the reduction of water occurs in contact with the metal on the sites outside the pit (Equation (2-7)). As a result, the pH outside the pit increases to give an alkaline environment. Further, aluminum ions will form a film of aluminum chloride in the pit and stabilize it. After a while, the aluminum chloride will hydrolysis into aluminum hydroxide leading to a decrease in the pH value to a more acidic environment, which increases the corrosion rate in the pit.

2.2.4 Stress corrosion cracking

Stress corrosion cracking results from the combined effect of tensile stress and the corrosive environment. The stress could be due to applied loads or residual stress from the manufacturing process. Figure 2.4 shows an example of the colonies of stress corrosion cracks on the external surface of the high-pressure gas transmission pipeline [15]. Due to the presence of continuous stress in the corrosive environment, the cracks propagate along with the gradual penetration of the corrosive ions.

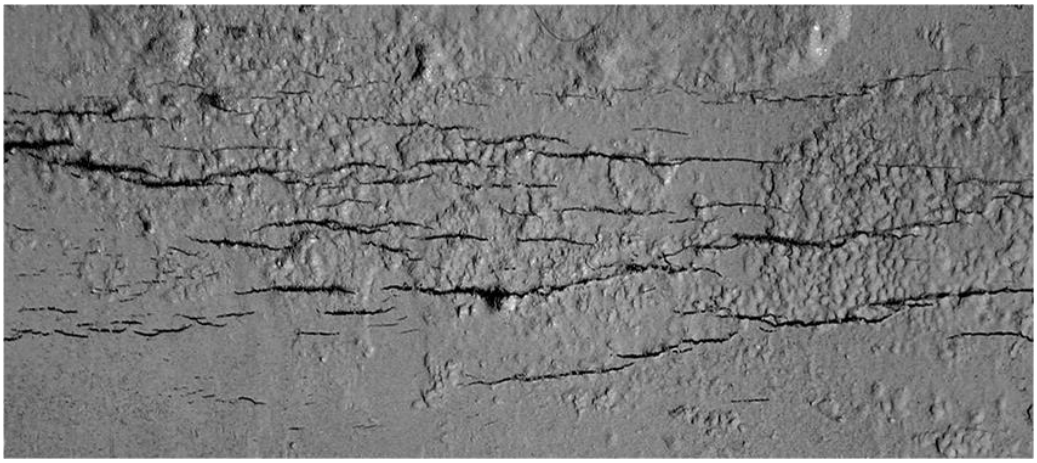

Figure 2.4: Example of stress corrosion cracks on the external surface of the high-pressure gas transmission pipeline [15].

There are several factors affecting the stress corrosion cracking such as alloy composition, tensile stress, corrosive environment, temperature and time [16].

2.3 **Methods of protection against corrosion**

2.3.1 Barrier coatings

Volatile organic compounds (VOCs) and hazardous air pollutants (HAPs) in the presence of moisture can enhance corrosion of metals. In particular, SO_2 and H_2S can combine with water from rain, to form sulfurous acid and eventually fall as acid rain. Acid rain is a well-known cause of the corrosion, particularly in the mining, petroleum, and marine areas [17]. In order to reduce the corrosion rate of metals in such conditions, several efforts have been explored to develop protective barrier coatings against corrosion. Protective coatings act as a physical barrier to prevent the transfer of electrochemical charges from the corrosive electrolyte to the metallic substrate. Barrier coating technologies such as sol-gel, plasma deposition, and electrodeposition will be briefly discussed here.

2.3.1.1 Sol-gel

The sol-gel process is a wet-chemical synthesis technique for preparation of oxide gels, glasses, and ceramics at low temperature [17]. The process involves the evolution of inorganic networks from colloidal suspension (sol). In particular, the hydrolysis and condensation of metal alkoxides (e.g. TEOS) result in the gelation of the sol to form a network of a continuous liquid phase called gel [18]. The sol-gel method is regarded as one of the most promising technique due to its various advantages such as low environmental impact, good chemical stability, low-cost and suitability for application on large areas and complex-shaped substrates [19–21]. The simultaneous hydrolysis and condensation reactions, resulting from the sol synthesis process are presented in Table 2.2 where 'M' stands for metal, 'O' for oxygen, and 'R' for reactive groups. The sol-gel process results in the formation of –M–O–M– oxide bridges between metal atoms and by-products of water molecules or alcohol for water or alcohol condensation respectively.

Table 2.2: Sol Synthesis Reaction.

Reaction	Formula
Hydrolysis reaction	$M–OR + H_2O \rightarrow M–OH + ROH$
Water condensation	$M–OH + HO–M \rightarrow M–O–M + H_2O$
Alcohol condensation	$M–OR + HO–M \rightarrow M–O–M + ROH$

The sol-gel method is used to prepare both inorganic coatings and inorganic-organic hybrid coatings on metals. Amongst the inorganic precursor, alkoxysilane, is the most preferred since it is mild and easily controllable [22].

Li *et al*. [22]. studied the effect of sol-gel hybrid coatings on the corrosion properties of laminated AA6061-T6 aluminum alloy. Using tetraethyl orthosilicate (TEOS) as SiO_2 source, ethanol as a solvent, both glycol and sodium dodecyl sulfate (SDS) as molecular controlling agents, and alkaline as a catalyst for the hydrolysis and condensation processes, they were able to prepare homogenous and uniform SiO_2 coatings on aluminum substrates with efficient anti-corrosion properties. The corrosion protection performance of SiO_2 coated sample using sol-gel hybrid coating (HC) was compared with chromate conversion coating (CCC), and bare aluminum substrate (BS) (Figure 2.5). The corrosion current density values were found to be 1.82, 1.98, and 7.28 $\mu A.cm^{-2}$ for HC, CCC, and BS samples, respectively. Generally, the lower the corrosion current density, the better the corrosion protection of the material [23]. These results were attributed to the continuous, homogenous and compact surface of the HC coatings on the aluminum substrates.

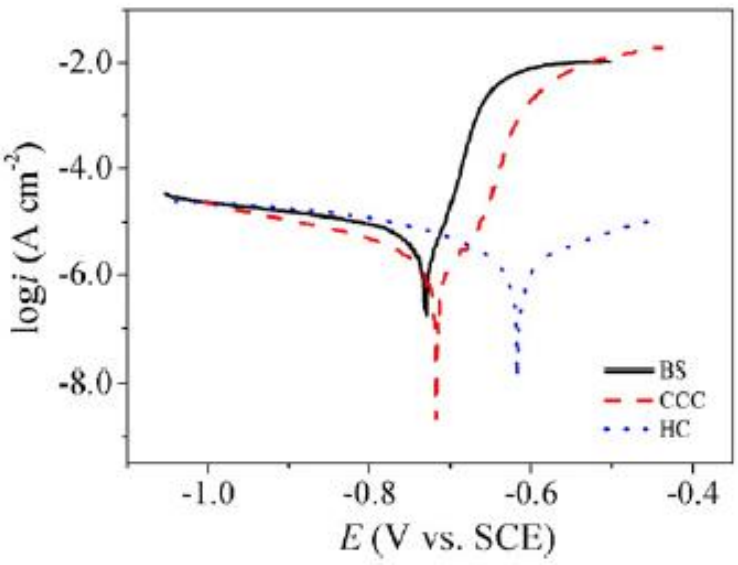

Figure 2.5: Polarization curves of aluminum bare substrate (BS), chromate conversion coating (CCC), and sol-gel hybrid coating (HC) in 3.5 wt.% NaCl corrosive medium [21].

2.3.1.2 Electrodeposition process

The electrodeposition of metals and alloys involve the electrochemical reduction of ions from aqueous, organic, and fused salt electrolysis. The deposition of material species involves the reduction of ions in the solution as, $M^{n+} + ne^{-} \rightarrow M$. The seemingly simple single reaction needs pre- and post complex steps before contributing to the whole deposition process. The two types of charged particles, an ion and an electron, can cross the interface. Hence, four types of fundamental areas are involved in the due process of deposition: (1) electrode-solution interface as the locus of deposition process, (2) kinetics and mechanism of the deposition process, (3) nucleation and growth processes of the deposits, and (4) structure and properties of the deposits [24]. Using the electrodeposition technique, a thick coating can easily be deposited on a conducting substrate with good control of thickness exhibiting excellent coating adhesion properties.

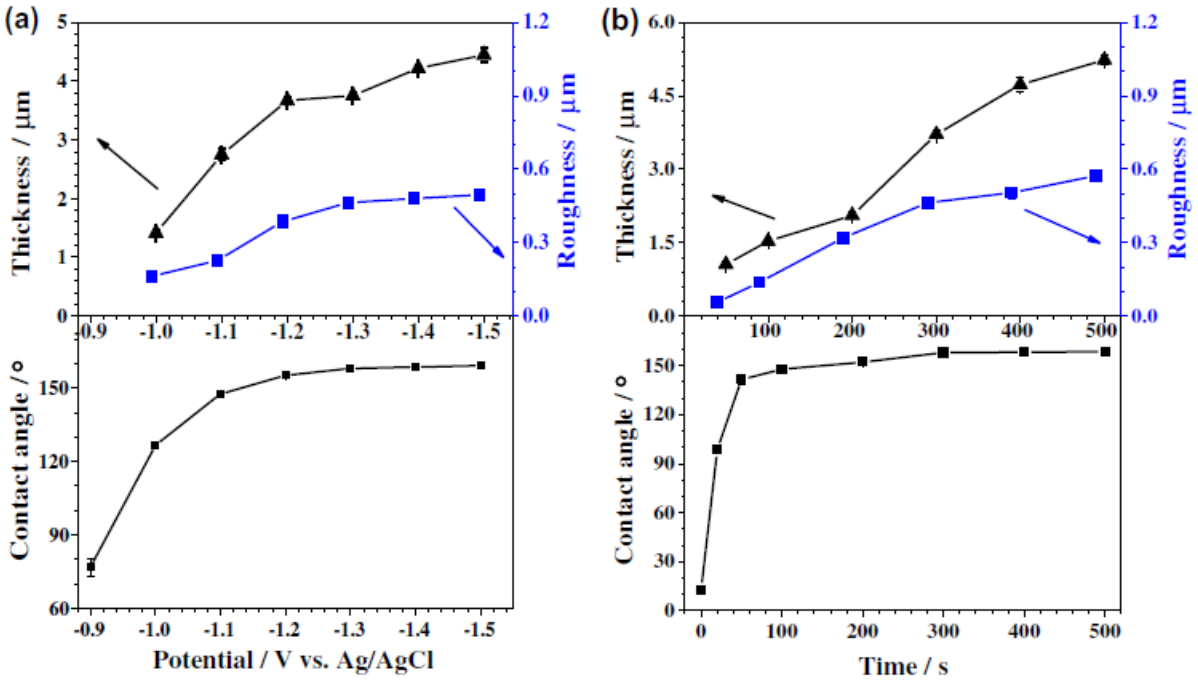

Figure 2.6: The variation of the thickness, roughness and contact angle of the fabricated films with (a) electrodeposition potential and (b) electrodeposition time [25].

Wu *et al.* [25] studied the corrosion protection properties of superhydrophobic silica films on steel by the electrodeposition process. The authors reported that the thickness and the roughness of the fabricated films are related to the electrodeposition potential and time as shown in Figure 2.6 (a) and (b), respectively. The increase in the electrodeposition potential and time leads to the formation of a thicker film on the metallic substrate, which could be due to the increase of the deposition rate on the metallic substrate. Furthermore, the corrosion performance of the coated sample with optimum conditions was investigated by SEM analysis as shown in Figure 2.7.

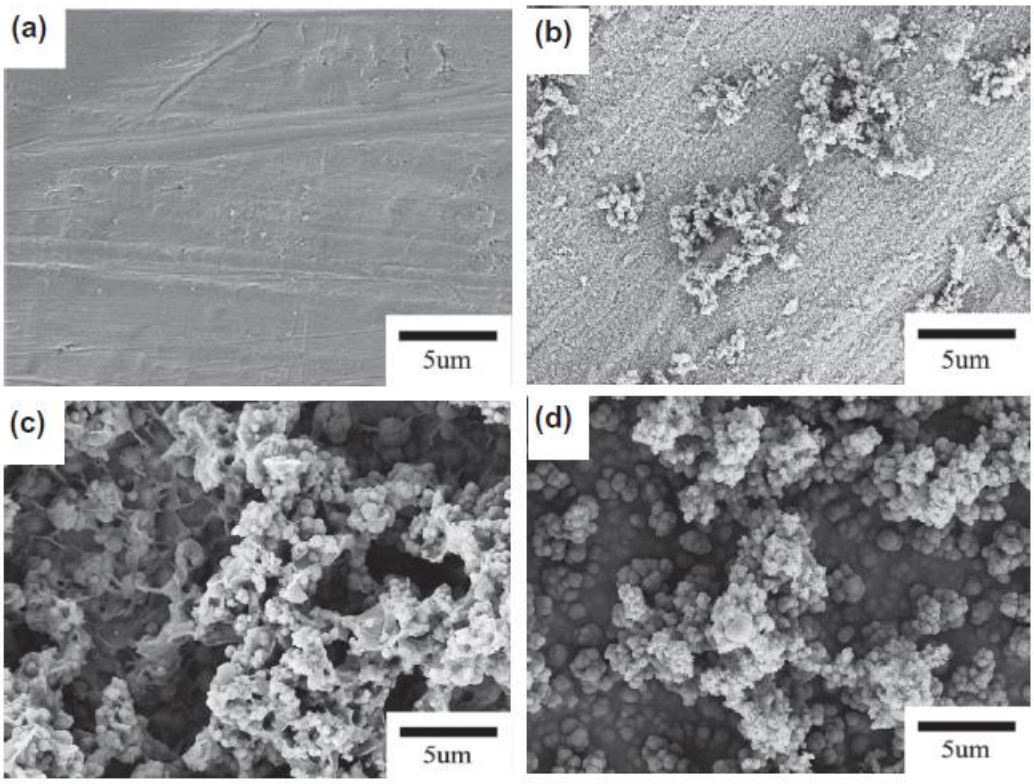

Figure 2.7: SEM images of steel substrate (a,b) and superhydrophobic film coated on steel. (a and c) represent before corrosion images, (b and d) are the images after corrosion tests. [25]

The SEM images of the steel substrate before and after immersion in a corrosive solution of 3.5 wt.% NaCl were presented in Figure 2.7. It can be seen from the images that the substrate presents corrosion-related features after immersion (Figure 2.7 (b)). On the other hand, the SEM image of the superhydrophobic film after immersion in corrosive solution (Figure 2.7 (d)). shows no change compared to before immersion (Figure 2.7 (c)). These results show the good corrosion protection properties of the fabricated films by electrodeposition process.

2.3.2 Corrosion protection by inhibition

Among the different methods to protect metals against corrosion, inhibition is one of the efficient methods and one of the most useful in the industry [26]. Corrosion inhibition process is used in many applications such as the oil industry, water transmission, and distribution systems, and boilers [27]. Generally, corrosion inhibitors are substances or mixtures that in low concentrations prevent or minimize the corrosion process of metals in corrosive mediums [28]. The inhibitor adsorbs on the metallic surface and forms a protective layer that prevents the corrosive ions from penetrating the substrate. Generally, inhibitors can be classified according to their chemical nature and their mechanism of action.

2.3.2.1 Inorganic inhibitors-Anodic and cathodic

2.3.2.1.1 Anodic inhibitors

Anodic inhibitors act by reducing anodic reactions on the metallic surface. Generally, these inhibitors react with the corrosion products resulting in an insoluble film on the metal surface. Lu *et al.* [29] reported the corrosion inhibition efficiency of sodium molybdate (Na_2MoO_4) in the corrosive environment of phosphoric acid (H_3PO_4). The resulted potentiodynamic polarization curves in Figure 2.8 shows that the increase of Na_2MoO_4 concentration leads to a shift of the potential towards positive values compared to the aluminum substrate without inhibitor. This result indicates that Na_2MoO_4 acts as an anodic inhibitor in the acidic environment of H_3PO_4.

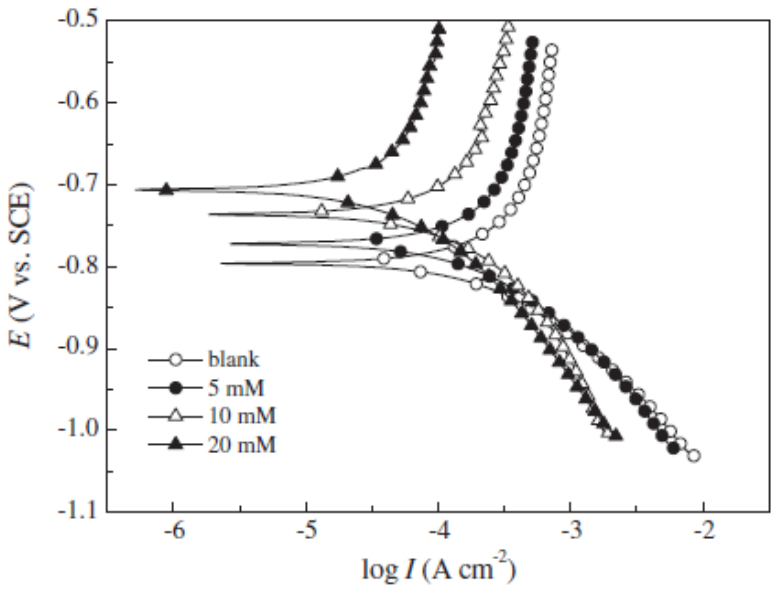

Figure 2.8: Potentiodynamic polarization curves of the aluminum substrate in 0.1 M H_3PO_4 without and with different concentrations of Na_2MoO_4 [29].

2.3.2.1.2 Cathodic inhibitors

The cathodic inhibitors act by reducing the cathodic reactions of the metal during the corrosion process. Generally, these inhibitors have metal ions that produce cathodic reactions due to the environment's alkalinity. This produces insoluble compounds that adsorb selectively on the cathodic sites of the metal. The deposition of such compounds forms a thin film protective layer that prevents diffusion of reducible species in the cathodic areas, resulting in higher impedance of the surface. Nam *et al.* [31] studied the corrosion inhibition efficiency of Lanthanum diphenylphosphate $La(dpp)_3$ on steel in a corrosive solution of 0.1 M NaCl. Figure 2.9 represents the potentiodynamic polarization tests of steel without and with the presence of $La(dpp)_3$. Notably, the potentials shift towards negative values with the increase of the inhibitor concentration. This can be attributed to precipitation of protective inhibitor molecules on the steel surface. This

deposition could result in a reduction of the movement of ions on the surface increasing the electrical resistance of the metallic substrate.

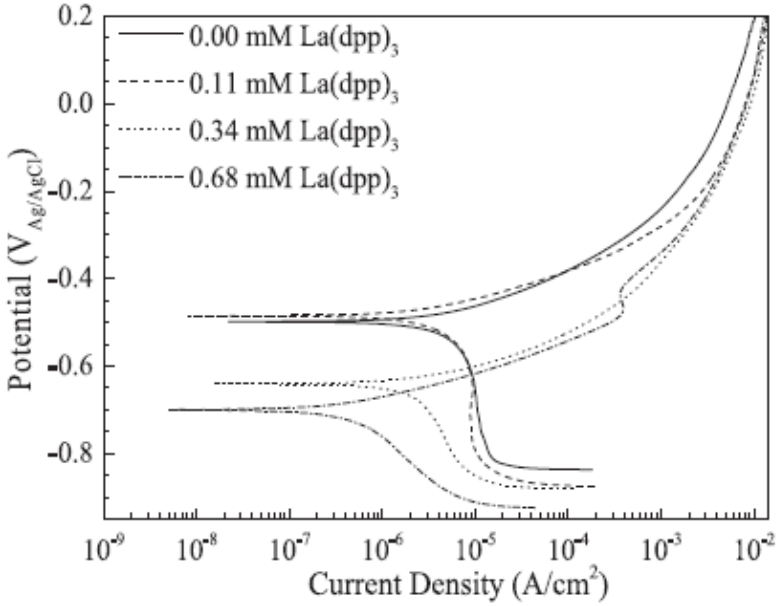

Figure 2.9: Potentiodynamic polarization curves of steel substrate without and with the presence of $La(dpp)_3$ at different concentrations in a corrosive solution of 0.1 M NaCl [31].

2.3.2.2 Organic inhibitors

The organic inhibitors can act as cathodic, anodic or both. These inhibitors are known as environmentally-friendly inhibitors and act by adsorption process on the metallic substrate. Figure 2.10 represents the action of organic inhibitors on the metallic substrate, where the inhibitor molecules form a protective film on the surface to protect the metal against corrosion. Generally, the inhibition efficiency of the organic inhibitors depends on many factors such as (a) chemical

structure of the molecules; (b) type and the number of the bonding atoms; (c) nature and the charge of the metal surface; (d) and type of the corrosive electrolyte [30].

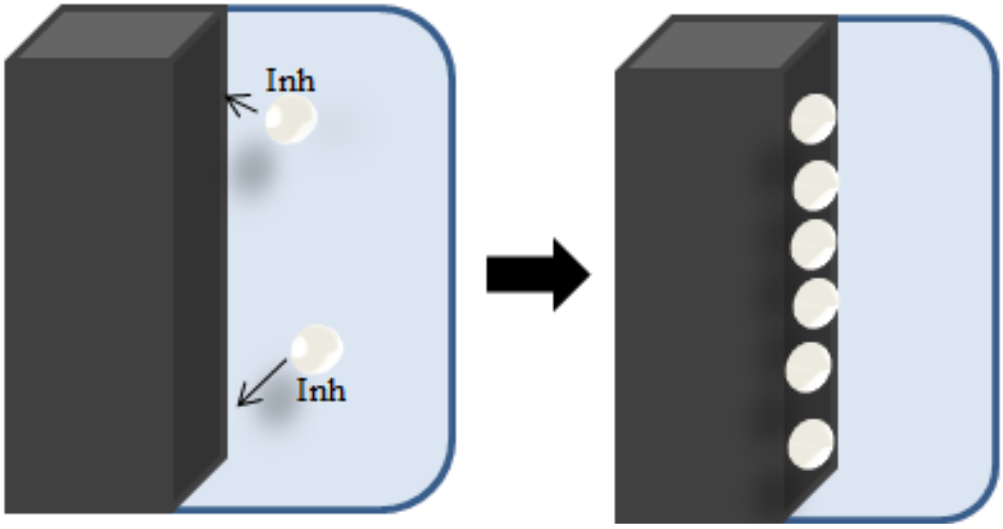

Figure 2.10: Schematic illustration on the action of organic inhibitors through adsorption process on a metallic substrate. Where the abbreviation 'Inh' represents the inhibitor molecules [32].

It has to be mentioned also that the metal surface covered by the formed film is proportional to the inhibitor concentration, which is a critical parameter in the corrosion efficiency of organic inhibitors. As an example, heterocyclic nitrogen compounds and sulfur-containing compounds are considered as organic inhibitors.

Several studies on the use of corrosion inhibition for protection of metals have been reported using organic inhibitors. For instance, Wysocka *et al.* [15] studied the corrosion inhibition effect of Butanedioic acid ($C_4H_6O_4$) on Al substrates. The corrosion tests performed in 0.05 M sodium bicarbonate ($NaHCO_3$) and 0.1 M sodium hydroxide (NaOH) showed an excellent corrosion

efficiency of 99.8 %. Similarly, Du *et al.* [32] investigated the performance of methyl ester of baicalin as a corrosion inhibitor on Al in a 1 M HCl corrosive medium. The inhibition efficiency of this inhibitor was found to be 96.12 %, which indicates its good corrosion inhibition properties.

2.3.3 Surface modification

In the aforementioned sections, the corrosion protection was concerned with the application of either a protective barrier coating or a reactive inhibitor that forms a protective layer on the metallic surface. However, in another method, one can modify the metallic surface to create a protective layer named as conversion layer. This treatment modifies the surface properties of the metal and forms an oxide or compound, which provides better corrosion properties to the metallic surface compared to its natural oxide layer. Generally, conversion coatings are characterized by their low cost and fast processing time. Most common conversion treatments are obtained using chromate conversion coatings, electrochemical anodization, and plasma ablation [33].

2.3.3.1 Chromate conversion coatings

Chromate conversion coatings (CCC) are considered as one of the most successful and widely used conversion coatings on different metallic surfaces. In particular, CCC has effectively been used to protect aluminum against localized corrosion and provide good adhesion to paints, which makes this technique useful for different applications [34]. Besides their ability to provide a protective layer against corrosion, chromate conversion coatings are also characterized by their ability to self-heal scratches and damages on the metallic surfaces as shown in Figure 2.11.

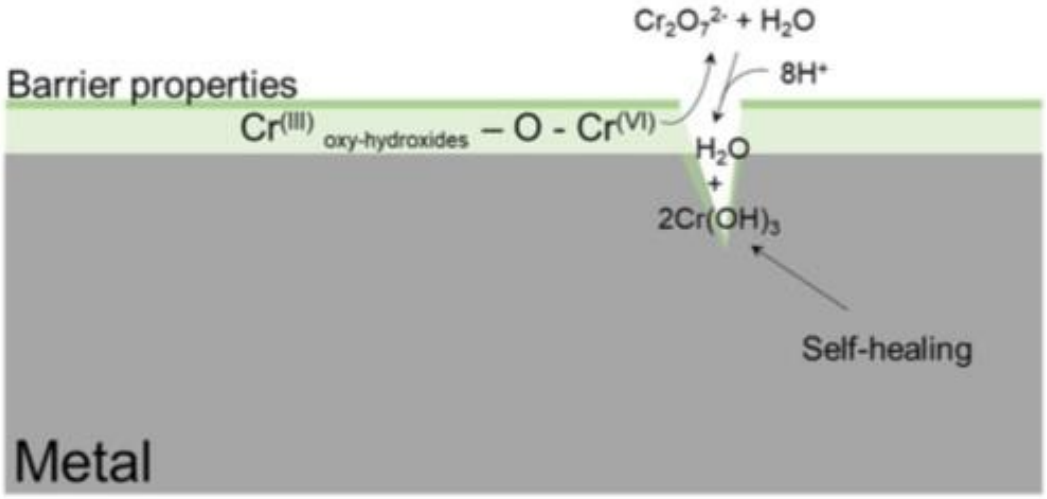

Figure 2.11: Schematic illustration of the self-healing and barrier properties of chromium conversion coatings on metallic surfaces [35].

2.3.3.2 Anodization

The anodization process is used to grow a thick oxide layer on the aluminum surface by anodic oxidation [37]. In a standard process, the anodization of aluminum is performed by immersion of the Al substrate (considered as the anode) and a steel substrate as a cathode in a sulfuric acid bath. With the application of a constant current density to the electrochemical cell, the aluminum surface undergoes oxidation and forms aluminum oxide as presented by Equation (2-8).

$$2Al_{(S)} + 3H_2O(l) \rightarrow Al_2O_3 + 6H^+ + 6e^- \qquad (2\text{-}8)$$

Generally, a 99% porous outer oxide layer is formed, which allow the corrosion inhibitors such as chromate acid to be incorporated inside those pores and thus increase the corrosion protection for the surface. On the other hand, the oxide layer provides good corrosion protection compared to the

uncoated aluminum surface due to the higher capacitive behavior of Al_2O_3. Figure 2.12 shows the Bode modulus plot of bare and anodized AA2024-T3 aluminum alloy in a 3% NaCl solution. The modulus of impedance versus the frequency from the electrochemical impedance spectroscopy (EIS) shows higher impedance modulus of the anodized sample compared to the uncoated substrate [33]. On the other hand, the thickness of the anodized layer is depending strongly on the applied current and the immersion time [36].

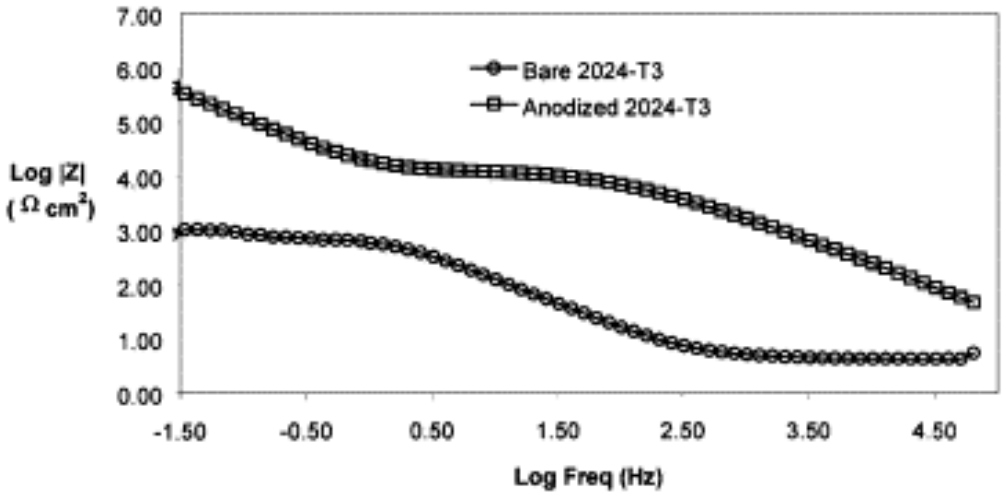

Figure 2.12: Bode impedance modulus plot of bare and anodized AA2024-T3 aluminum alloy in 3% NaCl solution [33].

2.3.3.3 Plasma ablation

Plasma ablation is a process which could be performed by sputtering or chemical etching. In the sputtering process, the surface is bombarded with plasma. Argon and hydrogen are the most commonly used gas for this procedure. When the gas ion collides with the metallic surface, an energy exchange takes place, resulting in dislodges of the atoms from all organic and inorganic

contaminants. On the other hand, chemical etching is a process where reactions take place between ions and atoms on the metallic surface. Oxygen is used in the chemical etching to clean the surface and deposit an oxide layer [37].

2.4 **Toxicity of chromates**

Chromium-based coatings are defined by their excellent corrosion resistance over a wide range of pH and electrolyte concentrations. They act as anodic and cathodic coatings, which means that they restrict the corrosion rate of metal, and simultaneously reduce the rate of reduction reactions (oxygen and water reduction) [28]. On the other hand, several studies during the past years indicated that chromates are both highly toxic and carcinogenic. Hexavalent chromium is now known to induce irreversible health damage such as nose, throat, eye and skin irritation, with a high risk of lung cancer [38,39]. Additionally, hexavalent chromium has also been documented to cause genotoxicity on aquatic and botanic life through soil and water contamination [40,41].

Several scientific works were reported the toxicity effect of chromates on some fish species. The chromium concentration in the fish environments could lead to changes in the physiology and survival of fish. The exact causes of death due to chromium depend on the time exposure and concentration of chromium. Table 2.3 summarizes the acute effects of chromium on freshwater fish.

Table 2.3: Acute effects of chromium on freshwater fish

Fish Species	[Cr]	Acute Effects
Salmo gairdneri	0.005 mg L^{-1}	Effect on fertilization [38].

Tilapia sparrmanii	0.098 mg L^{-1}	Decrease in blood clotting time [42].
Periophthalmus dipes	5-15 mg L^{-1}	Decrease in ion-dependent ATPase activity [43].
Labeo rohita	39.40 mg L^{-1} 96 h-LC50	Decrease in glycogen content, total lipid content and total protein content of liver, muscle and gill [44].
Colisa fasciatus	60 mg L^{-1}	Reduction in liver glycogen content. Hyperglycemic response [43].
Carassium auratus	250 μM	Decrease in cell viability. Increase in ROS [44].

2.5 **Alternatives to chromate coatings**

Despite the high efficiency in the corrosion protection of aluminum, the use of hexavalent chromium has been under strict regulation because of its highly toxic and carcinogenic nature [38,39]. On the other hand, various studies have now focused on non-chromate corrosion protection processes. Low toxicity conversion coatings prepared using non-chromate solution, such as zirconium, titanium, cerium, and molybdenum, have been widely investigated and developed. However, their anticorrosive performance is still inferior compared to chromate conversion coatings. In that regard, new inhibitors and formulations for anodization process and conversion coatings have been studied. The obtained results are promising but still in the infancy stage and need more investigations to meet industrial requirements.

Other possible alternative technologies for the corrosion protection of Al alloys, without hexavalent chromium coatings, include silicate, vanadate, manganese, zirconium, rare-earth,

organic, and phosphate-based coatings. Table 2.4 lists some alternative experimental and developmental technologies for replacing hexavalent chromium.

Table 2.4: Experimental and developmental technologies to replace hexavalent chromium in the corrosion protection of aluminum alloys

Coating	Ref.	Substrate	Characteristics	Findings
Silicates-based	Gao *et al.* [45] Corros. Sci 2011	Magnesium	The inhibition efficiency was found to be improved with the increase of sodium silicate concentration and reached a maximum of 99.4%.	The improved corrosion resistance is due to the formation of a transparent silicate thin film on the magnesium substrates.
	Garrity *et al*. [46] Electrochem. Acta 2014.	Aluminum	The addition of sodium silicate in 0.1 M NaCl inhibits the corrosion of aluminum.	The corrosion protection mechanism is found to be due to the formation of aluminosilicate on aluminum.
	Salami *et al.* [47] J. Magnesium Alloys 2014.	Magnesium	Sodium silicate coatings on magnesium substrate demonstrated a low corrosion rate of 0.12 mm/y compared to 9.8 mm/y for the bare magnesium alloy.	The improved corrosion properties are due to the formation of a mixed protective layer of Mg_2SiO_4 and MgO phases.
	Cerda *et al.*[48] Materials letters 2002.	Copper	Sodium silicate coating showed high anti-corrosion property 3 orders of magnitude higher than the as-received copper.	The corrosion resistance of the protective coating might be due to the formation of SiO_2 bonds.
Vanadate-based	Gharbi *et al.*[35] J. Electrochem. Soc 2015	Aluminum, Zinc, Carbon, Steel	Adsorption of inhibitor on cathodic sites and stabilization of passive film. Inhibition of oxygen reduction reaction	Do not meet environmental and health restrictions as Vanadium and its compounds were proven to be carcinogenic

	Ralston *et al.* [49] J. Electrochem. Soc 2008	Aluminum	$NaVO_3$ has no effect at pH of 3 and 5 but leads to a noticeable decrease in corrosion potential and corrosion current density at pH of 8 and 10.	Inhibition of Al by $NaVO_3$ in 0.05 M sodium chloride (NaCl) solutions is associated with tetrahedrally coordinated forms of vanadate.
Manganese-based	Danilidis *et al.* Corr. Sci. 2007	Aluminum	Manganese-based conversion coating provides good corrosion resistance for aluminum.	The corrosion protection properties of manganese-based conversion coatings could be improved by additives.
	Agnesia *et al.* [50] Ara J. Sci Eng 2009	Aluminum	The corrosion inhibition efficiency increases with the increase of $KMnO_4$ concentration.	Formation of Al-$KMnO_4$ complex on the metal surface, which prevents the penetration of corrosive ions.
Zirconium-based	Li *et al.* Int. J. Electrochem. Sci. 2016	Aluminum	Good corrosion protection of Al by the barrier properties of Zr-based coating.	The Zr-based coating is a promising high-performance protective coating.
	Haibin *et al.* [51] J. Mat Sci Letters 2001	Steel	Polarization resistance of the Zr-based thin films was 299 $\Omega.cm^2$ as compared to 40 $\Omega.cm^2$ for as-received steel substrates.	The heat treatment at high temperature leads to the formation of a dense coating.
Rare-earth-based	Haque *et al.* [52] Resources 2014	Aluminum, Steel	Mainly works as cathodic inhibitors, precipitation of Ce-oxide on cathodic sites,	Minor improvement in pitting potential and corrosion current was noted

			induced by the local pH increase	
Organic (including epoxy, sol-gel, polyurethane, silane, and nanocomposites)	Wolf *et al.*[53] Springer Briens in materials 2014	Aluminum, Steel	Good barrier properties	Nanocomposite: cost of implementation could be too important
Phosphate-based	Thomas *et al.*[54] Corros. Sci 2013	Aluminum, Steel, Carbon	Good barrier properties provided by the precipitation of metal-phosphate compounds	pH stability of phosphate-based coatings inferior to chromium oxide

References

[1] B. Cwalina, Biodeterioration of concrete, brick and other mineral-based building materials, Underst. Biocorrosion. (2014) 281–312.

[2] S. Michael, W. Dietrich, B. Roman, Corrosion Resistance of Aluminium and Aluminium Alloys, 2010.

[3] J.Y. Cao, M. Wang, L. Kong, L.J. Guo, Hook formation and mechanical properties of friction spot welding in alloy 6061-T6, J. Mater. Process. Technol. 230 (2016) 254–262.

[4] S.A. Abdel-Gawad, M.A. Sadik, M.A. Shoeib, Preparation and properties of a novel nano Ni-B-Sn by electroless deposition on 7075-T6 aluminum alloy for aerospace application, J. Alloys Compd. (2019).

[5] T. Maeno, K. Mori, R. Yachi, Hot stamping of high-strength aluminium alloy aircraft parts using quick heating, CIRP Ann. 66 (2017) 269–272.

[6] W.. Miller, L. Zhuang, J. Bottema, A.. Wittebrood, P. De Smet, A. Haszler, A. Vieregge, Recent development in aluminium alloys for the automotive industry, Mater. Sci. Eng. A. 280 (2000) 37–49.

[7] Y. Fu, X. Chen, B. Zhang, Y. Gong, H. Zhang, H. Li, Fabrication of nanodiamond reinforced aluminum composite coatings by flame spraying for marine applications, Mater. Today Commun. 17 (2018) 46–52.

[8] J.K. Oh, S. Liu, M. Jones, Y. Yegin, L. Hao, T.N. Tolen, N. Nagabandi, E.A. Scholar, A. Castillo, T.M. Taylor, L. Cisneros-Zevallos, M. Akbulut, Modification of aluminum surfaces with superhydrophobic nanotextures for enhanced food safety and hygiene, Food

Control. 96 (2019) 463–469.

[9] Y. Liu, H. Liu, Z. Chen, Post-fire mechanical properties of aluminum alloy 6082-T6, Constr. Build. Mater. 196 (2019) 256–266.

[10] E.E. (Ele E. Stansbury, R.A. (Robert A. Buchanan, Fundamentals of electrochemical corrosion, ASM International, 2000.

[11] C. Vargel, Corrosion of aluminium, Elsevier, 2004.

[12] Corrosion Testing Lab, Corrosion Testing Laboratory, Spectro Labs, (n.d.).

[13] C.H. Simmons, N. Phelps, T.L.D.E. Maguire, C.H. Simmons, N. Phelps, T.L.D.E. Maguire, Surface Finish and Corrosion of Metals, Butterworth-Heinemann, 2012.

[14] Crevice Corrosion, (n.d.). http://www.cdcorrosion.com/mode_corrosion/corrosion_crevice.htm (accessed March 24, 2019).

[15] J. Wysocka, M. Cieslik, S. Krakowiak, J. Ryl, Carboxylic acids as efficient corrosion inhibitors of aluminium alloys in alkaline media, Electrochim. Acta. 289 (2018) 175–192.

[16] C.T.F. Ross, C.T.F. Ross, An overview of pressure vessels under external pressure, Press. Vessel. (2011) 1–14.

[17] F. Ahnia, Y. Khelfaoui, B. Zaid, F.J. Pérez, D. Miroud, A. Si Ahmed, G. Alcalá, Thermally sprayed Al/Mo coatings on industrial steel E335 and effects on electrochemical parameters in simulated acid rain, J. Alloys Compd. 696 (2017) 1282–1291.

[18] L.C. Klein, M. Aparicio, A. Jitianu, Handbook of sol-gel science and technology : processing, characterization and applications, n.d.

[19] S. Senani, E. Campazzi, M. Villatte, C. Druez, Potentiality of UV-cured hybrid sol–gel coatings for aeronautical metallic substrate protection, Surf. Coatings Technol. 227 (2013) 32–37.

[20] R. Naderi, M. Fedel, F. Deflorian, M. Poelman, M. Olivier, Synergistic effect of clay nanoparticles and cerium component on the corrosion behavior of eco-friendly silane sol–gel layer applied on pure aluminum, Surf. Coatings Technol. 224 (2013) 93–100.

[21] L. Li, J. He, J. Lei, W. Xu, X. Jing, X. Ou, S. Wu, N. Li, S. Zhang, A sol–bath–gel approach to prepare hybrid coating for corrosion protection of aluminum alloy, Surf. Coatings Technol. 279 (2015) 72–78.

[22] S.B. Ulaeto, R. Rajan, J.K. Pancrecious, T.P.D. Rajan, B.C. Pai, Developments in smart anticorrosive coatings with multifunctional characteristics, Prog. Org. Coatings. 111 (2017) 294–314.

[23] A.A. Al-Amiery, F.A. Binti Kassim, A.A.H. Kadhum, A.B. Mohamad, Synthesis and characterization of a novel eco-friendly corrosion inhibition for mild steel in 1 M hydrochloric acid, Sci. Rep. 6 (2016) 19890.

[24] A. Mallik, B.C. Ray, Evolution of Principle and Practice of Electrodeposited Thin Film: A Review on Effect of Temperature and Sonication, Int. J. Electrochem. 2011 (2011) 1–16.

[25] W. Xu, K. Rajan, X.G. Chen, D.K. Sarkar, Facile electrodeposition of superhydrophobic aluminum stearate thin films on copper substrates for active corrosion protection, Surf. Coatings Technol. (2019).

[26] A. Shaban, I. Felhosi, J. Telegdi, Laboratory assessment of inhibition efficiency and

mechanism of inhibitor blend (P22SU) on mild steel corrosion in high chloride containing water, Int. J. Corros. Scale Inhib. 6 (2017) 262–275.

[27] Y.I. Kuznetsov, Progress in the science of corrosion inhibitors 1, Int. J. Corros. Scale Inhib. 4 (2015) 15–34.

[28] C.L. Page, Corrosion and protection of reinforcing steel in concrete, Woodhead Publishing, 2007.

[29] X. Li, S. Deng, H. Fu, Sodium molybdate as a corrosion inhibitor for aluminium in H3PO4 solution, Corros. Sci. 53 (2011) 2748–2753.

[30] H.J. Habeeb, H.M. Luaibi, R.M. Dakhil, A.A.H. Kadhum, A.A. Al-Amiery, T.S. Gaaz, Development of new corrosion inhibitor tested on mild steel supported by electrochemical study, Results Phys. 8 (2018) 1260–1267.

[31] N.D. Nam, P. Van Hien, N.T. Hoai, V.T.H. Thu, A study on the mixed corrosion inhibitor with a dominant cathodic inhibitor for mild steel in aqueous chloride solution, J. Taiwan Inst. Chem. Eng. 91 (2018) 556–569.

[32] C.G. Dariva, A.F. Galio, Corrosion Inhibitors-Principles, Mechanisms and Applications, in: Chapter Corros. Inhib., 2014.

[33] Y.-T. Du, H.-L. Wang, Y.-R. Chen, H.-P. Qi, W.-F. Jiang, Synthesis of baicalin derivatives as eco-friendly green corrosion inhibitors for aluminum in hydrochloric acid solution, J. Environ. Chem. Eng. 5 (2017) 5891–5901.

[34] R.L. Twite, G.P. Bierwagen, Review of alternatives to chromate for corrosion protection of aluminum aerospace alloys, Prog. Org. Coatings. 33 (1998) 91–100.

[35] O. Lunder, J.C. Walmsley, P. Mack, K. Nisancioglu, Formation and characterisation of a chromate conversion coating on AA6060 aluminium, Corros. Sci. 47 (2005) 1604–1624.

[36] O. Gharbi, S. Thomas, C. Smith, N. Birbilis, Chromate replacement: what does the future hold?, 2 (2018) 12.

[37] C. Blawert, P. Bala Srinivasan, Plasma electrolytic oxidation treatment of magnesium alloys, in: Surf. Eng. Light Alloy., Woodhead Publishing, 2010: pp. 155–183.

[38] G.E.J. Poinern, N. Ali, D. Fawcett, Progress in Nano-Engineered Anodic Aluminum Oxide Membrane Development, Materials (Basel). 4 (2011) 487–526.

[39] D. Manova, J.W. Gerlach, S. Mändl, Thin Film Deposition Using Energetic Ions., Mater. (Basel, Switzerland). 3 (2010) 4109–4141.

[40] ¡j --~ World, R. Organzation, will-~ IARC MONOGRAHS ON THE EVALUATION OF CARCINOGENIC Evaluation of Carcinogenic Risks to Rumans, which met in Lyon, n.d. https://monographs.iarc.fr/wp-content/uploads/2018/06/mono49.pdf (accessed March 31, 2019).

[41] H.J. Gibb, P.S.J. Lees, P.F. Pinsky, B.C. Rooney, Lung cancer among workers in chromium chemical production, Am. J. Ind. Med. 38 (2000) 115–126.

[42] H. Oliveira, Chromium as an Environmental Pollutant: Insights on Induced Plant Toxicity, J. Bot. 2012 (2012) 1–8.

[43] R. Bartlett, B. James, Behavior of Chromium in Soils: III. Oxidation1, J. Environ. Qual. 8 (1979) 31.

[44] V. Wepener, J.H. van Vuren, H.H. Du Preez, The effect of hexavalent chromium at

different pH values on the haematology of Tilapia sparrmanii (Cichlidae)., Comp. Biochem. Physiol. C. 101 (1992) 375–81.

[45] J. Thaker, J. Chhaya, S. Nuzhat, R. Mittal, A.P. Mansuri, R. Kundu, Effects of chromium(VI) on some ion-dependent ATPases in gills, kidney and intestine of a coastal teleost Periophthalmus dipes., Toxicology. 112 (1996) 237–44. http://www.ncbi.nlm.nih.gov/pubmed/8845044 (accessed March 31, 2019).

[46] S.S. Vutukuru, Chromium Induced Alterations in Some Biochemical Profiles of the Indian Major Carp, Labeo rohita (Hamilton), Bull. Environ. Contam. Toxicol. 70 (2003) 118–123.

[47] H. Gao, Q. Li, F. Chen, Y. Dai, F. Luo, L. Li, Study of the corrosion inhibition effect of sodium silicate on AZ91D magnesium alloy, Corros. Sci. 53 (2011) 1401–1407.

[48] O. Lopez-Garrity, G.S. Frankel, Corrosion inhibition of AA2024-t3 by sodium silicate, Electrochim. Acta. 130 (2014) 9–21.

[49] B. Salami, A. Afshar, A. Mazaheri, The effect of sodium silicate concentration on microstructure and corrosion properties of MAO-coated magnesium alloy AZ31 in simulated body fluid, J. Magnes. Alloy. 2 (2014) 72–77.

[50] L.. García-Cerda, O. Mendoza-González, J.. Pérez-Robles, J. González-Hernández, Structural characterization and properties of colloidal silica coatings on copper substrates, Mater. Lett. 56 (2002) 450–453.

[51] K.D. Ralston, S. Chrisanti, T.L. Young, R.G. Buchheit, Corrosion Inhibition of Aluminum Alloy 2024-T3 by Aqueous Vanadium Species, J. Electrochem. Soc. 155 (2008) 350–359.

http://www.ecsdl.org/terms_use.jsp (accessed December 13, 2018).

[52] S.A. Kanimozhi, S. Rajendran, ALUMINIUM INHIBITION BY POTASSIUM PERMANGANATE – Zn 2 + SYSTEM, Arab. J. Sci. Eng. 35 (2009) 41–52.

[53] H. Li, K. Liang, L. Mei, S. Gu, S. Wang, Corrosion protection of mild steel by zirconia sol-gel coatings, J. Mater. Sci. Lett. 20 (2001) 1081–1083.

[54] N. Haque, A. Hughes, S. Lim, C. Vernon, N. Haque, A. Hughes, S. Lim, C. Vernon, Rare Earth Elements: Overview of Mining, Mineralogy, Uses, Sustainability and Environmental Impact, Resources. 3 (2014) 614–635.

[55] E.L. Wolf, Applications of Graphene, Springer International Publishing, Cham, 2014.

[56] S. Thomas, N. Birbilis, M.S. Venkatraman, I.S. Cole, Self-repairing oxides to protect zinc: Review, discussion and prospects, Corros. Sci. 69 (2013) 11–22.

CHAPTER 3

EXPERIMENTAL PROCEDURES

CHAPTER 3 : EXPERIMENTAL PROCEDURES

3.1 Materials

The AA6061-T6 aluminum alloys have been widely used in many applications such as marine, aircraft and automotive industries due to their high strength and lightweight properties. The laminated aluminum alloy AA6061-T6 will be investigated in this project. The chemical composition of laminated aluminum alloy AA6061-T6 is listed in Table 3.1.

Table 3.1: The chemical composition of laminated AA6061 aluminum alloy

Elements	Al	Mg	Si	Mn	Cu	Fe	Ti	V
Composition (wt. %)	97.9	1.08	0.63	0.52	0.32	0.17	0.02	0.01

3.2 Cleaning process of la laminated AA6061-T6 aluminum alloy substrates

The Al substrates of dimensions of 1″ × 1″ and 1″ × 2″ were ultrasonically degreased in a diluted soap solution (LIQUINOX) for 15 minutes and then rinsed in deionized water for 15 minutes. Further, the substrates were dried on hotplate at 100 ˚C for 18 h.

3.3 Materials tests procedures and techniques

The experimental procedures and characterization tools employed in this study are presented in this part, also a brief description of the parameters used in the experiments with the necessary background is provided.

3.3.1 Electrochemical experiments

The electrochemical experiments were performed at room temperature (around 25 ˚C), in open air condition. Further, the corrosion resistance performance of the samples was investigated using Open circuit potential (OCP), potentiodynamic polarization (Tafel), and electrochemical impedance spectroscopy (EIS) tests. The electrochemical experiments were performed using a PGZ100 potentiostat and a 300 cm^3 EG&G PAR flat cell (London Scientific, London, ON, Canada), equipped with a three-electrode system with an Ag/AgCl reference electrode, a platinum (Pt) mesh as the counter electrode (CE), and the sample as the working electrode (WE) as shown in Figure 3.1. For the potentiodynamic polarization experiments, the potential was scanned from -250 mV to +1000 mV of OCP value. The electrochemical impedance spectroscopy (EIS) technique was performed in the frequency ranges between 0.001 Hz and 100 kHz with a sine-wave amplitude of 10 mV at room temperature. The potentiodynamic polarization curves were scanned in a range of -300 mV to 1200 mV with respect to OCP.

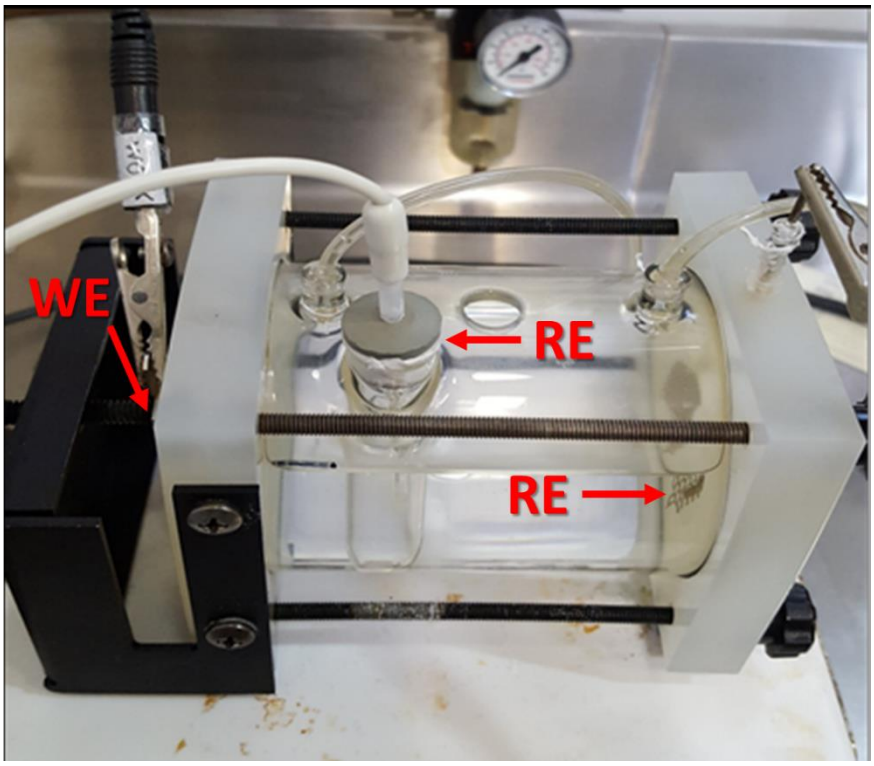

Figure 3.1: Electrochemical cell used in the present project with the three-electrode system, working electrode (WE), reference electrode (RE), and counter electrode (CE).

3.3.2 Infrared absorption analysis

The chemical composition of the samples was analyzed by Attenuated Total Reflectance-Fourier Transform Infrared spectroscopy (ATR-FTIR Agilent Technologies Cary 630) in the wavenumber range of 4000-450 cm^{-1}, as shown in Figure 3.2.

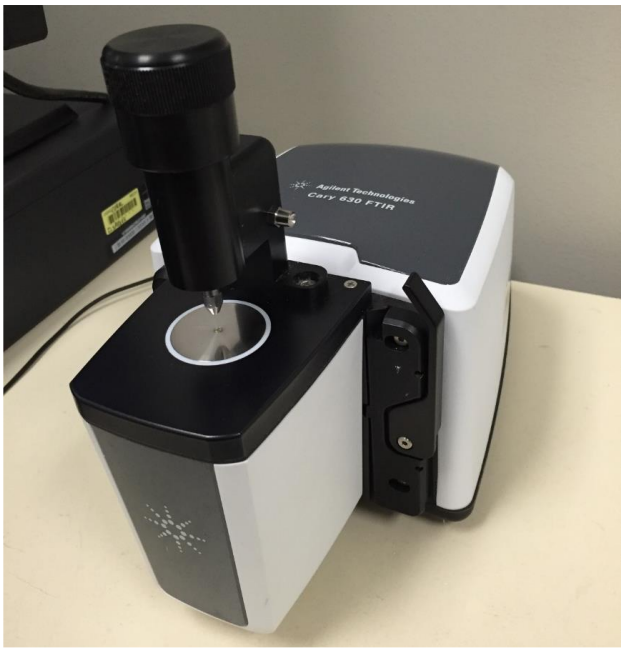

Figure 3.2: Fourier Transform Infrared Spectroscopy (ATR-FTIR) Cary 630 Agilent Technologies instrument.

Generally, the infrared radiation is passed through the sample, some of this radiation is absorbed by the sample, and some of it is transmitted. The resulting ATR-FTIR spectra represents the specific molecular absorption and transmission, creating a molecular fingerprint of the sample. This reason makes ATR-FTIR a useful tool for the chemical analysis of the samples.

3.3.3 Microstructural characterization by scanning electron microscopy

The surface morphology and its evolution of the samples was carried out using a Scanning Electron Microscope (SEM, JEOL JSM 6480LV), equipped with energy dispersive X-ray spectroscopy (EDS), as shown in Figure 3.3.

Figure 3.3: Scanning Electron Microscope SEM Jeol (model JSM 6480LV) instrument.

To analyze the surface morphology of the coating and surfaces, the samples were first placed in a vacuum environment, after which they are covered with a thin layer of gold to increase the conduction and thus improve the quality of the image. To deposition of this gold layer is insured by plasma for 90 s. Furthermore, the samples prepared are fixed on support using conductive adhesive. All these manipulations help to obtain a better resolution of the images and avoids charging effects. This device is also coupled to an Energy Dispersive X-ray Spectroscopy (EDS) allowing the identification and quantification of the elements present on samples surfaces.

3.3.4 Optical profilometry

The MicroXAM surface profiling microscope is used to measure the roughness of a surface in this work. A MapVue software is used to record the data received from the microscope and the

SPIP software allows the analysis of the resulting image by modeling the surface in 3D. This device works as an optical microscope. It is necessary to focus on the surface of the specimen to be analyzed and then start the acquisition. The microscope scans the surface of the specimen with great accuracy in order to give a detailed image of the surface of the sample.

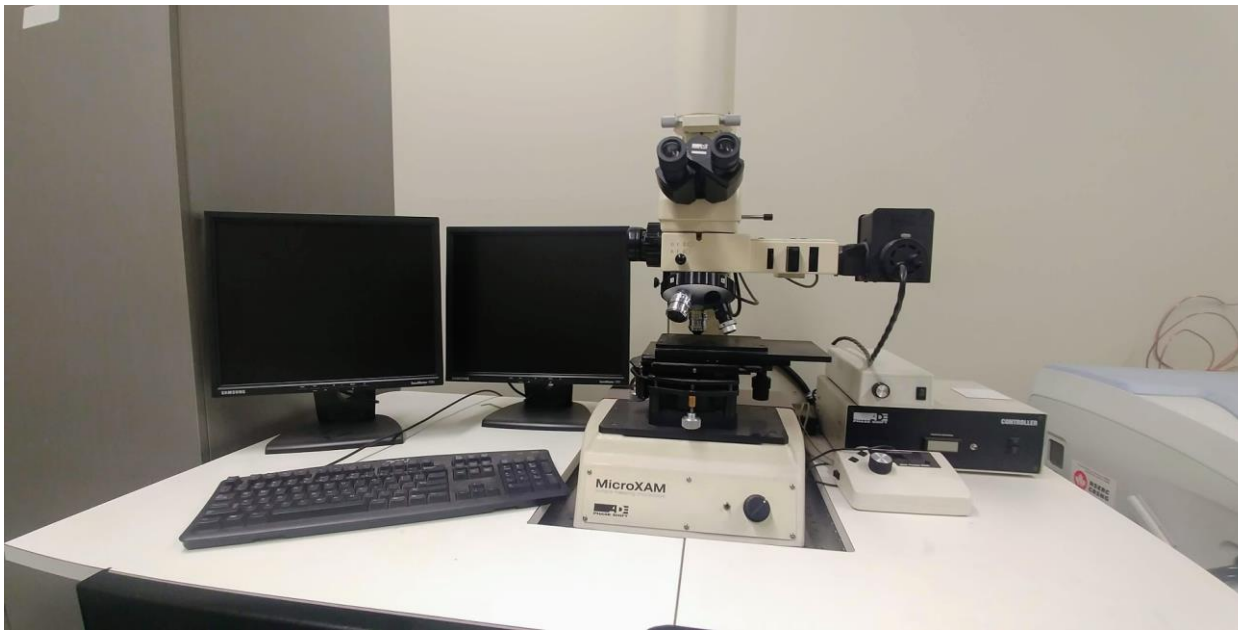

Figure 3.4: Instrument of Optical profilometry

From the image obtained, MicroXAM determines the root mean square (RMS) surface roughness. A large RMS value is related to rough surfaces.

3.3.5 Surface wettability

The surface wettability of the samples was analyzed by measuring the contact angle of 10 µL water drops using First Ten Angstrom contact angle goniometer as shown in Figure 3.5.

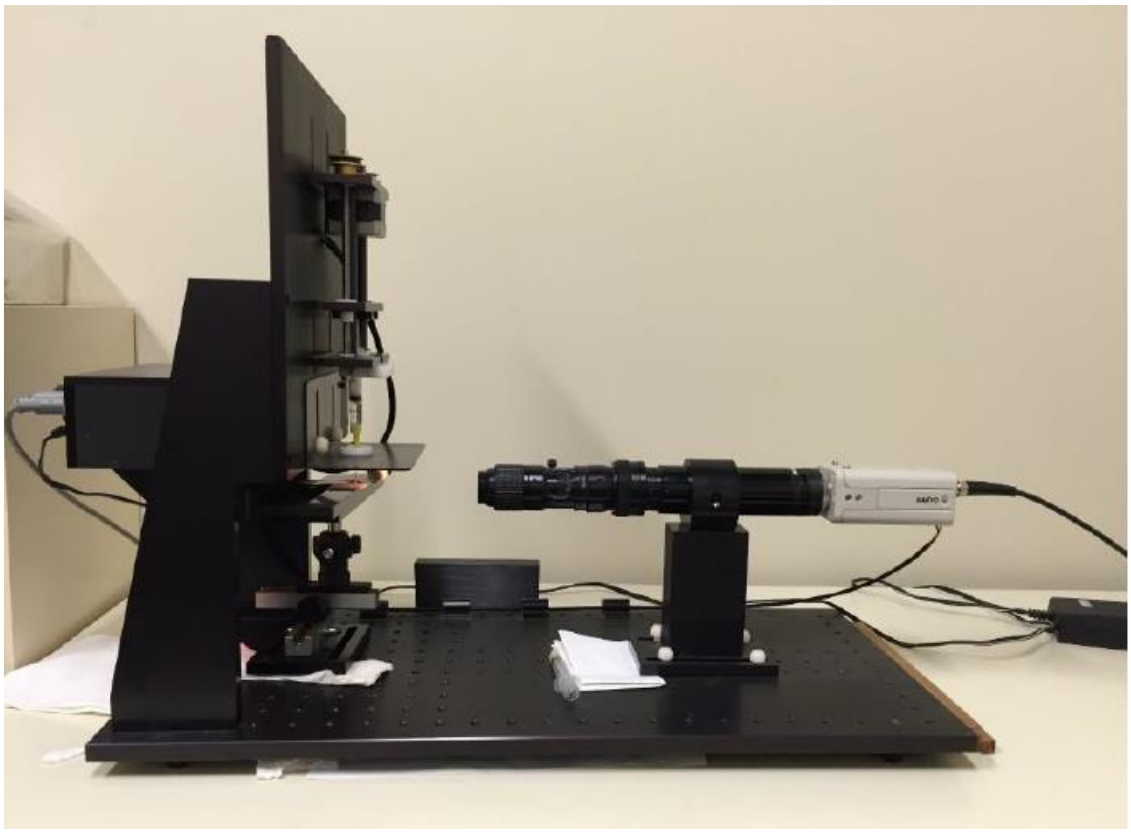

Figure 3.5: Contact angle goniometer

Superhydrophobicity refers to surfaces with extremely large water contact angles, greater than 150 ˚. It has proven that superhydrophobic surfaces exhibits higher resistance against corrosion. Hence, a part of this project focuses on the characterization of superhydrophobic thin films.

CHAPTER 4

ENHANCED CORROSION PROTECTION OF ALUMINIUM BY ULTRASONICALLY DIP COATED SODIUM SILICATE THIN FILMS

CHAPTER 4 : ENHANCED CORROSION PROTECTION OF ALUMINUM BY ULTRASONICALLY DIP COATED SODIUM SILICATE THIN FILMS

Abstract

A simple ultrasonic dip-coating process was utilized to fabricate sodium silicate thin films on laminated AA6061-T6 aluminum alloy substrates, and their chemical and corrosion properties were investigated as a function of their concentration in the solution. The attenuated total reflectance Fourier transmission infrared spectroscopy (ATR-FTIR) and energy dispersive X-ray spectroscopy (EDS) confirmed the presence of Na, Si, and O in the films. The polarization resistance (R_p) of the as-received aluminum substrates was found to be 10 ± 2 k$\Omega \cdot cm^2$ in 3.5 wt.% NaCl solutions. In comparison, sodium silicate thin films prepared from 1M solution exhibited a large R_p of 593 ± 32 k$\Omega \cdot cm^2$. The corrosion protection efficiency was calculated from the corrosion current density, which was found to be 99.52%. This study shows that sodium silicate thin films can be used as a protective coating against corrosion for aluminum substrates under aqueous NaCl environments.

4.1 **Introduction**

Metals and metal alloys have become an indispensable part of modern society and find applications in medical devices, electrical products, household products, transportations, food packaging, housing and construction, manufacturing, etc. [1–3]. In particularly, aluminum metal and alloys are not only attractive for their characteristic lightweight, high stiffness and good physical properties, but also excellent high strength to weight ratios. However, Al metals degrade and deteriorate by the electrochemical process in aggressive environments, which results in their wear and energy loss [4]. This electrochemical process herein referred as corrosion accounts for 20 % of energy loss annually, constituting to about 4.2 % of the United States' gross national product (GNP) [5]. Overall, the economic impact of corrosion on the United States economy is estimated to cost more than 1 trillion dollars annually [6]. Given the colossal economic loss due to corrosion, various strategies such as the use of corrosion inhibitors have been attempted to protect metals against corrosion. Traditionally, chromium-based coatings have been used due to their excellent anti-corrosive property [7,8]. However, due to increased environmental and safety concerns, their use have been discontinued in recent times [9,10].

In this regard, alternative anti-corrosion coatings such as silicate-based materials have attracted the attention of the scientific community in recent times [11]. Silicate-based materials do not only offer excellent polymerizability, chemical, and heat stability but also due to their biocompatibility and environmental friendliness, are ideal for the protection of metallic pipelines against corrosion [11,12]. Due to the formation of strong metal-silicate bonding between the thin film silicate coatings and the underlying metal substrate, silicate coatings offer good anticorrosive property. Such coatings have extensively been investigated for protecting metals such as mild steel [13], copper [14], zinc [15], magnesium [16,17] and aluminum against corrosion [18–20].

In particular, sodium silicate, commonly known as ‘water glass’, is used to protect metals against corrosion by coating and inhibition mechanism [17–21]. In the inhibition process, sodium silicate is added in the corrosive solution to reduce the corrosion rate of metals [11,17,20]. On the other hand, in the coating process, metals are coated by sodium silicate thin films to protect against corrosion [15,22,23].

Gao *et al.* [17] evaluated the corrosion properties of magnesium alloy by an inhibition process utilizing sodium silicate as an inhibitor. In this process, they immersed the magnesium alloy in the corrosive solution of standard ASTM D1384-87 (Na_2SO_4, 148 mg/L, $NaHCO_3$ 138 mg/L, NaCl 165 mg/L, pH 8.2) with different sodium silicate concentrations. The inhibition efficiency was found to be improved with the increase of sodium silicate concentration and reached a maximum of 99.4%. They concluded that this gain is due to the formation of a transparent silicate thin film on the magnesium alloy substrates. Similarly, Garrity *et al*. [20] studied the corrosion protection of aluminum alloy through the inhibition process by incorporating sodium silicate in the 0.1 M NaCl aqueous solution. In their study, the corrosion protection mechanism is found to be due to the formation of aluminosilicate on the aluminum substrate. Thus, the addition of sodium silicate to domestic or industrial water supply as a corrosion control agent of the metallic pipeline has also ensured zero effects on environment/health issues, which added desirable quality to silicate materials [11].

However, a few studies were focused on the corrosion properties of sodium silicate as a coating on metallic substrates. Salami *et al.* [16] used micro arc oxidation (MAO) process to fabricate sodium silicate coatings on magnesium substrate and demonstrated a low corrosion rate of 0.12 mm/y compared to 9.8 mm/y for the bare magnesium alloy. A similar study by Zhang *et*

al. [24] used the MAO process for the fabrication of sodium silicate coatings on titanium alloys and investigated their corrosion behaviors.

Additionally, using an immersion process, Cerda *et al.* [14] synthesized a sodium silicate thin film coating on copper substrates that showed high anti-corrosion property 3 orders of magnitude higher than the as-received copper. Similarly, Gaggiano *et al.* [25] detailed the sodium silicate deposition on porous aluminum oxide by a dip-coating process. They observed that the sodium silicate interacted with the pore on the aluminum surface that led to the formation of aluminosilicate. The authors have not reported any corrosion-related studies of silicate coatings.

However, the fabrication of sodium silicate thin films on aluminum metals and their corrosion protection have not been fully studied and therefore require further investigation. In this work, a simple ultrasonic dip-coating process is utilized to fabricate sodium silicate thin films coatings on aluminum alloy substrates. The effect of concentrations of sodium silicate in the solution is envisaged to study the surface morphology, chemical composition, and corrosion properties of the fabricated thin films.

4.2 **Experimental section**

In a typical procedure, the as-received aluminum substrates were chemically cleaned with soap solution, ethanol, and distilled water. Further, the samples were dried on hotplate at 100 ^{o}C for 18 h. To study the effect of the substrate pre-treatment on the coating process, a 1 M sodium hydroxide (NaOH) solution was used to chemically etch the as-received aluminum substrate at 55 ^{o}C for 3 minutes, followed by rinsing in distilled water. Afterward, both chemically cleaned and etched substrates were dried on hotplate at 100 ˚C overnight before the coating process.

The substrates were immersed into industrial-grade sodium silicate solution (SiO_2/Na_2O ratio of 3.22; pH ~ 12) having Molar concentrations of 0.1, 0.5, 0.75 and 1 M for 20 minutes in an ultrasonic bath (Branson 5510R-DTH, 135 W, 42 kHz) for dip-coating. After the ultrasonic dip-coating process, the substrates were dried on hotplate at 100 ˚C for 2 h to remove residual solvent and solidify the coating.

The morphological and elemental characterizations were performed on the fabricated thin films by scanning electron microscope (SEM, JEOL JSM-6480 LV) equipped with energy dispersive X-ray spectroscopy (EDS). The chemical composition analysis was carried out by Attenuated Total Reflectance-Fourier transform infrared (ATR-FTIR, Agilent Technologies Cary 630) spectra. The thickness of the fabricated thin films was measured using PosiTector 6000 probe. A three electrodes set-up, consisting of a platinum mesh (counter electrode), a silver/silver-chloride (Ag-AgCl) (reference electrode), and the fabricated samples (working electrodes) was employed to study the electrochemical properties of the samples. The potentiodynamic polarization curves were scanned in a range of -250 mV to 1000 mV with respect to OCP using a scan rate of 2 mV/s. The frequency range of the electrochemical impedance spectroscopy (EIS) study was fixed between 10^{-2} and 10^{5} Hz with an amplitude of 20 mV with respect to the open circuit potential (OCP). All the electrochemical experiments were carried out in 3.5 wt.% NaCl solution with a pH of 5.8 to simulate seawater.

4.3 **Results and discussion**

Figure. 4.1 (a) shows the ATR-FTIR spectra of sodium silicate thin films on aluminum substrates fabricated using the solutions with concentrations of 0.1 M, 0.5 M, 0.75 and 1 M. Figure.

4.1 (a-I) represents the thin film fabricated using 0.1 M sodium silicate solution. Due to the low concentration, very tiny peaks are observed.

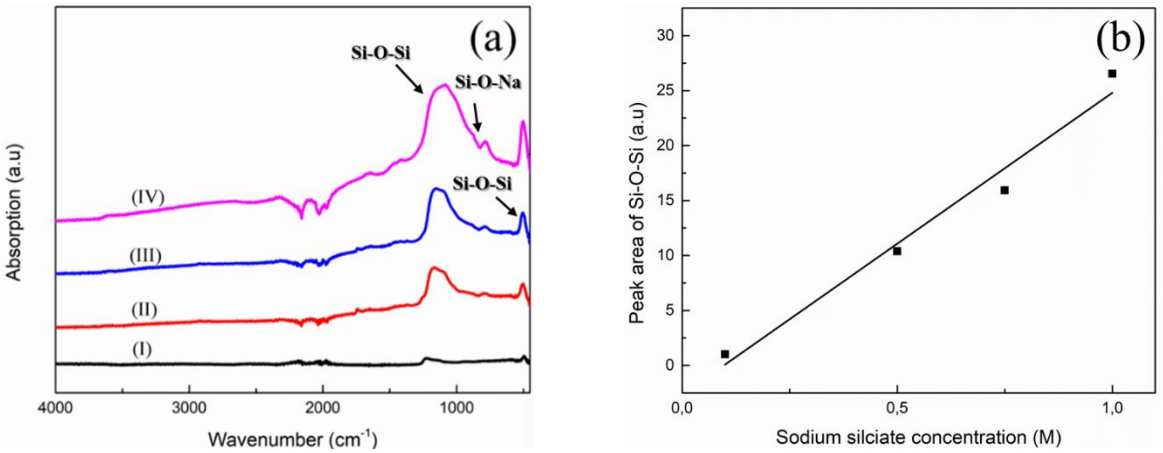

Figure. 4.1: (a) ATR-FTIR curves of sodium silicate thin films on aluminum substrates fabricated using (I) 0.1, (II) 0.5 (III) 0.75 and (IV) 1 M of sodium silicate solution (b) the variation in the peak area of Si-O-Si bond with respect to sodium silicate concentration.

The thin films fabricated using 0.5 M solution show four significant peaks at 501, 800, 943 and 1207 cm^{-1} in Figure. 4.1 (a-II). The peak at 1207 cm^{-1} is well matched with the Si-O-Si asymmetric stretching modes [27,28], while the peak located at 943 cm^{-1} could be attributed to the symmetric stretching vibration of Si-O-Na bond. Furthermore, the peaks at 800 cm^{-1} and 501 cm^{-1} correspond to symmetric stretching and bending vibration mode of Si-O-Si, respectively [27]. At a concentration of 0.75 and 1 M, the intensity of the Si-O-Si bond at 1207 cm^{-1} is largely increased as shown in Figure. 4.1 (a-III) and (a-IV). Similarly, the symmetric stretching and bending vibration mode are also observed with the 0.75 and 1 M concentration thin films. It has to be mentioned that Si-O-Si bond shows typically three characteristic peaks, namely, (i) stretching at

1070 cm^{-1} followed by a shoulder at 1150 cm^{-1}, (ii) bending at 810 cm^{-1} and (iii) rocking at 450 cm^{-1} [29].

The area of the intense peak around 1200 cm^{-1} associated with the sodium silicate thin film as shown in Figure. 4.1 (a) was determined by peak fitting software. Figure. 4.1 (b) shows the variation of the peak area of sodium silicate thin films fabricated with four solutions of different concentrations. The peak area increases linearly with the increase of sodium silicate concentration.

It is well known that the absorbance or the integrated peak area measurement is proportional to the concentration and thickness of the coating explained by the Beer-Lambert law [30]. The following Equation (4-1) governs this linear relationship:

$$A = \varepsilon . c . l \tag{4-1}$$

where A is the integrated absorbance of a specific vibration, ε is the absorption coefficient, and c is the concentration and l is the optical path length.

Figure. 4.2 represents the SEM images of (a) as-received aluminum substrate and sodium silicate thin films on aluminum substrates fabricated using the solution concentration of (b) 0.1, (c) 0.5 and (d) 1 M. Figure. 4.2 (b-d) shows the changes in morphological features on aluminum substrates attributable to the presence of sodium silicate features. Figure. 4.2 (b), exhibit nearly the same feature as shown in Figure. 4.2 (a) except certain patches around the existing craters, which could be related to the interaction of sodium silicate to aluminum [25]. Further increase of concentration to 0.5 and 1 M results in the formation of dense particles was observed, which can be clearly seen in Figure. 4.2 (d). The higher concentration also enhanced the formation of uniform morphological features with no specific nucleation sites (see Appendix A, Figure A.2). It is to be

mentioned that the inherent rolling lines were observed on all SEM images as it exists in the as-received aluminum substrate.

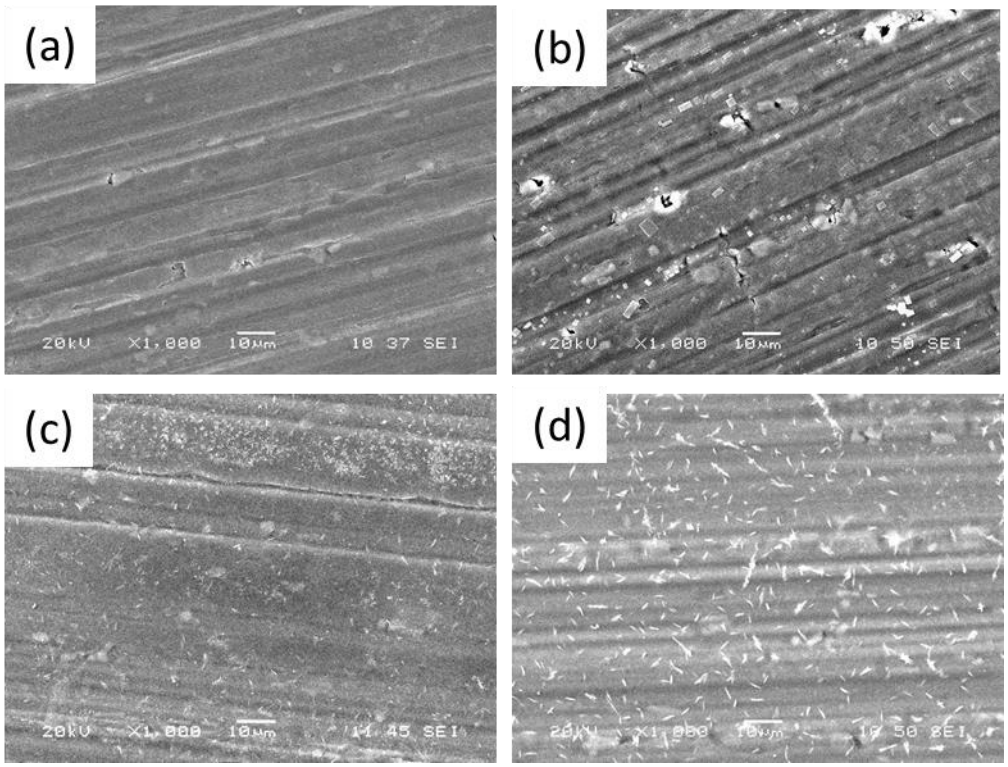

Figure. 4.2: SEM images of (a) as-received aluminum substrate, and sodium silicate thin films on aluminum substrates formed using (b) 0.1, (c) 0.5, and (d) 1 M of sodium silicate solution.

Figure. 4.3 shows the EDS spectrum of sodium silicate thin film coated aluminum substrate prepared from 1 M solution. The spectrum displayed corresponds to the inset SEM image for the entire region that includes particle and flat area. The spectrum is composed of Na, Si and O elements with their respective Kα X-ray peaks at 1, 1.7 and 0.5 keV. A strong peak at 1.4 keV has been observed due to the Kα X-ray from the aluminum substrate [16]. The table in the inset describes the detailed elemental composition of the global area of the SEM image. The

composition in the global region is found to be 3.30, 24.48 and 72.22 at. % respectively to the elements of Na, Si, and O. The morphological feature is composed of the particle (spot 1) and flat area (spot 2) as indicated in the SEM image (EDS spectra of region 1 and 2 are provided in Figure A.1 in Appendix A). The spectrum of the particle shows Na, Si, and O with the respective composition of 8.38, 16.89 and 74.73 at. %. Similarly, the composition of the flat area is found to be 6.60, 20.81 and 72.60 at. % of Na, Si, and O, respectively. It is clearly observed that the flat area is covered by sodium silicate with the excess of Si, confirming the sodium silicate deposition and complementary with ATR-FTIR results.

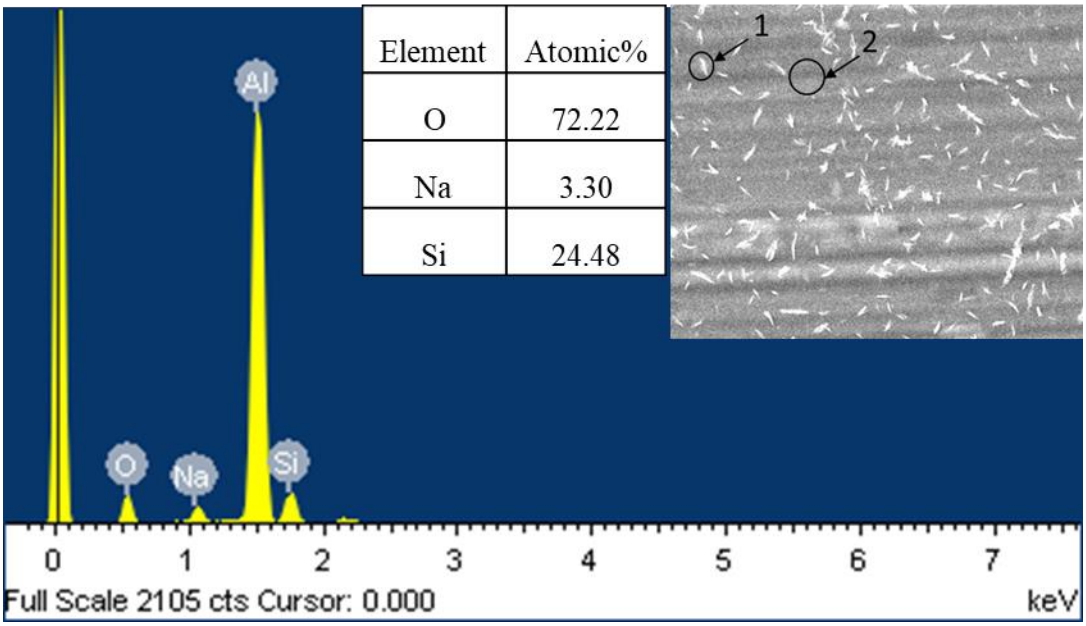

Figure. 4.3: EDS spectrum of the sodium silicate thin film on aluminum substrate formed using 1 M of sodium silicate solution for the global region of SEM image. The inset shows the corresponding SEM image with two circular spots. 1. Particle, 2. Flat area.

To quantify variation in elemental composition across the 1 M sodium silicate coated thin film, EDS line scan was performed (Figure. 4.4). The EDS line scan shows a uniform distribution of the elements of O, Na, and Si across the surface confirming the uniformity of the deposited thin film.

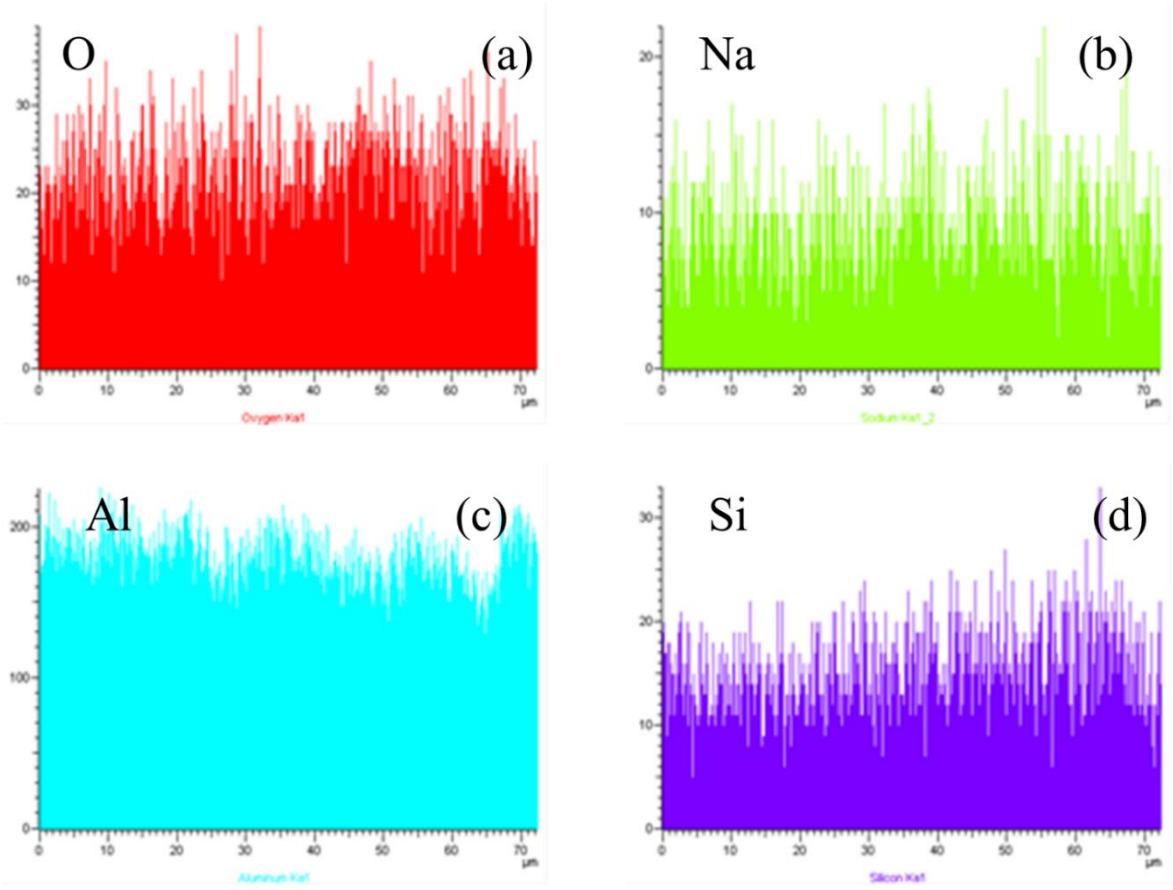

Figure. 4.4: The EDS line-scanning of the 1 M sodium silicate thin film on Al substrate for the elements of (a) O, (b) Na, (c) Al, and (d) Si.

To verify the uniformity of the fabricated 1 M sodium silicate thin film coating, surface roughness (Root mean square, rms) was determined at six different spots (with the size of

~ 1 mm) on the sample using the optical profilometer (MicroXAM-100 HR 3D surface profilometer). The obtained morphological features of the six spots are presented in Figure. 4.5.

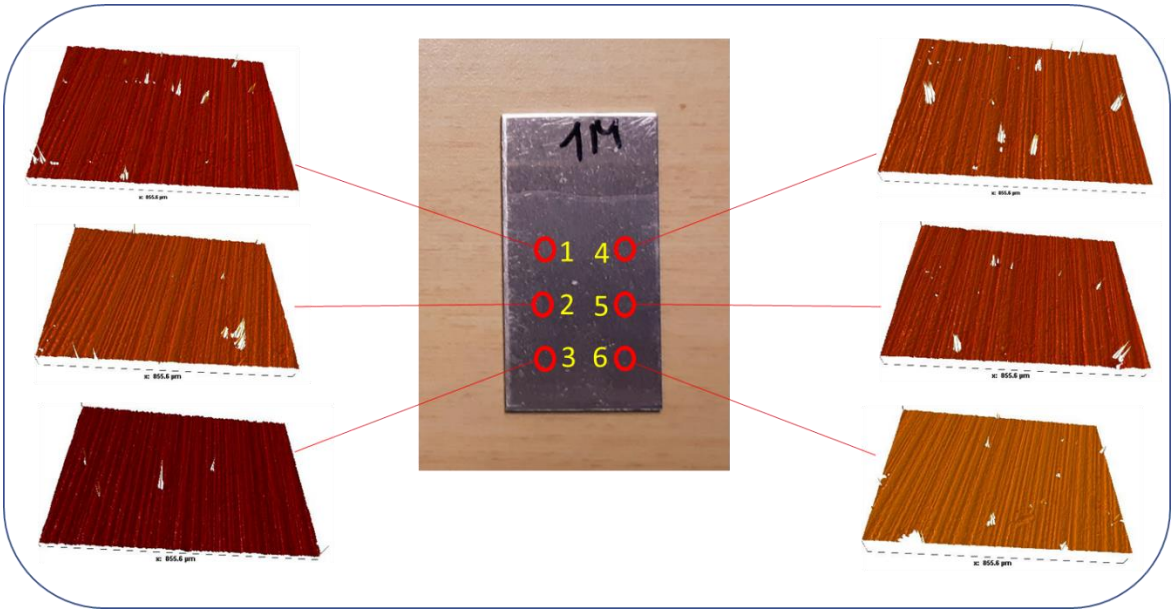

Figure. 4.5: Surface roughness measurement of 1 M sodium silicate thin film on Al substrate (blow-up view of the measured six spots)

The results confirm the uniformly deposited thin film on the aluminum surface with rms roughness of 0.53, 0.54, 0.52, 0.50, 0.53, and 0.51 µm, respectively on the measured spots. The proximity of these numbers demonstrates the uniformity of the 1 M sodium silicate thin film on the aluminum surface. The average roughness was found to be 0.52 ± 0.01 µm. This is also in agreement with the SEM analysis.

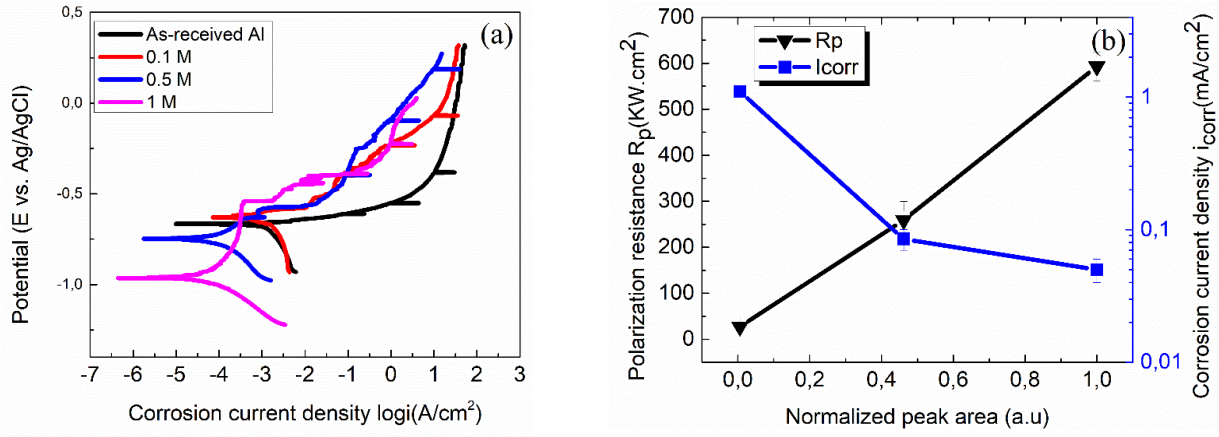

Figure. 4.6: (a) Potentiodynamic polarization curves of the as-received aluminum substrate, and sodium silicate thin films formed using 0.1, 0.5, and 1 M sodium silicate solution, (b) polarization resistance and corrosion current density variation of sodium silicate thin films on the aluminum substrates as a function of normalized Si-O-Si peak area.

The corrosion properties of fabricated sodium silicate thin films were analyzed by measuring potentiodynamic polarization resistances (R_p). Figure. 4.6 (a) show the potentiodynamic polarization by Tafel plots of the as-received aluminum substrate and sodium silicate thin films formed using 0.1 M, 0.5 M, and 1 M sodium silicate solution.

The polarization resistance R_p was calculated from the Stern-Geary Equation (4-2) as given below:

$$R_p = \frac{\beta a \beta c}{2.3 Icorr(\beta a + \beta c)} \qquad (4\text{-}2)$$

where βa and βc are the anodic and cathodic slopes of Tafel curves, respectively. I_{corr} is the corrosion current density that was determined from the extrapolation of the anodic and cathodic curves from these figures.

The calculated I_{corr}, R_p and E_{corr} for these four samples have presented in Table 4.1. E_{corr} of the as-received Al substrate is found to be -650 ± 22.5 mV which is close to our previously published results [26,31]. The E_{corr} of the sodium silicate thin films prepared from 0.1 M solution has been shifted negatively to -680 ± 47 mV. The further negative shifts of -707 ± 45 and -999 ± 33 mV corrosion potentials have been observed for the sodium silicate thin films prepared from 0.5 and 1 M solutions, respectively. These negative shifts of E_{corr} as compared to aluminum are due to the lower reduction potential of -2.71 V for Na with respect to -1.67 V for Al as given by Nernst Equation [32].

Table 4.1: Corrosion potential E_{corr}, corrosion current density I_{corr}, polarization resistance R_p and corrosion protection inhibition efficiency η of as-received aluminum substrate, sodium silicate thin films prepared on aluminum substrates fabricated using 0.1 M, 0.5 M, and 1 M solutions.

Sodium silicate concentration	Corrosion potential E_{corr} (mV)	Corrosion current density I_{corr} ($\mu A/cm^2$)	Polarization resistance R_p ($k\Omega.cm^2$)	Corrosion inhibition efficiency η (%)
0 M (as-received Al)	-650 ± 22.5	10.6 ± 3.3	10 ± 2	-
0.1 M	-680 ± 47	1.1 ± 0.03	27.5 ± 0.5	89.62
0.5 M	-707 ± 45	0.085 ± 0.01	259 ± 40	99.19
1 M	-999 ± 33	0.05 ± 0.01	593 ± 32	99.52

On the other hand, the as-received aluminum substrates have exhibited a corrosion current density (I_{corr}) of 10.6 ± 3.3 μA/cm^2 and a polarization resistance (R_p) of 10 ± 2 kΩ.cm^2. While the I_{corr} and R_p of the sodium silicate thin film prepared from 0.1 M sodium silicate were found to be 1.1 ± 0.03 μA/cm^2 and 27.5 ± 0.5 kΩ.cm^2, respectively. The sodium silicate thin films prepared from the 0.5 M solution provided the I_{corr} and R_p values of 0.085 ± 0.01 μA/cm^2 and 259 ± 40 kΩ.cm^2, respectively. The I_{corr} has been further reduced to 0.05 ± 0.01 μA/cm^2 and R_p has been increased to 593 ± 32 kΩ.cm^2 for the sodium silicate thin films prepared from 1 M solution. It is to mention that in our study, the polarization resistance is found to be ~ 60 times higher than the as-received aluminum substrates. A similar observation was reported by Zhang *et al.* [24] on titanium alloy substrate using different sodium silicate concentrations through the micro arc oxidation process. They varied the concertation of sodium silicate from 0.03 to 0.12 M (4 to 16 g/L) with the pH in the range of 11 to 12. Their reported current density of 0.02 μA/cm^2 for the higher concentration (0.12 M), is comparable to our thin films fabricated using 0.1 M solution. They found that the higher concentration of sodium silicate assisted in achieving lower corrosion current density. Similarly, by inhibition process using 0.2 M concentration of sodium silicate, Anaee *et.al* [33], observed their corrosion current density to be 30.69 μA/cm^2. In comparison, we have observed a much lower current density of 0.05 ± 0.01 μA/cm^2 for the thin film fabricated on Al substrate using 1M sodium silicate solution.

As shown in Figure. 4.1 (a), the increase in the intensity of the ATR-FTIR peak area from 862 to 1306 cm^{-1} could be attributed to the increase in its film thickness. It is comparable to the results obtained from the potentiodynamic polarization curves. Though, the corrosion potential (E_{corr}) reduces with the increase of sodium silicate thin film's thickness, the polarization resistance (R_p) is found to be increasing. Similarly, the corrosion current density (I_{corr}) reduces with the

increase in the thickness of sodium silicate thin films. It is well known that higher R_p and lower I_{corr} represent better corrosion protection.

Figure. 4.6 (b) shows that the polarization resistance and corrosion current density plotted against the ATR-FTIR peak area. The peak area signifies thickness of the sodium silicate thin film. The figure shows that R_p increases linearly with increased ATR-FTIR peak area and inversely decreased with corresponding I_{corr}. The increase of thin film thickness helps to protect aluminum against the corrosive ion's penetration. The corrosion protection efficiency η (%) of sodium silicate thin film was evaluated using Equation (4-3):

$$\eta(\%) = \frac{I_{corr\ (Al)} - I_{corr\ (\text{thin films})}}{I_{corr\ (Al)}} \times 100 \qquad (4\text{-}3)$$

Where $I_{corr\ (Al)}$ is the corrosion current density of as-received aluminum substrate and $I_{corr\ (thin\ films)}$ is the corrosion current density of the sodium silicate thin films.

The corrosion inhibition efficiencies of the sodium silicate thin film prepared from a solution of 0.1, 0.5 and 1M are found to be 89.62, 99.19 and 99.52 %, respectively. In the study published by Yuan *et.al.* [34], the inhibition efficiency η (%) of the sodium silicate on steel substrate was calculated as 95.88 %. Similarly, Gao *et al.* [17] investigated the inhibition efficiency of 99.40 % for magnesium substrates. The present study attained an inhibition efficiency of 99.52 % for sodium silicate thin films on the aluminum substrate. It is observed in the literature that the aluminosilicate formation take place at the interface between the aluminum substrate and sodium silicate thin film [23]. Therefore, in our work, the increase of inhibition efficiency with increased sodium silicate concentration could be ascribed to the thickness of the sodium silicate thin film as well as the interfacial layer.

On the other hand, PosiTector 6000 probe has been used to determine the thickness of the fabricated thin films. This tool has an error of ± 0.1 µm, which makes the thickness measurement for the samples fabricated with 0.1 M sodium silicate not accurate. Further, the film thickness of both 0.5 and 1 M sodium silicate thin film coating was 0.4 ± 0.2 and 0.55 ± 0.15 µm, respectively.

The increase in the sodium silicate molar concentration leads to the formation of thicker thin films, which explain the better corrosion properties of the sodium silicate thin film fabricated from 1 M sodium silicate solution.

To study the effect of surface pre-treatment on the corrosion properties of the fabricated sodium silicate thin films, sodium hydroxide (NaOH) chemical etching process was performed. Afterward, 1 M sodium silicate ultrasonication dip-coating was performed on both as-received (without etching) and etched aluminum substrates.

The obtained Tafel curves of the sodium silicate coatings on both as-received aluminum substrate and etched aluminum substrate are presented in Figure 4.7 (a), and the corresponding corrosion parameters are summarized in Table 4.2. The sodium silicate thin film fabricated on as-received aluminum (without etching) exhibited a corrosion current density (I_{corr}) of 0.1 µA/cm^2 compared to 0.19 µA/cm^2 for the thin film fabricated on etched aluminum substrate. The higher value of the corrosion current density of sodium silicate thin film coatings on the etched aluminum substrate could be due to surface irregularities of the thin film on metallic substrate (Figure 4.8).

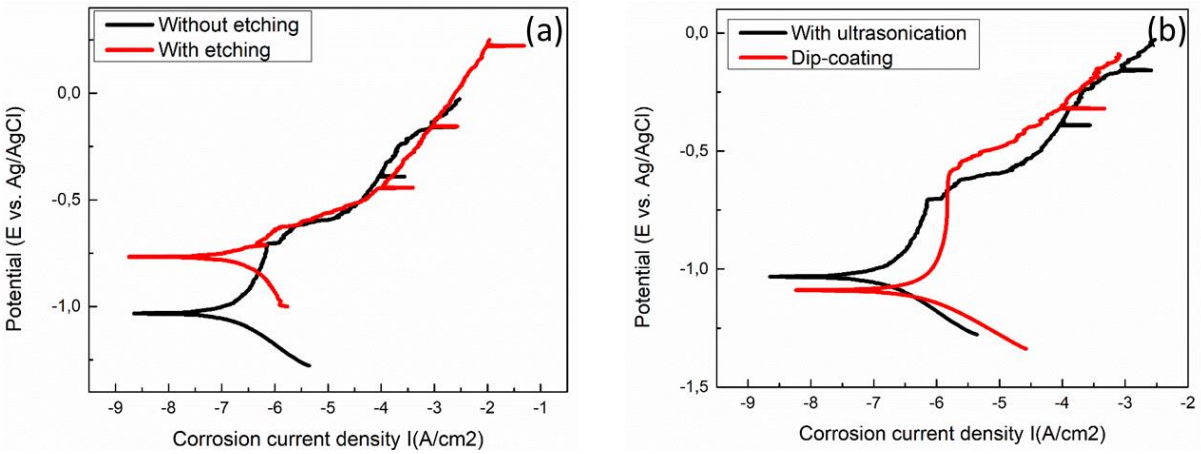

Figure 4.7: Potentiodynamic polarization curves: (a) 1 M sodium silicate thin films deposited by ultrasonication process on clean aluminum substrate (Without etching) and etched aluminum substrate (with etching). (b) Potentiodynamic polarization curves of 1 M sodium silicate thin films deposited by ultrasonication process and simple dip-coating process on clean aluminum substrate.

Table 4.2: The polarization resistance (R_p) and the corrosion current density (I_{corr}) of the sodium silicate thin films fabricated on aluminum substrates using a simple dip-coating process and ultrasonication process with and without etching.

		R_p ($k\Omega.cm^2$)	I_{corr} ($\mu A/cm^2$)
Dip-coating process		64.5	0.4
Ultrasonication process	With etching	157	0.19
	Without etching	227	0.10

In a similar study, Sun *et al.* [35] studied the effect of chemical etching on the corrosion properties of chromium-based coatings on aluminum substrates. The etched sample using HF-H_2SO_4 solution (1.5 mL HF, 10 mL H_2SO_4 and 90 mL of H_2O) exhibited a corrosion current density value of 8.9 × 10^{-3} µA/cm^2 compared to 5.3 × 10^{-3} µA/cm^2 for the sample coated without prior etching. The high I_{corr} value of the etched sample indicates its lower corrosion protection properties compared to the sample coated without etching.

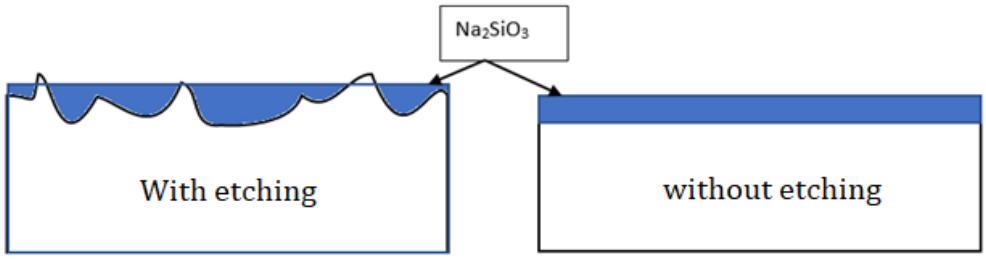

Figure 4.8: Model of sodium silicate thin films deposited by ultrasonication process on aluminum substrate (without etching) and on etched aluminum substrate.

Furthermore, to study the effect of ultrasonication on corrosion properties of sodium silicate thin films, two samples were fabricated using ultrasonication and simple dip-coating process (without ultrasonication) under same experimental conditions. Afterward, the corrosion properties of the two samples were evaluated using potentiodynamic polarization tests (Figure 4.7 (b)). The corrosion current density of the sample fabricated by ultrasonication process was 0.1 µA/cm^2 compared to 0.4 µA/cm^2 for the sample fabricated by the simple dip-coating process. This indicates better corrosion protection for ultrasonication process compared to simple dip-coating process.

In a related study, Sheng *et al.* [36], investigated the role of ultrasonication deposition of phosphate coatings on Al for corrosion protection. It was observed that ultrasonication reduces the particle size of phosphate coatings, resulting in the formation of a denser thin film with improved corrosion property compared to the samples without ultrasonication.

For practical application, it is important to study the stability of the thin films on Al substrate. Consequently, the adhesion test was performed on sodium silicate thin film using ASTM D3359-02 standard. The test was performed on the 1 M sodium silicate thin film (Figure 4.9). According to the ASTM D3359-02 standard, the average adhesion of the sodium silicate thin film showed robust adhesion on the aluminum substrate with a 5B rating on cross-hatch scale.

Figure 4.9: Adhesion test on Al substrate coated with sodium silicate thin film formed using 1 M sodium silicate solution.

4.4 **Conclusion**

Sodium silicate thin films were fabricated on laminated AA6061-T6 aluminum alloy substrates by a facile ultrasonic dip-coating process. ATR-FTIR exhibited the presence of Si-O-Si

bond with an absorption peak at 1207 cm^{-1} and possible Si-O-Na bond at 943 cm^{-1}. The complementary study by EDS analysis supports the compositions having the elemental percentage of Na, Si and O are 3.30, 24.48 and 72.22, respectively. The corrosion resistance properties of sodium silicate thin film analyzed by Tafel plots provided the polarization resistance of 593 ± 32 $k\Omega.cm^2$, which is ~60 times higher than that of aluminum substrate. The corresponding corrosion current density (I_{corr}) is found to be ~ 100 times lower for silicate thin film compared to the as-received aluminum substrate. The surface pretreatment by chemical etching before the formation of sodium silicate thin films does not improve the corrosion properties. These results of this study shows promises to effective protection against corrosion, which can find potential in many industrial applications.

References

[1] W.D. Compton, N.A. Gjostein, Materials for Ground Transportation, Sci. Am. 255 (1986) 92–100.

[2] H. Ohno, P. Nuss, W.-Q. Chen, T.E. Graedel, Deriving the Metal and Alloy Networks of Modern Technology, Environ. Sci. Technol. 50 (2016) 4082–4090.

[3] M. Liu, Y. Guo, J. Wang, M. Yergin, Corrosion avoidance in lightweight materials for automotive applications, Npj Mater. Degrad. 2 (2018) 24.

[4] J.-P. Immarigeon, R.T. Holt, A.K. Koul, L. Zhao, W. Wallace, J.C. Beddoes, Lightweight materials for aircraft applications, Mater. Charact. 35 (1995) 41–67.

[5] T.N. Nguyen, J.B. Hubbard, G.B. McFadden, A mathematical model for the cathodic blistering of organic coatings on steel immersed in electrolytes., J. Coatings Technol. (1991).

[6] T.L. Metroke, R.L. Parkhill, E.T. Knobbe, Passivation of metal alloys using sol–gel-derived materials — a review, Prog. Org. Coatings. 41 (2001) 233–238.

[7] J. Zhao, L. Xia, A. Sehgal, D. Lu, R.L. McCreery, G.S. Frankel, Effects of chromate and chromate conversion coatings on corrosion of aluminum alloy 2024-T3, Surf. Coatings Technol. 140 (2001) 51–57.

[8] W.J. Clark, J.D. Ramsey, R.L. McCreery, G.S. Frankel, A Galvanic Corrosion Approach to Investigating Chromate Effects on Aluminum Alloy 2024-T3, J. Electrochem. Soc. 149 (2002) B179.

[9] C. Pellerin, S.M. Booker, Reflections on hexavalent chromium: Health hazards of an industrial heavyweight, Environ. Health Perspect. 108 (2000) 402–407.

[10] H.J. Gibb, P.S. Lees, P.F. Pinsky, B.C. Rooney, Lung cancer among workers in chromium chemical production., Am. J. Ind. Med. 38 (2000) 115–26.

[11] J.W. WOOD, J.S. BEECHER, P.S. LAURENCE, Some Experiences With Sodium Silicate As a Corrosion Inhibitor in Industrial Cooling Waters, Corrosion. 13 (1957) 41–46.

[12] X. Yang, P. Roonasi, A. Holmgren, A study of sodium silicate in aqueous solution and sorbed by synthetic magnetite using in situ ATR-FTIR spectroscopy, J. Colloid Interface Sci. 328 (2008) 41–47.

[13] M. Hara, R. Ichino, M. Okido, N. Wada, Corrosion protection property of colloidal silicate film on galvanized steel, Surf. Coatings Technol. 169 (2003) 679–681.

[14] L.. García-Cerda, O. Mendoza-González, J.. Pérez-Robles, J. González-Hernández, Structural characterization and properties of colloidal silica coatings on copper substrates, Mater. Lett. 56 (2002) 450–453.

[15] R.P. Socha, J. Fransaer, Mechanism of formation of silica–silicate thin films on zinc, Thin Solid Films. 488 (2005) 45–55.

[16] B. Salami, A. Afshar, A. Mazaheri, The effect of sodium silicate concentration on microstructure and corrosion properties of MAO-coated magnesium alloy AZ31 in simulated body fluid, J. Magnes. Alloy. 2 (2014) 72–77.

[17] H. Gao, Q. Li, F. Chen, Y. Dai, F. Luo, L. Li, Study of the corrosion inhibition effect of sodium silicate on AZ91D magnesium alloy, Corros. Sci. 53 (2011) 1401–1407.

[18] A.S. Hamdy, D.P. Butt, Environmentally compliant silica conversion coatings prepared by sol-gel method for aluminum alloys, Surf. Coatings Technol. 201 (2006) 401–407.

[19] A.S. Hamdy, Corrosion protection of aluminum composites by silicate/cerate conversion coating, Surf. Coatings Technol. 200 (2006) 3786–3792.

[20] O. Lopez-Garrity, G.S. Frankel, Corrosion inhibition of AA2024-t3 by sodium silicate, Electrochim. Acta. 130 (2014) 9–21.

[21] G.P. Thim, M.A.S. Oliveira, E.D.A. Oliveira, F.C.L. Melo, Sol-gel silica film preparation from aqueous solutions for corrosion protection, J. Non. Cryst. Solids. 273 (2000) 124–128.

[22] R.U. Din, K. Bordo, N. Tabrizian, M.S. Jellesen, R. Ambat, Steam based conversion coating on AA6060 alloy: Effect of sodium silicate chemistry and corrosion performance, Appl. Surf. Sci. 423 (2017) 78–89.

[23] R. Gaggiano, P. Moriamé, M. Biesemans, I. De Graeve, H. Terryn, Influence of SiO 2 /Na 2 O ratio and temperature on the mechanism of interaction of soluble sodium silicates with porous anodic alumina, Surf. Coat. Technol. 206 (2011) 1269–1276.

[24] Y.L. Zhang, C.H. Li, M. Hu, Y.M. Zhang, Influence of Na2SiO3 Concentration on the Corrosion Behavior of TC4 Ceramic Coatings, Adv. Mater. Res. 971–973 (2014) 85–88.

[25] R. Gaggiano, P. Moriamé, M. Biesemans, I. De Graeve, H. Terryn, Influence of SiO2/Na2O ratio and temperature on the mechanism of interaction of soluble sodium silicates with porous anodic alumina, Surf. Coatings Technol. 206 (2011) 1269–1276.

[26] J. Xiong, D.K. Sarkar, X.-G. Chen, Superhydrophobic honeycomb-like cobalt stearate thin films on aluminum with excellent anti-corrosion properties, Appl. Surf. Sci. 407 (2017)

361–370.

[27] Z. Zhao, Y. Song, X. Min, Y. Liang, L. Chai, M. Shi, XPS and FTIR studies of sodium arsenate vitrification by cullet, J. Non. Cryst. Solids. 452 (2016) 238–244.

[28] J.-D. Brassard, D.K. Sarkar, J. Perron, Synthesis of Monodisperse Fluorinated Silica Nanoparticles and Their Superhydrophobic Thin Films, ACS Appl. Mater. Interfaces. 3 (2011) 3583–3588.

[29] D.K. Sarkar, D. Brassard, M.A. El Khakani, L. Ouellet, Dielectric properties of sol–gel derived high-k titanium silicate thin films, Thin Solid Films. 515 (2007) 4788–4793.

[30] F.T. Ling, J.E. Post, P.J. Heaney, J.D. Kubicki, C.M. Santelli, Fourier-transform infrared spectroscopy (FTIR) analysis of triclinic and hexagonal birnessites, Spectrochim. Acta Part A Mol. Biomol. Spectrosc. 178 (2017) 32–46.

[31] N. Xu, D.K. Sarkar, X. Grant Chen, H. Zhang, W. Tong, Superhydrophobic copper stearate/copper oxide thin films by a simple one-step electrochemical process and their corrosion resistance properties, RSC Adv. 6 (2016) 35466–35478.

[32] Z. AHMAD, Principles of corrosion engineering and corrosion control, 2006.

[33] R.A.M. Anaee, Sodium Silicate and Phosphate as Corrosion Inhibitors for Mild Steel in Simulated Cooling Water System, Arab J Sci Eng. 39 (2014) 153–162.

[34] M. Yuan, J. Lu, G. Kong, Surface & Coatings Technology Effect of SiO 2 : Na 2 O molar ratio of sodium silicate on the corrosion resistance of silicate conversion coatings, Surf. Coat. Technol. 204 (2010) 1229–1235.

CHAPTER 5

EVALUATION OF THE CORROSION INHIBITION PERFORMANCE OF NON-CHROMATE CORROSION INHIBITORS FOR ALUMINUM ALLOY

CHAPTER 5 : EVALUATION OF THE CORROSION INHIBITION PERFORMANCE OF NON-CHROMATE CORROSION INHIBITORS FOR ALUMINUM ALLOY

Abstract

In this work, the behavior of sodium silicate (Na_2SiO_3), manganese sulfate monohydrate ($MnSO_4.H_2O$) and ammonium metavanadate (NH_4VO_3) as corrosion inhibitors for laminated AA6061-T6 aluminum alloy (Al) was investigated. The polarization resistance (R_p) of the Al substrate immersed in 0.1 M NaCl solution was found to be 13 $k\Omega.cm^2$. In comparison, the R_p of the Al substrate immersed in 0.1 M NaCl in the presence of Na_2SiO_3, $Na_2SiO_3/MnSO_4.H_2O$, and Na_2SiO_3/NH_4VO_3 inhibitors was found to be 100, 133 and 679 $k\Omega.cm^2$, respectively. The best inhibition result was obtained when the mixture of the inhibitors was used indicating an R_p of 722 $k\Omega.cm^2$. The maximum percentage of the corroded area calculated from the scanning electron microscopy (SEM) images was found to be 5.7 % for Al substrate immersed in 0.1 M NaCl, which decreases to 0.06 % when the mixture of the inhibitors was used. The synergetic effects between the three inhibitors were studied and the results illustrated that the combination of Na_2SiO_3, $MnSO_4.H_2O$, and NH_4VO_3 provided the best corrosion inhibition properties for Al in aqueous NaCl environments.

5.1 **Introduction**

Aluminum (Al) and its alloys have several applications in aerospace [1], aircraft [2], automobiles [3], marine industry [4], computer components, food packaging [5], and construction [6] as it exhibits some favorable properties like low density, high ductility, excellent strength-to-weight ratio, and high stiffness [7]. Being a reactive metal, Al reacts with atmospheric oxygen to form a passive and stable protective oxide layer (Al_2O_3), which provides protection from corrosion in neutral environments [8]. However, Al is susceptible to corrosion in aggressive mediums, such as seawater, which limits its potential applications. Hence, to utilize the advantages of Al and its alloys, it is essential to explore more corrosion protection strategies, particularly for applications in marine or highly corrosive environments.

Traditionally, chromate surface treatments technologies [9,10] are used for corrosion protection of Al alloys. But the chromate ions have raised some health and human safety concerns, resulting in the ban of these technologies in recent times [11] . Thus, researchers need to investigate alternative non-toxic or less toxic corrosion protection techniques. Corrosion inhibition is one such technique, which reduces the corrosion rate of Al when exposed to highly corrosive environments. In this technique, silicate-based materials are investigated for their buffering ability, polymerizing capability, heat and chemical stability [12]. They are used as inhibitors, which reduce the corrosion rate of metals in a corrosive environment [13,14]. Garrity *et al*.[13] investigated the corrosion protection of aluminum through the inhibition process by incorporating sodium silicate in the 0.1 M NaCl aqueous solution. They found that the corrosion protection mechanism is due to the formation of aluminosilicate complex that adsorbs on the aluminum substrate, preventing penetration of corrosive ions.

Further, a frequent contender to chrome is manganese-based compounds. These compounds are studied for their corrosion inhibition properties as manganese exhibits multiple oxidation states similar to chrome. Even though, the corrosion inhibition ability of the manganese is not as effective as the latter (Chromium) mainly for low pH environment, the former (Manganese) inhibits the corrosion of Al at high pH values [15]. This inhibition is due to the reduction of Mn(VII) in alkaline media, which leads to the formation of MnO_2, considered as a less soluble species [16]. In another study, Agnesia *et al.* [17] reported the corrosion inhibition of Al by potassium permanganate ($KMnO_4$) in an alkaline aqueous solution. They found that the corrosion inhibition efficiency increases along with the concentration of $KMnO_4$. The formation of Al-$KMnO_4$ complex on the metal surface prevents the penetration of corrosive ions to the substrate and thus increases the corrosion performance of the inhibitor.

Another effective environmental alternative inhibitor to chromium source is vanadium compounds. These compounds were considered as suitable corrosion inhibitors for Al alloys in several studies [18–20]. As reported, the inhibition property of vanadium compounds in alkaline aqueous solutions are related to tetrahedrally-coordinated V^{+5} anions, such as VO_4^{3-} and $VO(OH)^-_2$ [19]. These anions decrease the kinetics of oxygen reduction, which are the dominant cathodic reactions in the corrosion process. In this context, Ralston *et al.* [18] studied the corrosion inhibition of Al by aqueous vanadium species. They observed that the addition of sodium metavanadate ($NaVO_3$) has no effect at acidic medium but led to a noticeable increase in the corrosion protection in alkaline medium. They concluded that the inhibition of Al by $NaVO_3$ in sodium chloride (NaCl) solutions was associated with the formation of tetrahedrally coordinated vanadate. However, the octahedrally coordinated vanadate predominated in the acidic

environments does not seem to provide inhibition and may accelerate corrosion under deaerated conditions.

Although studies on the corrosion inhibition of Al by each compound (sodium silicate, manganese or vanadium) are abundant in the literature, studies on the synergetic effect between the three inhibitors are less reported. The present work aims to illustrate the corrosion inhibition effect of sodium silicate (Na_2SiO_3), manganese sulfate monohydrate ($MnSO_4.H_2O$) and ammonium metavanadate (NH_4VO_3) on AA6061 Al alloy substrates in corrosive environments. An optimized combination of all three inhibitors is also studied to analyze the synergetic effect between the inhibitors where the corrosion properties of the samples are investigated using electrochemical tests. The surface morphology and chemical composition of the samples are also analyzed after the corrosion tests to compare the performance of each inhibitor.

5.2 **Experimental**

In this work the AA6061 Al alloy with the chemical composition of Al 97.9 wt.%, Mg 1.08 wt.%, Si 0.63 wt.%, Mn 0.52 wt.%, Cu 0.32 wt.%, Fe 0.17 wt.%, Ti 0.02 wt.%, and V 0.01 wt.%, was used as substrates. Each Al substrates with the size of one by one inch are ultrasonically degreased in a soap solution and cleaned in ethanol and deionized water for 30 minutes. Furthermore, the samples are mounted in the electrochemical cell and expose to corrosive solutions of 0.1 M sodium chloride (NaCl, pH of 5.9) with the presence of inhibitors.

Three different inhibitors, sodium silicate (Na_2SiO_3) with the concentration of 3×10^{-2} M, manganese sulfate monohydrate ($MnSO_4.H_2O$) with the concentration of 3×10^{-4} M, and ammonium metavanadate (NH_4VO_3) with the concentration of 3×10^{-4} M. The inhibitors are added to the NaCl aqueous solution and kept for 24 hours to assess their corrosion inhibitive properties

on Al using electrochemical studies. For each inhibitor, the tests have been repeated in triplicate. Solartron analytical 1252 and SI 1287 potentiostat equipped with a 300 cm^3 volume flat cells are used to perform the open circuit potential (OCP), electrochemical impedance spectroscopy (EIS), and potentiodynamic polarization (Tafel) tests. A three electrodes set-up, consisting of a platinum mesh (counter electrode), a silver/silver-chloride (Ag/AgCl) (reference electrode), and the Al samples (working electrodes) is employed. The frequency range of the EIS study is fixed between 10^{-2} and 10^5 Hz and an amplitude of 20 mV with respect to OCP. The potentiodynamic polarization curves are scanned in a range of -300 mV to 1200 mV with respect to OCP. The morphological and elemental characterizations of the samples are performed by scanning electron microscopy (SEM, JEO JSM-6480 LV) equipped with energy dispersive X-ray spectroscopy (EDS). Additionally, the image analysis software, Clemex (CLEMEX JS-2000, PE4.0), has been used to determine the percentage of the corroded area on Al substrates.

5.3 **Results and discussion**

Figure 5.1 shows the open circuit potential (OCP) curves of Al substrate immersed in 0.1 M NaCl solution without and with the presence of Na_2SiO_3, $Na_2SiO_3/MnSO_4.H_2O$, Na_2SiO_3/NH_4VO_3, and $Na_2SiO_3/MnSO_4.H_2O/NH_4VO_3$ inhibitors. The OCP curve of Al substrate immersed in 0.1 M NaCl solution stabilized at around -734 mV (shown in Table 5.4) and this value is in good agreement with the values reported in the literature [22,23]. Furthermore, the OCP curve in the presence of Na_2SiO_3 inhibitor shows a shift toward positive potential values and stabilized at around -678 mV. This shift is related to the anodic inhibition nature of sodium silicate. Similar results have been reported in different studies [13,24,25]. An anodic inhibitor such as sodium silicate reacts with Al^{3+}ions, forming an insoluble film, such as aluminosilicate, that result in a shift of the potential towards more positive values [26].

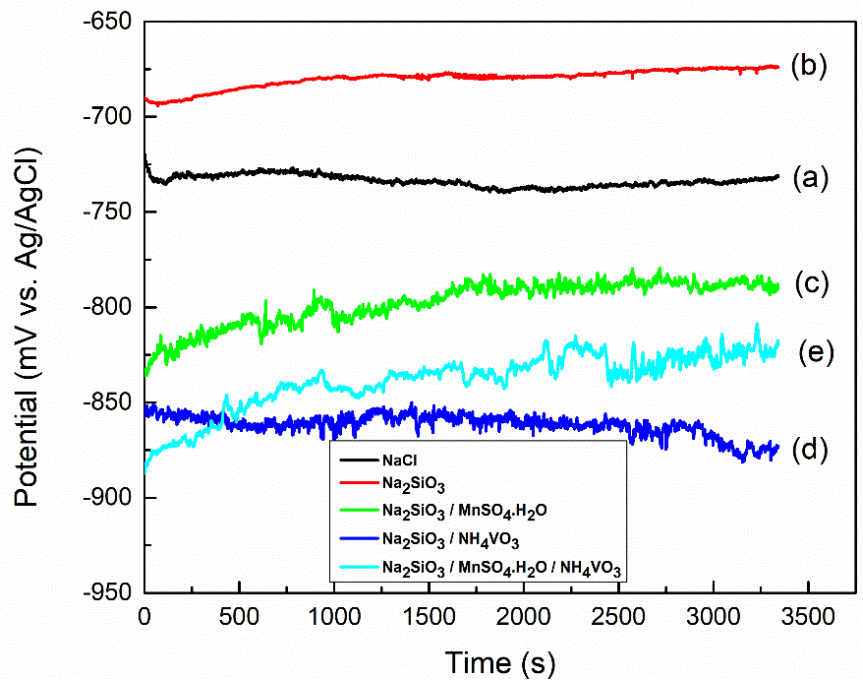

Figure 5.1: Open circuit potential (OCP) curves of (a) Al substrate immersed in 0.1 M NaCl without inhibitors, and with the presence of (b) Na_2SiO_3, (c) Na_2SiO_3/ $MnSO_4.H_2O$, (d) Na_2SiO_3 /NH_4VO_3, (e) and Na_2SiO_3/$MnSO_4.H_2O$/NH_4VO_3.

Contrarily, the OCP curve for the sample contained in Na_2SiO_3/ $MnSO_4.H_2O$ inhibitors shifted towards a more negative potential (-798 mV) compared to -734 mV for Al substrate. Madden *et al.* [27] has previously studied the effect of potasium permanganate ($KMnO_2$) on the corrosion properties of Al. They found that the OCP values decrease to lower potentials after 24 h of immersion in sodium chloride aqueous solution. The authors attributed the steady drop in the potential to the reduction of the manganese oxide deposited on Al, and as the reduction from manganese (IV) to (III) to (II) occurs, the potential of the system dropped toward the Nernst potential of the lowest valence oxide until all the oxide had been reduced. Furthermore, the OCP

curve for the sample contained Na_2SiO_3/ NH_4VO_3 inhibitors stabilized at a further lower value of -861 mV. Ralston *et al.* [28] reported a similar decreasing tendency of OCP curve for Al in the presence of sodium metavanadate ($NaVO_3$). They have reported that the addition of $NaVO_3$ leads to a negative shift below -790 mV compared to -650 mV for the Al substrate in NaCl solution. The negative shift as compared to Al could be due to the decrease of the intermetallic phases dissolution by vanadium, which leads to less distributed copper on the surface. It is to mention that copper has a positive reduction potential of +340 mV with respect to -166 mV for Al as given by Nernst equation. Interestingly, the OCP curve of the sample in presence of Na_2SiO_3/ $MnSO_4.H_2O$/ NH_4VO_3 stabilized at the value of -838 mV, which is an intermediate value between the OCP curves of the samples inhibited with Na_2SiO_3/ $MnSO_4.H_2O$ and Na_2SiO_3 /NH_4VO_3.

Figure 5.2 shows the EIS measurements of Al substrate immersed in 0.1 M NaCl solution and with the presence of different inhibitors and their mixture, Na_2SiO_3, Na_2SiO_3/$MnSO_4.H_2O$, Na_2SiO_3/NH_4VO_3, and Na_2SiO_3/$MnSO_4.H_2O$/NH_4VO_3 for the duration of 24 h. Figure 5.2 (a) presents the Nyquist plots of Al substrate immersed in 0.1 M NaCl and with the presence of Na_2SiO_3, Na_2SiO_3/$MnSO_4.H_2O$, Na_2SiO_3/NH_4VO_3, and Na_2SiO_3/$MnSO_4.H_2O$/NH_4VO_3, which depict the imaginary component (-Z'') vs the real component (Z'). The Nyquist plot of the Al substrate (magnified in the inset of Figure 5.2 (a)) is composed of a small semi-circle at high frequencies followed by a linear part at low frequencies. The semi-circle indicates the charge transfer resistance (R_{ct}) of 6.7 kΩ.cm^2. The linear part at low frequencies in the Nyquist plot corresponds to Warburg impedance and it is due to the diffusion of the electrolyte into the Al substrate [29].

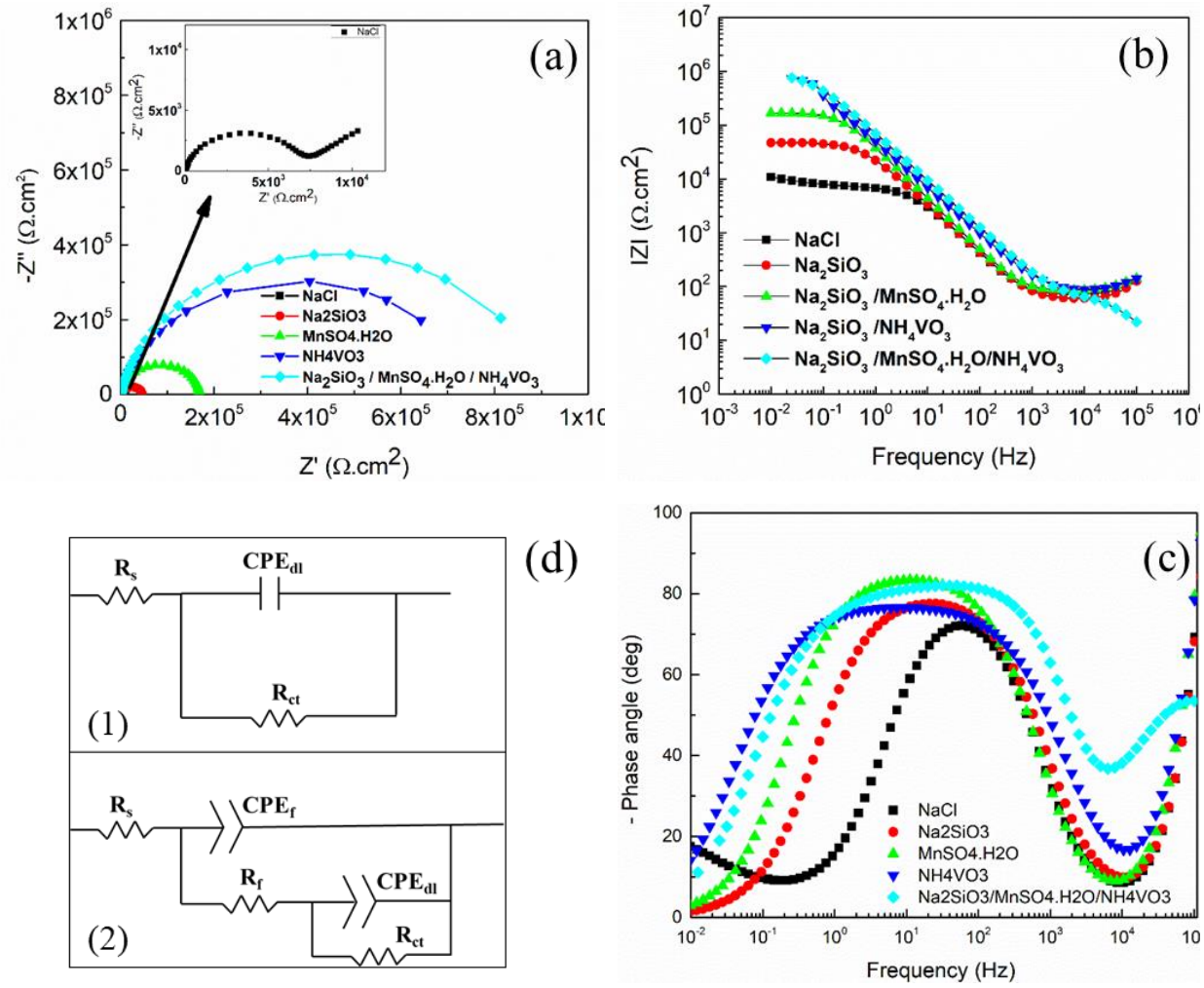

Figure 5.2: (a) Nyquist plots, (b) Bode modulus diagrams, (c) Bode phase diagrams and (d) Equivalent circuit of Al substrate immersed in 0.1 M NaCl without inhibitors, and with the presence of Na_2SiO_3, Na_2SiO_3/ $MnSO_4.H_2O$, Na_2SiO_3 /NH_4VO_3, and Na_2SiO_3 /$MnSO_4.H_2O$ /NH_4VO_3.

On the contrary, in the presence of Na_2SiO_3, Na_2SiO_3/$MnSO_4.H_2O$, Na_2SiO_3/NH_4VO_3, or Na_2SiO_3/$MnSO_4.H_2O$/NH_4VO_3 as inhibitors in 0.1 M NaCl solution, the Nyquist plots show only one semi-circle. A higher R_{ct} value of 47 kΩ.cm^2 was observed for the sample in the presence of

Na_2SiO_3 as an inhibitor. Such increase of the R_{ct} value could be due to the formation of a protective layer which acts as a barrier to oxygen diffusion into the metallic surface [30]. A further increase of the R_{ct} of 169 kΩ.cm^2 is observed for the sample in the presence of Na_2SiO_3/ $MnSO_4.H_2O$ as an inhibitor.

Mohammadi *et al.* [31] have studied the inhibition performance of potassium permanganate ($KMnO_4$) on Al in 3.5 wt.% NaCl solution. They found that the R_{ct} values increase from 5.5 to 27.2 kΩ.cm^2 with the increase of the concentration of $KMnO_4$ from 0.01 M to 0.1 M, respectively.

Furthermore, the presence of Na_2SiO_3/NH_4VO_3 as an inhibitor in 0.1 M NaCl solution resulted in a much higher R_{ct} of 753 kΩ.cm^2, which indicates that vanadium-based inhibitor has good protection against corrosion in presence of sodium silicate. Kharitonov *et al.* [20] reported that the inhibition process of vanadium-based inhibitors in alkaline environments involves two steps. First, V^{+5} vanadates are reduced to V^{+4} or V^{3+} species on the surface of the cathodic intermetallic phases and formed a mixed-valence V^{+5}/ V^{+4} polymerized compounds. Then, these compounds are precipitated on the Al surface and form a thin protective layer on the substrate [20]. The highest R_{ct} of 926 kΩ.cm^2 is achieved for the sample in the presence of mixed $Na_2SiO_3/MnSO_4.H_2O/NH_4VO_3$ as an inhibitor. These results could be due to a synergetic effect between the inhibitors leading to the formation of a complex protective layer on the Al surface.

Figure 5.2 (b) shows the Bode modulus diagrams of the Al substrate in the aqueous solution of 0.1 M NaCl and with the presence of Na_2SiO_3, $Na_2SiO_3/MnSO_4.H_2O$, Na_2SiO_3/NH_4VO_3, and $Na_2SiO_3/MnSO_4.H_2O/NH_4VO_3$. The impedance modulus |Z| has been presented with respect to frequency. The modulus of the impedance is given by: $|Z|=\sqrt{(Z' + Z'')^2}$, where Z' and Z'' are the

real and the imaginary parts of the impedance. Further, the imaginary part of the impedance Z'' is given by the expression: Z''=1/jωC, where; j=-1 is the imaginary unit, ω is the angular frequency (ω=2πf, f is the frequency), and C is the capacitance of the passivated layer. At a given capacitance, the value of Z'' increases with the decrease of the frequencies. Consequently, the higher |Z| value at the low-frequency region could signify a better barrier property of the thin film [32]. Thus, to evaluate the effectiveness of corrosion protection of the inhibitors, the values of the impedance at a low-frequency value of 0.1 Hz were plotted and presented in Figure 5.3.

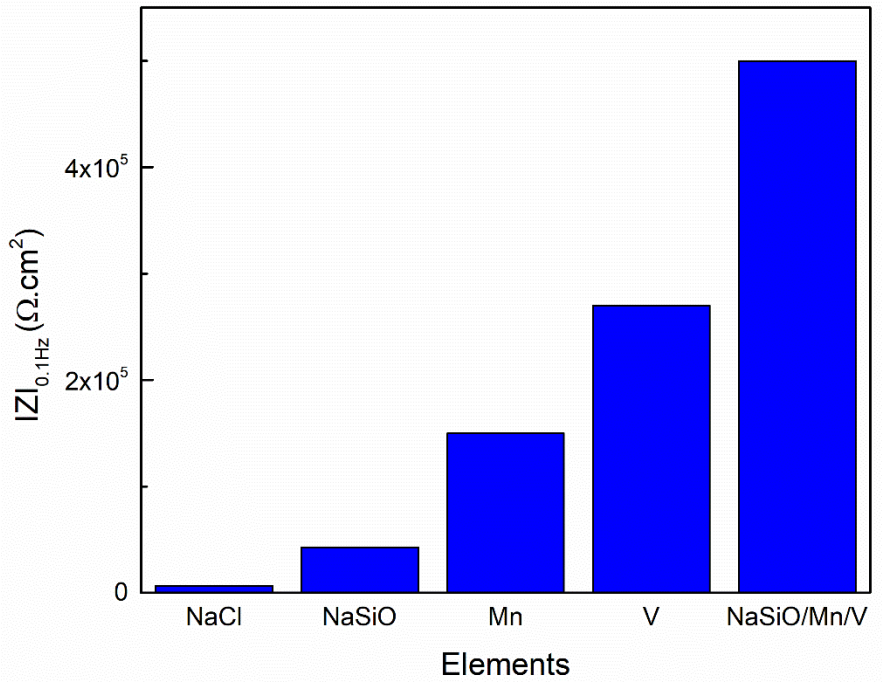

Figure 5.3: The impedance |Z| at the frequency of 0.1 Hz of Al substrate immersed in 0.1 M NaCl solution and with the presence of Na_2SiO_3, Na_2SiO_3/$MnSO_4.H_2O$, Na_2SiO_3/NH_4VO_3, and Na_2SiO_3/$MnSO_4.H_2O$/NH_4VO_3.

The impedance modulus |Z| for Al substrate in 0.1 M NaCl solution is found to 0.7 kΩ.cm^2, and that has been increased systematically to 42, 150, 270, and 500 kΩ.cm^2 for the Al substrates with the presence of Na_2SiO_3, $Na_2SiO_3/MnSO_4.H_2O$, Na_2SiO_3/NH_4VO_3 and $Na_2SiO_3/MnSO_4.H_2O/NH_4VO_3$ inhibitors, respectively. At low-frequency region, dominated part of the modulus of the impedance is related to the capacitance of the passivated layers on the Al substrates in presence of different inhibitors as given in Equation (5-1).

$$Z'' = \frac{1}{j\omega C} \tag{5-1}$$

Where Z'' is the imaginary part of the impedance, j=-1 is the imaginary unit, ω is the angular frequency ($\omega=2\pi f$, f is the frequency), and C is the capacitance of the passivated layer.

On the other hand, the capacitance of the passivated layer is a function of its dielectric constant and its thickness as shown in Equation (5-2).

$$C = \frac{A\varepsilon\varepsilon_0}{d} \tag{5-2}$$

Where, A is the effective electrode surface area, which is constant in our experiment. ε_0 is the vacuum permittivity (8.85×10^{-14} F/cm), ε and d are the dielectric constant and the thickness of the passivated layer, respectively. As a result, the impedance modules at low frequency is proportional to the thickness (d) and inversely proportional to the dielectric constant ε as shown in Equation (5-3).

$$Z'' = \left(\frac{1}{j\omega A\varepsilon_0}\right)\left(\frac{d}{\varepsilon}\right) = \alpha\ \left(\frac{d}{\varepsilon}\right) \quad (5\text{-}3)$$

The passivated layer on Al substrates in the presence of different inhibitors is very thin, the intensity of the ATR-FTIR absorption peak is considered as the representative of the thickness. Figure 5.4 shows the ATR-FTIR spectra of aluminum substrate immersed in 0.1 M NaCl for 24 h in the presence of Na_2SiO_3, $Na_2SiO_3/MnSO_4.H_2O$, Na_2SiO_3/NH_4VO_3, and $Na_2SiO_3/MnSO_4.H_2O/NH_4VO_3$ as inhibitors. The area under the peaks at the range of the wavenumber of 460-1280 cm^{-1} for all inhibitors was calculated using a peak fitting software. The sample with the presence of Na_2SiO_3 exhibited the lower peak area which could be due to its low thickness compared to the samples where the other inhibitors were used.

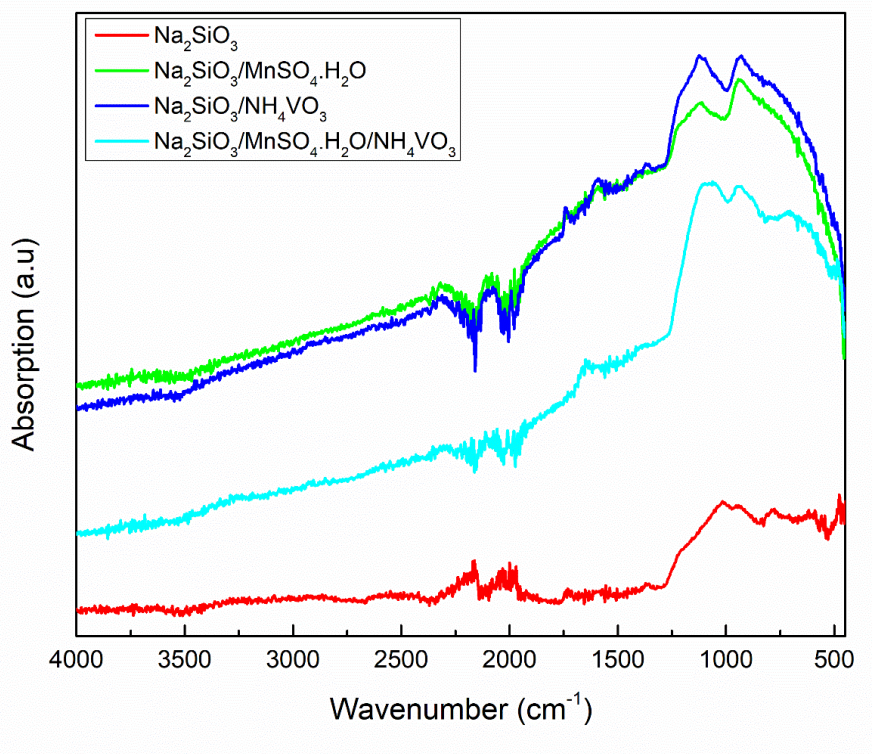

Figure 5.4: ATR-FTIR spectra of aluminum substrate immersed in 0.1 M NaCl for 24 h in the presence of Na_2SiO_3, $Na2SiO_3/MnSO_4.H_2O$, Na_2SiO_3/NH_4VO_3, and $Na_2SiO_3/MnSO_4.H_2O/NH_4VO_3$ as inhibitors.

The passivated layer on Al substrate is composed of oxides of Na_2SiO_3, MnO_2, and V_2O_5 inhibitors and their dielectric constants are 9, 72, and 36, respectively [34–36]. A graph of |Z| vs d/ε has been plotted and presented in Figure 5.5. The linear plot of |Z| vs d/ε supports the synergetic effect between the inhibitors. On the contrary, the Al substrate in presence of Na_2SiO_3 as inhibitor does not satisfy the linear correlation which could be due to the lower thickness of the protective layer on the Al substrate.

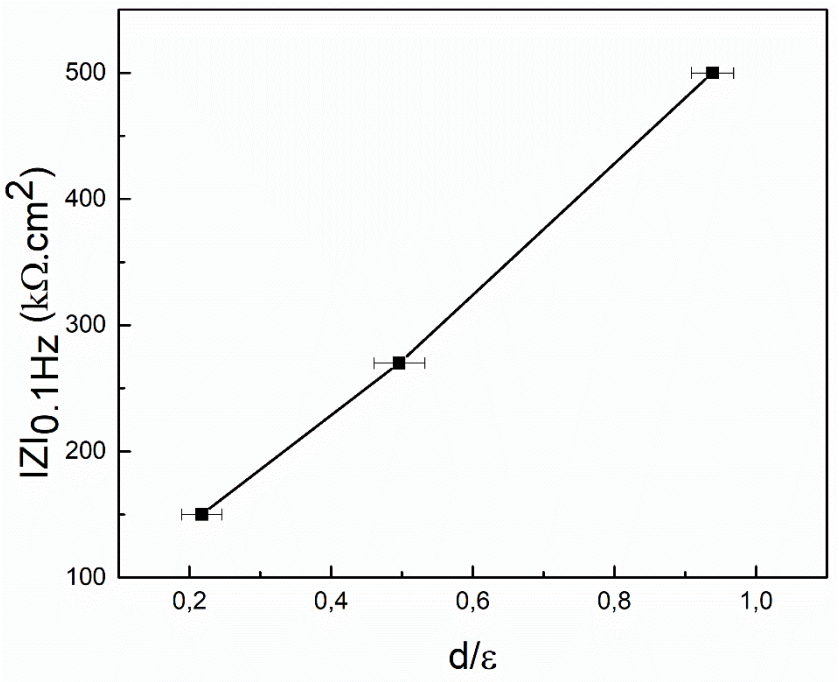

Figure 5.5: The impedance |Z| at the frequency of 0.1 Hz as a function of the peak area and dielectric constant of the probable adsorbed oxides on the Al substrate during the inhibition process.

Figure 5.2 (c) shows the Bode phase diagram of the Al substrate in the aqueous solution of 0.1 M NaCl and with the presence of Na_2SiO_3, $Na_2SiO_3/MnSO_4.H_2O$, Na_2SiO_3/NH_4VO_3, and $Na_2SiO_3/MnSO_4.H_2O/NH_4VO_3$ inhibitors. The full width at half maximum (FWHM) of the phase bands was calculated using analysis software and the results are summarized in Table 5.1.

Table 5.1: Full width half maximum (FWHM) values calculated from the fitting of Bode phase diagrams in Figure 2 (c).

Solution	FWHM (Hz)

NaCl	164
Na_2SiO_3	1905
Na_2SiO_3/ $MnSO_4.H_2O$	3019
Na_2SiO_3/ NH_4VO_3	26001
Na_2SiO_3/ $MnSO_4.H_2O$/ NH_4VO_3	27227

The FWHM value of 164 Hz was found for the Al substrate immersed in 0.1 M NaCl. Furthermore, FWHM values increased systemically to 1905, 3019, 26001 and 27227 Hz for the sample in the presence of Na_2SiO_3, Na_2SiO_3/$MnSO_4.H_2O$, Na_2SiO_3/NH_4VO_3 and Na_2SiO_3 /$MnSO_4.H_2O$ /NH_4VO_3 inhibitors, respectively. The increase of the FWHM values with the addition of the inhibitors could be related to the adsorption process of inhibitors on the Al substrate which leads to a change in the local dielectric constant [20]. On the other hand, the maximum phase angle was found to be shifting toward lower frequencies in the presence of the inhibitors (Na_2SiO_3, Na_2SiO_3/$MnSO_4.H_2O$, Na_2SiO_3/NH_4VO_3 and Na_2SiO_3 /$MnSO_4.H_2O$ /NH_4VO_3). This shift could be associated with the change of the local dielectric constant of the thin film, resulting from the probable deposition of Na_2SiO_3, VO_2, and MnO_2 with their respective dielectric constant of 9, 36, and 72 [34–36].

Figure 5.2 (d1) and (d2) are the electrical equivalent circuits (EEC) for the experimental impedance spectroscopy data of Al substrate immersed in 0.1 M NaCl and with the presence of Na_2SiO_3, Na_2SiO_3/$MnSO_4.H_2O$, Na_2SiO_3/NH_4VO_3, and Na_2SiO_3/$MnSO_4.H_2O$/NH_4VO_3 inhibitors respectively. Figure 5.2 (d1) shows the EEC of the Al substrate immersed in 0.1 M NaCl solution,

which is represented by an ohmic resistance R_S connected in series with RC circuit composed of capacitance C_1 and a charge transfer resistance R_{ct} in parallel. The circuit also contained a Warberg factor element (Z_w) that indicates the diffusion process of electrolyte/coating interface. In the case of the samples contain inhibitors, the constant phase element (CPE) is used to replace the ideal electrical capacitance in the circuits due to the heterogeneities in the microstructure and chemical composition [37]. Figure 5.2 (d2) represents the EEC associated with the samples contain inhibitors, where R_S is connected in series with two RC circuits. The CPE related to the dielectric properties of the samples is represented as CPE_f and the resistance provided by the inhibition film on the Al surface is presented as R_f. On the other hand, the CPE associated with the double layer at the interface near the Al surface is noted as (CPE_{dl}) and the charge transfer resistance is presented as R_{ct}. Table 5.2 and Table 5.3 summarized the impedance parameters of EEC for the Al substrate immersed in 0.1 M NaCl and with inhibitors, respectively.

Table 5.2: Fitted parameters of the equivalent circuit of EIS measurements of Al substrate immersed in 0.1 M NaCl for 24 h

Solution	Rs ($\Omega.cm^2$)	R_{ct}($k\Omega.cm^2$)	C_1($\mu F.cm^{-2}$)	n_f	Z_w($\Omega.cm^2.S^{1/2}$)
NaCl	79	6	5.95	0.47	7813

Table 5.3: Fitted parameters of the equivalent circuit of EIS measurements of Al substrate immersed in 0.1 M for 24 h in the presence of Na_2SiO_3, Na_2SiO_3/ $MnSO_4.H_2O$, Na_2SiO_3 /NH_4VO_3, and Na_2SiO_3 /$MnSO_4.H_2O$ /NH_4VO_3 inhibitors.

Solution	Rs ($\Omega.cm^2$)	CPE_f $Y_1(\Omega^{-1}.S^n.cm^{-2})$	n_f	R_f (Ω.cm2)	CPE_{dl} $Y_{dl}(\Omega^{-1}.S\text{-}^n.cm^{-2})$	n_{dl}	R_{ct} ($k\Omega.cm^2$)
Na_2SiO_3	86	3.26×10^{-11}	1.40	143	6.99×10^{-6}	0.90	47
Na_2SiO_3/ $MnSO_4.H_2O$	99	1.4×10^{-10}	1.29	183	4.38×10^{-6}	0.95	169
Na_2SiO_3/ NH_4VO_3	92	1.18×10^{-10}	1.31	171	4.02×10^{-6}	0.86	753
Na_2SiO_3/ $MnSO_4.H_2O$/ NH_4VO_3	90	2.67×10^{-6}	0.69	170	2.29×10^{-6}	0.88	926

It is observed in Table 5.3 that the CPE_{dl} of the Al substrate immersed in 0.1 M NaCl in the presence of Na_2SiO_3, Na_2SiO_3/ $MnSO_4.H_2O$, Na_2SiO_3/ NH_4VO_3, and Na_2SiO_3/$MnSO_4.H_2O$/ NH_4VO_3 are found to be 6.66×10^{-6}, 4.38×10^{-6}, 4.02×10^{-6}, and 2.29×10^{-6} $\Omega^{-1}.S^n$ cm^{-2}, respectively. This systematic decrease in the CPE_{dl} indicates that the hydrogen evolution reactions on the Al substrate are decelerated, suggesting a better inhibition performance when the mixture of the inhibitors is used in the solution [37].

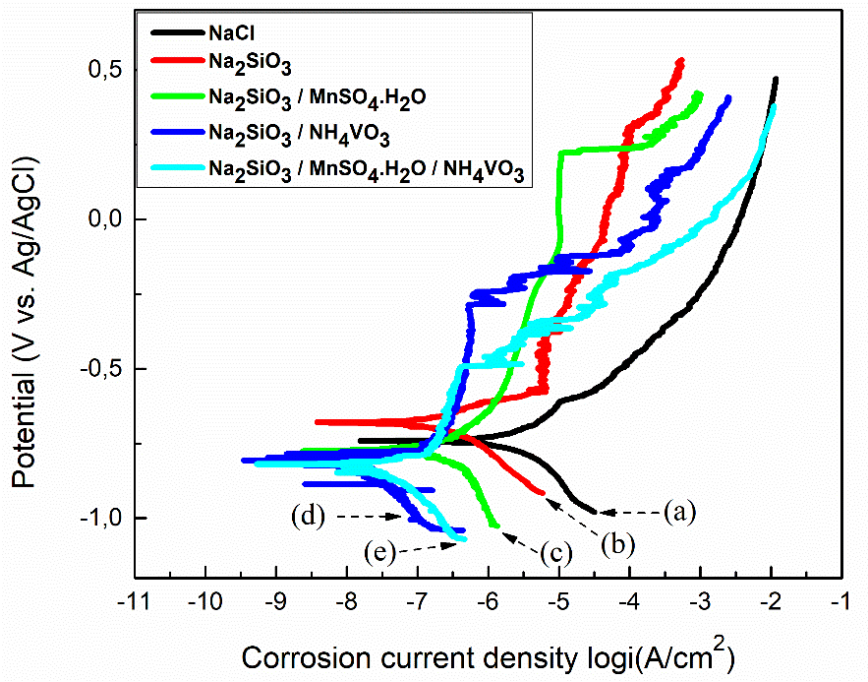

Figure 5.6: Potentiodynamic polarization curves of (a) Al substrate immersed in 0.1 M NaCl for 24 h without inhibitors, and with the presence of (b) Na_2SiO_3, (c) Na_2SiO_3/ $MnSO_4.H_2O$, (d) Na_2SiO_3 /NH_4VO_3, (e) and Na_2SiO_3 /$MnSO_4.H_2O$ /NH_4VO_3

Potentiodynamic polarization curves of Al substrate immersed in 0.1 M NaCl and with the presence of Na_2SiO_3, Na_2SiO_3/ $MnSO_4.H_2O$, Na_2SiO_3 /NH_4VO_3, and Na_2SiO_3 or/$MnSO_4.H_2O$ /NH_4VO_3 as inhibitors are shown in Figure 5.6.

The polarization resistance (R_p) is calculated from the Stern-Geary equation as given below:

$$R_p = \frac{\beta_a \beta_c}{2.3 I_{corr}(\beta_a + \beta_c)} \qquad (5\text{-}4)$$

where, β_a and β_c are the anodic and cathodic slopes of the Tafel curves, respectively. I_{corr} is the corrosion current density. The calculated values of I_{corr}, $R_{p,}$ and E_{corr} for all samples are presented in Table 5.4.

The Al substrate immersed in 0.1 M NaCl solution exhibited the highest I_{corr} value of 2 $\mu A/cm^2$ and the lowest R_p of 13 $k\Omega.cm^2$ as compared to all samples in the presence of inhibitors. For the sample containing Na_2SiO_3 as an inhibitor, I_{corr} value decreases to 0.25 $\mu A/cm^2$ and R_p value increases to 100 $k\Omega.cm^2$. This happens due to the formation of a protective layer of aluminosilicate on Al substrate. This result corroborates with the result obtained from EIS studies.

Table 5.4: Open circuit potential (OCP), corrosion potential (E_{corr}), corrosion current density (I_{corr}), polarization resistance (R_p), anodic Tafel coefficient (β_a) and cathodic Tafel coefficient (β_c) of Al substrate immersed in 0.1 M NaCl without inhibitors, and with the presence of Na_2SiO_3, Na_2SiO_3/ $MnSO_4.H_2O$, Na_2SiO_3 /NH_4VO_3, and Na_2SiO_3 /$MnSO_4.H_2O$ /NH_4VO_3.

	OCP (mV) Vs. Ag/AgCl	Corrosion potential E_{corr} (mV) Vs. Ag/AgCl	Corrosion current density I_{corr} ($\mu A/cm^2$)	Polarization resistance R_p ($k\Omega.cm^2$)	Corrosion inhibition efficiency η (%)
NaCl	-734	-741	2	13	-
Na_2SiO_3	-678	-680	0.25	100	87.5
Na_2SiO_3/ $MnSO_4.H_2O$	-798	-775	0.16	133	92
Na_2SiO_3/ NH_4VO_3	-861	-843	0.003	679	99.5
Na_2SiO_3/ $MnSO_4.H_2O$/ NH_4VO_3	-838	-816	0.002	722	99.99

Garrity *et al.* [13] have investigated the corrosion protection of Al by adding different concentrations of Na_2SiO_3 as an inhibitor into a 0.1 M NaCl aqueous solution. In their work, the potentiodynamic polarization curves show that sodium silicate provided strong anodic inhibition. The sample contains Na_2SiO_3/ $MnSO_4.H_2O$ as inhibitor displayed a further decrease of I_{corr} value to 0.16 $\mu A/cm^2$ and increase of R_p to 133 $k\Omega.cm^2$. It has been reported elsewhere that Mn-based inhibitors can reduce the corrosion of Al alloys at high pH values (pH>11), which could be due to

the reduction of Mn(VII) in alkaline environments and the formation of a protective layer of MnO_2, a less soluble species, on the Al substrate [16,17]. The I_{corr} value has further decreased to 0.003 μA/cm^2 and R_p has further increased to 679 kΩ.cm^2 for the sample contained Na_2SiO_3/ NH_4VO_3 as an inhibitor. In a similar study, Ralston *et al*. [19] had investigated the corrosion inhibition of Al by sodium metavanadate (NaVO3) at different pH environments. They observed that the addition of $NaVO_3$ has no effect at pH of 3 and 5. However, it leads to a noticeable decrease in corrosion potential and corrosion current density at a pH of 8 and 10. Their pH values are comparable to the measured pH value of 11 for the sample contained Na_2SiO_3/ NH_4VO_3 as an inhibitor in this work, which explains the better corrosion inhibition properties of Na_2SiO_3/ NH_4VO_3.

The lowest I_{corr} value of 0.002 μA/cm^{2}and the highest R_p of 722 kΩ.cm^2 is observed for the sample in the presence of mixed Na_2SiO_3 /$MnSO_4.H_2O$ /NH_4VO_3 as an inhibitor. The improved corrosion protection properties indicate that the inhibitors appear to display a synergetic effect.

Figure 5.7 (a,b) shows bar chart comparison of the polarization resistance R_p and the corrosion current density I_{corr} of the Al substrate immersed in 0.1 M NaCl solution and with the presence of Na_2SiO_3, Na_2SiO_3/ $MnSO_4.H_2O$, Na_2SiO_3/ NH_4VO_3, and Na_2SiO_3 /$MnSO_4.H_2O$ /NH_4VO_3 as inhibitors. A significant rise of R_p value is observed (Figure 5.7 (a)) for the sample contained Na_2SiO_3 /NH_4VO_3 as an inhibitor. A systematic decrease of I_{corr} values is observed (Figure 5.7 (b)) for samples in the presence of inhibitors. The sample contains mixed Na_2SiO_3 /$MnSO_4.H_2O$ /NH_4VO_3 as inhibitor provided the best corrosion protection for Al substrate.

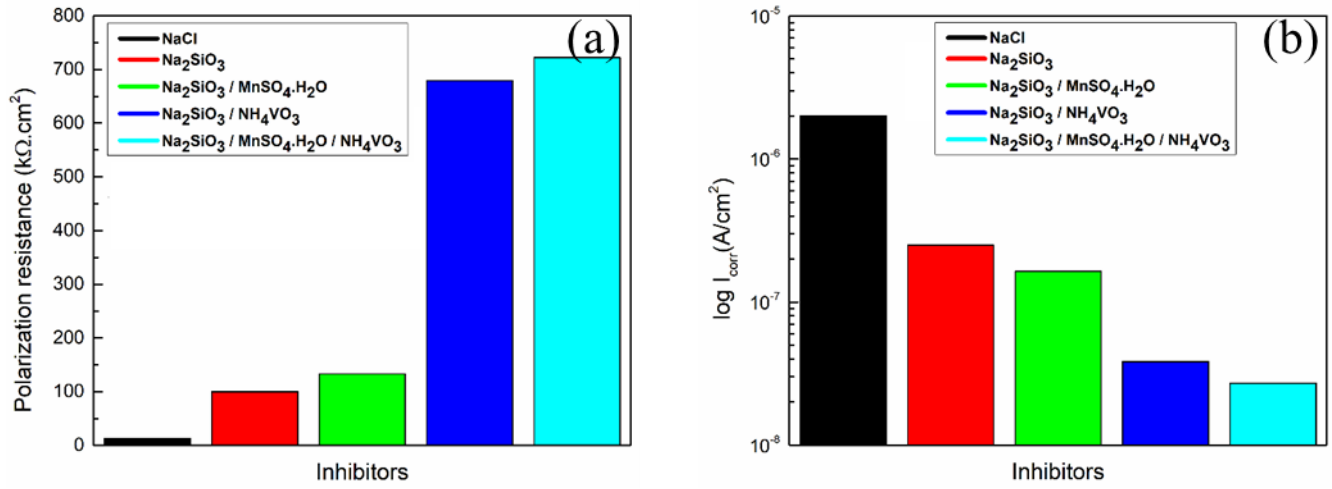

Figure 5.7: The variation of the (a) Polarization resistance R_p and the (b) corrosion current density I_{corr} of Al substrate immersed in 0.1 M NaCl without inhibitors, and with the presence of Na_2SiO_3, Na_2SiO_3/ $MnSO_4.H_2O$, Na_2SiO_3 /NH_4VO_3, and Na_2SiO_3 /$MnSO_4.H_2O$ /NH_4VO_3.

The corrosion inhibition efficiency η (%) of all the samples was evaluated using the standard equation below:

$$\eta(\%) = \frac{I_{corr(0)} - I_{corr(\text{inh})}}{I_{corr(0)}} \times 100 \qquad (5\text{-}5)$$

Where $I_{corr(0)}$ is the corrosion current density of Al substrate immersed in 0.1 M NaCl and $I_{corr(inh)}$ is the corrosion current density of the Al substrate in the presence of inhibitors. A systematic increase of η values of 87.5, 92, 99.5, and 99.9 % are found for the samples in presence of Na_2SiO_3, Na_2SiO_3/ $MnSO_4.H_2O$, Na_2SiO_3/ NH_4VO_3, and Na_2SiO_3 /$MnSO_4.H_2O$ /NH_4VO_3, respectively. The highest corrosion inhibition efficiency observed of mixed Na_2SiO_3 /$MnSO_4.H_2O$ /NH_4VO_3 sample

could be due to the formation of a complex inhibitor structure, which could adsorb on the metallic substrate and prevents the penetration of corrosive ions to the substrate.

To understand synergetic effects for the mixed Na_2SiO_3 /$MnSO_4.H_2O$ /NH_4VO_3 sample, which can be taken place between Na_2SiO_3, $MnSO_4.H_2O$, and NH_4VO_3 inhibitors, the synergism parameter, s, is determined as proposed by Aramaki *et al.* in 1969 [38]. Generally, for the interaction of inhibitors A and B, the synergism parameter, s, is given by the Equation (5-6):

$$s = \frac{1 - (\eta_{A+}\eta_B)}{1 - \eta_{AB}} \tag{5-6}$$

where η_A and η_B are the corrosion inhibition efficiencies calculated for inhibitor A and B, respectively, while η_{AB} is the corrosion inhibition efficiency for the mixture of A and B.

When the inhibitor A or B have no effect on each other and adsorbs independently at the metal/solution interface, then the value of s will be 1. On the other hand, s > 1 represents a manifestation of synergetic effects, while antagonistic effects are characterized when s <1.

In this work, the synergism parameter, s, for the mixed Na_2SiO_3 /$MnSO_4.H_2O$ /NH_4VO_3 was found to be 2.8. This value confirms that the enhanced inhibition efficiency for the mixed inhibitor sample is achieved due to the synergetic effect.

Figure 5.8 (a) represents the SEM image of the as-received Al substrate and the lines appearing on the substrate surface are due to the rolling process. The SEM image of the Al substrate immersed in a 0.1 M NaCl aqueous solution for 24 h is shown in Figure 5.8 (b). The image exhibits corrosion-related features corresponding to the intermetallic phases. The potential

difference between these intermetallic phases and the Al matrix causes the formation of galvanic corrosion cells and leads to localized corrosion of the Al matrix [1].

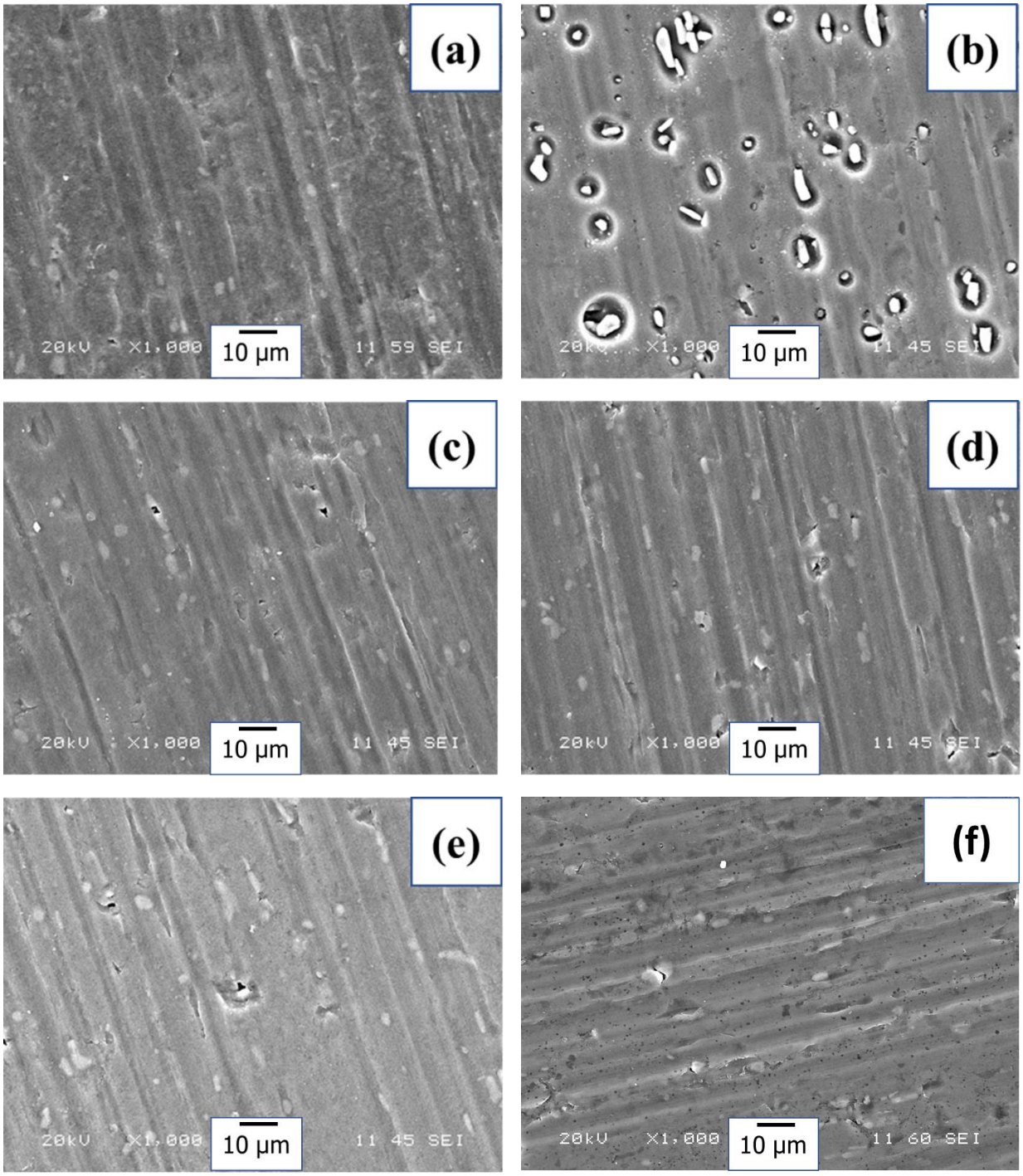

Figure 5.8: SEM images of (a) as-received Al substrate. (b) Al substrate immersed in 0.1 M NaCl for 24 h, and with the presence of the inhibitors of (c) Na_2SiO_3, (d) Na_2SiO_3/ $MnSO_4.H_2O$, (e) Na_2SiO_3 /NH_4VO_3, (f) and Na_2SiO_3 /$MnSO_4.H_2O$ /NH_4VO_3.

It is observed from the images that the shape of the corroded area on the Al surface either circular or elliptical. This shape seems to be determined by the shape of the intermetallic phases. Additionally, the image can be used to determine the percentage of the corroded area on the Al surface using image analysis software and the value was found to be 5.7%. Interestingly, in the image shown in Figure 5.8 (c), no such corrosion features are visible for the sample with the presence of Na_2SiO_3 as an inhibitor. The percentage of the corroded area is found to be 0.29 %. This decrease in the percentage of the corroded area could be to the formation of sodium silicate protective layer on the Al substrate and that prevents the penetration of corrosive ions to the substrate [13]. A similar image is shown in Figure 5.8 (d) for the sample contained Na_2SiO_3/ $MnSO_4.H_2O$ as an inhibitor, and the calculated percentage of corrosion is 0.08 %. The decrease of the percentage of the corroded area with the addition of Mn-based inhibition could be due to its inhibitive properties in alkaline environments. In a similar study, Mikhailovskii *et al.* [16] reported that manganese ions (MnO_4^-) inhibits the corrosion of Al alloys at high pH values, which is due to the fact that the reduction of Mn(VII) in alkaline media leads to the formation of MnO_2, considered as a less soluble species. A further decrease of the percentage of the corroded area (0.06 %) was calculated for the sample with the presence of Na_2SiO_3 /NH_4VO_3 as an inhibitor, and the image is illustrated in Figure 5.8 (e). Ralston *et al.* [19] studied the corrosion inhibition of Al by aqueous vanadium species. They found that in alkaline solutions vanadates play a role in preventing the dissolution of magnesium from the intermetallic particles. As a result, these particles may not become strong cathodes, which reduces the effect of localized corrosion. Figure 5.8 (f) shows the SEM image of the sample contained Na_2SiO_3 /$MnSO_4.H_2O$ /NH_4VO_3 as an inhibitor. The calculated percentage of the corroded area was found to be 0.06 %. This result indicates an excellent corrosion protection performance for the mixed inhibitors solution due to the formation

of a complex inhibitors structure that adsorbs on the Al surface to protect against corrosion. The calculated values of the percentage corroded area of all samples are presented in Figure 5.9.

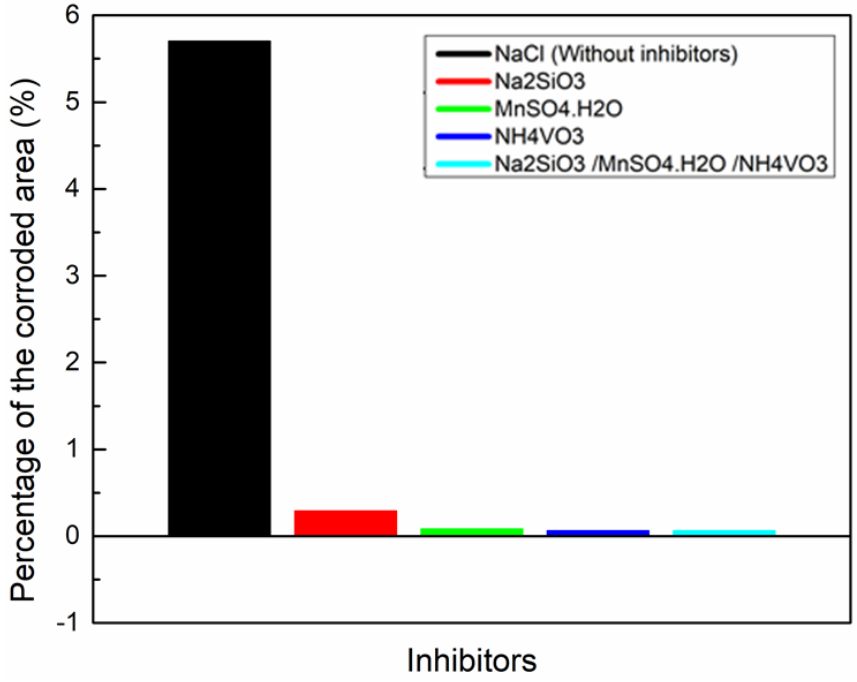

Figure 5.9: The percentage of the corroded area determined from SEM images of Al substrate immersed in 0.1 M NaCl for 24 h, and with the presence of the inhibitors of Na_2SiO_3, Na_2SiO_3/ $MnSO_4.H_2O$, Na_2SiO_3 /NH_4VO_3, and Na_2SiO_3 /$MnSO_4.H_2O$ /NH_4VO_3.

In Figure 5.10 (a), the EDS spectra of as-received Al substrate is characterized by the presence of the elements of O and Al with their respective Kα peaks at 0.52 and 1.48 keV. Figure 5.10 (b) shows the spectrum of Al substrate immersed for 24 h in 0.1 M NaCl solution. The spectrum shows the presence of C, O, Al and Cl with their respective Kα peaks at 0.28, 0.52,1.48, and 2.62 keV. The Lα peaks of Mn and Fe are located at 0.63 and 0.70 keV, respectively. While the Mα peaks of Mn and Fe are located at 5.89 and 6.39 KeV, respectively. The presence of Mn and Fe elements

in the surface chemical composition indicates the effect of the localized corrosion process caused by the potential difference between the intermetallic phases and the Al matrix. Figure 5.10 (c) shows the spectrum of Al substrate immersed for 24 h in 0.1 M NaCl solution in the presence of Na_2SiO_3 as an inhibitor. The spectrum is composed of C, O, Na, and Si elements with their respective Kα peaks at 0.27, 0.52, 1.04, and 1.73 keV. The presence Na and Si peaks could be related to the formation of an inhibitive layer of sodium silicate on the Al substrate. Figure 5.10 (d) shows the spectrum of the sample in the presence of Na_2SiO_3/ $MnSO_4.H_2O$ as an inhibitor. The spectrum is composed of C, O and Mn elements with their respective Kα peaks at 0.27, 0.52, and 5.89 keV. The Mn-related peak at 0.63 keV due to Lα could be due to the intermetallic phases or the deposition of Mn on the Al surface. Figure 5.10 (e) shows the spectrum of the sample in the presence of Na_2SiO_3 /NH_4VO_3 as an inhibitor. The spectrum is composed of C, O and V elements with their respective Kα peaks at 0.27, 0.52, and 4.94 keV. The vanadium Lα peak at 0.51 keV could be due to the deposition of vanadium on the Al surface. The spectrum in Figure 5.10 (f) corresponds to the sample in the presence of Na_2SiO_3 /$MnSO_4.H_2O$ /NH_4VO_3. The spectrum is composed of C, O, V, and Mn elements with their respective Kα X-ray peaks at 0.2, 0.5, 4.9 and 5.8 keV. The appearance of V and Mn peak in the EDS spectrum could be related to the formation of a complex inhibitors structure layer on the Al substrate. It is to mention that in certain cases, the gold conductive coating was applied on samples for better imaging and analysis, which resulted in the appearance of the peak at around 2.12 keV.

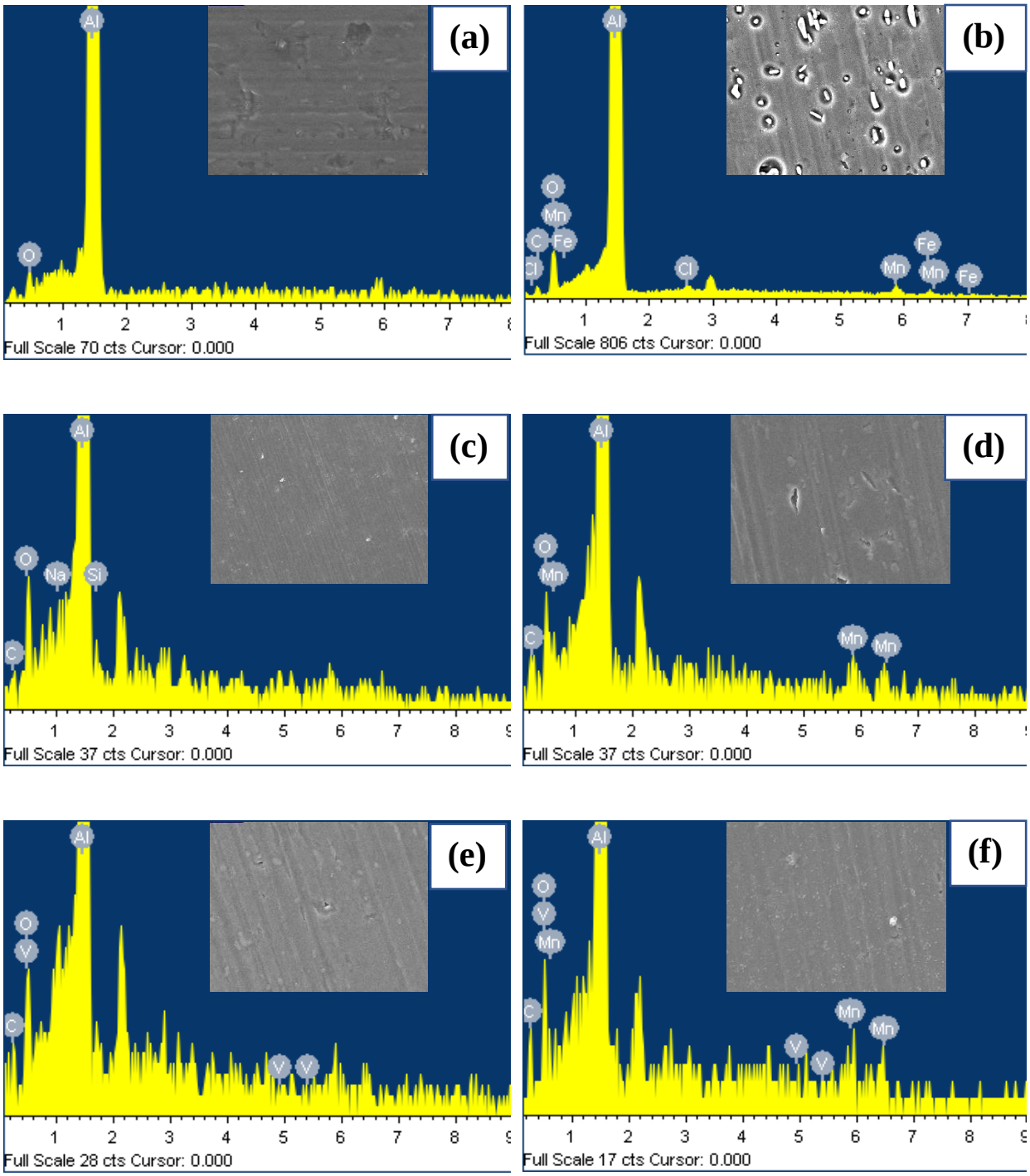

Figure 5.10: EDS spectra of (a) as-received Al substrate, (b) Al substrate immersed in 0.1 M NaCl for 24 h, and with the presence of the inhibitors of (c) Na_2SiO_3, (d) Na_2SiO_3/ $MnSO_4.H_2O$, (e) Na_2SiO_3 /NH_4VO_3, and (f) Na_2SiO_3 /$MnSO_4.H_2O$ /NH_4VO_3 inhibitors.

5.4 **Conclusion**

A comparative study on the corrosion inhibition performance of Na_2SiO_3, $Na_2SiO_3/MnSO_4.H_2O$, and Na_2SiO_3/NH_4VO_3 for laminated AA6061-T6 aluminum alloy was undertaken. It was found that the mixture of three inhibitors provided the best performance against corrosion in NaCl environments. The inhibition efficiency (η) of the inhibitors was calculated from the corrosion current density, which was found to be 87.5, 92, and 99.5 % for Na_2SiO_3, $Na_2SiO_3/MnSO_4.H_2O$, and Na_2SiO_3/NH_4VO_3, respectively. However, a maximum value of η 99.9 % was obtained in the mixed inhibitors of Na_2SiO_3 $/MnSO_4.H_2O$ $/NH_4VO_3$ due to synergic effect. The corrosion inhibitors used in this study displays promising results in terms of replacement of chromate-based inhibitors.

References

[1] J.Y. Cao, M. Wang, L. Kong, L.J. Guo, Hook formation and mechanical properties of friction spot welding in alloy 6061-T6, J. Mater. Process. Technol. 230 (2016) 254–262.

[2] S.A. Abdel-Gawad, M.A. Sadik, M.A. Shoeib, Preparation and properties of a novel nano Ni-B-Sn by electroless deposition on 7075-T6 aluminum alloy for aerospace application, J. Alloys Compd. (2019).

[3] T. Maeno, K. Mori, R. Yachi, Hot stamping of high-strength aluminium alloy aircraft parts using quick heating, CIRP Ann. 66 (2017) 269–272.

[4] W.. Miller, L. Zhuang, J. Bottema, A.. Wittebrood, P. De Smet, A. Haszler, A. Vieregge, Recent development in aluminium alloys for the automotive industry, Mater. Sci. Eng. A. 280 (2000) 37–49.

[5] Y. Fu, X. Chen, B. Zhang, Y. Gong, H. Zhang, H. Li, Fabrication of nanodiamond reinforced aluminum composite coatings by flame spraying for marine applications, Mater. Today Commun. 17 (2018) 46–52.

[6] J.K. Oh, S. Liu, M. Jones, Y. Yegin, L. Hao, T.N. Tolen, N. Nagabandi, E.A. Scholar, A. Castillo, T.M. Taylor, L. Cisneros-Zevallos, M. Akbulut, Modification of aluminum surfaces with superhydrophobic nanotextures for enhanced food safety and hygiene, Food Control. 96 (2019) 463–469.

[7] Y. Liu, H. Liu, Z. Chen, Post-fire mechanical properties of aluminum alloy 6082-T6, Constr. Build. Mater. 196 (2019) 256–266.

[8] A. Salam Hamdy, A.M. Beccaria, T. Temtchenko, Corrosion protection of AA6061 T6 by

fluoropolymer coatings in NaCl solution, Surf. Coatings Technol. 155 (2002) 176–183.

[9] J. Zhao, L. Xia, A. Sehgal, D. Lu, R.L. McCreery, G.S. Frankel, Effects of chromate and chromate conversion coatings on corrosion of aluminum alloy 2024-T3, Surf. Coatings Technol. 140 (2001) 51–57.

[10] W.J. Clark, J.D. Ramsey, R.L. McCreery, G.S. Frankel, A Galvanic Corrosion Approach to Investigating Chromate Effects on Aluminum Alloy 2024-T3, J. Electrochem. Soc. 149 (2002) B179.

[11] C. Pellerin, S.M. Booker, Reflections on hexavalent chromium: Health hazards of an industrial heavyweight, Environ. Health Perspect. 108 (2000) 402–407.

[12] X. Yang, P. Roonasi, A. Holmgren, A study of sodium silicate in aqueous solution and sorbed by synthetic magnetite using in situ ATR-FTIR spectroscopy, J. Colloid Interface Sci. 328 (2008) 41–47.

[13] O. Lopez-Garrity, G.S. Frankel, Corrosion inhibition of AA2024-t3 by sodium silicate, Electrochim. Acta. 130 (2014) 9–21.

[14] J.W. Wood, J.S. Beecher, P.S. Laurence, Some Experiences With Sodium Silicate As a Corrosion Inhibitor in Industrial Cooling Waters, Corrosion. 13 (1957) 41–46.

[15] H. Gao, Q. Li, F. Chen, Y. Dai, F. Luo, L. Li, Study of the corrosion inhibition effect of sodium silicate on AZ91D magnesium alloy, Corros. Sci. 53 (2011) 1401–1407.

[16] Y. Mikhalovekii, Influence of pH on electrochemical and corrosion behavior of aluminum in media containing oxo anions of the oxidizing type, Zashchita Met. 21 (1985) 935–939.

[17] S.A. Kulinich, M. Farzaneh, X.W. Du, Growth of corrosion-resistant manganese oxide

coatings on an aluminum alloy, Inorg. Mater. 43 (2007) 956–963.

[18] S.A. Kanimozhi, S. Rajendran, Aluminium Inhibition By Potassium Permanganate – Zn 2 + System, Arab. J. Sci. Eng. 35 (2009) 41–52.

[19] K.D. Ralston, S. Chrisanti, T.L. Young, R.G. Buchheit, Corrosion Inhibition of Aluminum Alloy 2024-T3 by Aqueous Vanadium Species, J. Electrochem. Soc. 155 (2008) 350–359.

[20] D.S. Kharitonov, J. Sommertune, C. Örnek, J. Ryl, I.I. Kurilo, P.M. Claesson, J. Pan, Corrosion Inhibition of Aluminium Alloy AA6063-T5 by Vanadates: Local Surface Chemical Events Elucidated by Confocal Raman Micro-Spectroscopy, Corros. Sci. (2018).

[21] M.F. Morks, P.A. Corrigan, I.S. Cole, Mnâ€“Mg based zinc phosphate and vanadate for corrosion inhibition of steel pipelines transport of CO2 rich fluids, Int. J. Greenh. Gas Control. 7 (2011) 218–224.

[22] S. Bonetti, R. Spengler, A. Petersen, L.S. Aleixo, A.A. Merlo, S.M. Tamborim, Surface-decorated silica with Schiff base as an anticorrosive coating for aluminium alloy 2024-T3, Appl. Surf. Sci. 475 (2019) 684–694.

[23] M.K. Cavanaugh, J.-C. Li, N. Birbilis, R.G. Buchheit, Electrochemical Characterization of Intermetallic Phases Common to Aluminum Alloys as a Function of Solution Temperature, J. Electrochem. Soc. 161 (2014) C535–C543.

[24] N. Asrar, A.U. Malik, S. Ahmed, Corrosion Prevention With Sodium Silicate 1, N.D.

[25] F.B. Mainier, A.A.M. Figueiredo, A.E.R. De Freitas, A.M. De Alencar Junior, The Use of Sodium Silicate as a Corrosion Inhibitor in a Saline Drilling Fluid: A Nonaggressive

Option to the Environment, J. Environ. Prot. (Irvine,. Calif). 7 (2000) 2025–2035.

[26] C.G. Dariva, A.F. Galio, Corrosion Inhibitors-Principles, Mechanisms and Applications, in: Chapter Corros. Inhib., 2014.

[27] S.B. Madden, J.R. Scully, Inhibition of AA2024-T351 Corrosion Using Permanganate, J. Electrochem. Soc. 161 (2014) 162–175.

[28] K.D. Ralston, T.L. Young, R.G. Buchheit, Electrochemical Evaluation of Constituent Intermetallics in Aluminum Alloy 2024-T3 Exposed to Aqueous Vanadate Inhibitors, J. Electrochem. Soc. 156 (2009) 135–146.

[29] Z. Wang, J. Li, Y. Wang, Z. Wang, An EIS analysis on corrosion resistance of anti-abrasion coating, Surfaces and Interfaces. 6 (2017) 33–39.

[30] A.S. Hamdy, Corrosion protection of aluminum composites by silicate/cerate conversion coating, Surf. Coatings Technol. 200 (2006) 3786–3792.

[31] M. Mohammadi, A. Yazdani, F. Mohammadi, A. Alfantazi, Corrosion Behavior of 2024 Aluminum Alloy Anodized in Sulfuric Acid, (2013) 509–513.

[32] R.L. Twite, G.P. Bierwagen, Review of alternatives to chromate for corrosion protection of aluminum aerospace alloys, Prog. Org. Coatings. 33 (1998) 91–100.

[33] P.J. Denissen, S.J. Garcia, Reducing subjectivity in EIS interpretation of corrosion and corrosion inhibition processes by in-situ optical analysis, Electrochim. Acta. 293 (2019) 514–524.

[34] S. Jumrat, B. Chatveera, P. Rattanadecho, Dielectric properties and temperature profile of fly ash-based geopolymer mortar ☆, Int. Commun. Heat Mass Transf. 38 (2011) 242–248.

[35] Z. Yang, C. Ko, V. Balakrishnan, G. Gopalakrishnan, S. Ramanathan, Dielectric and carrier transport properties of vanadium dioxide thin films across the phase transition utilizing gated capacitor devices, Phys. Rev. B. 82 (2010) 205101.

[36] M. Moalleminejad, D.D.L. Chung, Dielectric constant and electrical conductivity of carbon black as an electrically conductive additive in a manganese-dioxide electrochemical electrode, and their dependence on electrolyte permeation, (2015).

[37] B. Hirschorn, M.E. Orazem, B. Tribollet, V. Vivier, I. Frateur, M. Musiani, Determination of effective capacitance and film thickness from constant-phase-element parameters, Electrochim. Acta. 55 (2009) 6218–6227.

[38] K. Aramaki, N. Hackerman, Inhibition Mechanism of Medium-Sized Polymethyleneimine, J. Electrochem. Soc. Electrochem. Sci. 116 (1969) 568–574.

CHAPTER 6

ZIRCONIUM SILICATE THIN FILMS BY SOL-GEL PROCESS FOR CORROSION PROTECTION OF ALUMINUM

CHAPTER 6 : ZIRCONIUM SILICATE THIN FILMS BY SOL-GEL PROCESS FOR CORROSION PROTECTION OF ALUMINUM

Abstract

The fabrication of zirconium silicate thin films by sol-gel process on laminated AA6061-T6 aluminum alloy (Al) has been exanimated. The thin films were prepared by the combination of two precursors, zirconium (IV) n-propoxide and tetraethylorthosilicate (TEOS). The effect of the aging time and the concentration of the sol on the corrosion properties of the fabricated thin films were evaluated. The morphology of the thin films was analyzed using scanning electron microscopy (SEM), the chemical composition was studied using Attenuated Total Reflectance-Fourier transform infrared spectroscopy (ATR-FTIR) and energy dispersive X-ray spectroscopy (EDS). The barrier properties of the fabricated thin films were analyzed using potentiodynamic polarization studies. The zirconium silicate thin films fabricated from the Si/Zr molar ratio of 0.5 and the aging time of the sol of 72 h exhibited a polarization resistance R_p of 446 kΩ.cm^2 compared to 10 kΩ.cm^2 for as-received aluminum substrate, which indicates the good corrosion properties of these thin films.

6.1 **Introduction**

Aluminum alloys have attracted high interest in many applications due to their high strength, low cost and high performance, these materials are used in aerospace, automobile, aircraft, boats and electronic industries [1,2]. Despite their good properties, aluminum alloys show weak resistance to corrosion in marine environments resulting from the penetration of chloride ions to the protective oxide film formed on the aluminum surface (alumina) [3,4].

In that regard, various coating systems are employed to protect aluminum against corrosion such as chromate-based coatings which have been used for decades [5,6]. However, these coatings deliver residual hexavalent chromate ions, a toxic compound to human health and environment [7,8]. Given the need for replacement of these chromate-based coatings, environmentally-friendly, effective, and inexpensive coatings with simple fabrication processes have been attracted a lot of attention for corrosion protection of aluminum. Sol-gel derived thin films are considered as chromate-free compounds and could be good candidates for environmentally friendly corrosion treatments. The sol-gel process is an efficient process that offers several advantages such as low-temperature densification, good adhesion on the metallic substrates, cost effectiveness and with simple application procedures, which are easily adaptable in the industrial applications [13]. A considerable amount of sol-gel studies is based on silicon precursors due to their balance of reactivity and ease of handling. It is well known that the corrosion resistance of the sol-gel coatings is attributed to its physical barrier properties, which prevents the penetration of the corrosion ions to the metallic substrate. However, silica-based coatings could present pores and crack on the surface, which could reduce their corrosion protection efficiency [14]. In order to limit the corrosion process caused by pores and cracks formation, hybrid silicate-based coatings containing organic compounds and/or metal oxides have been extensively investigated [15–17].

Zirconium is an effective material for the corrosion protection of Al. The zirconium-based materials have attracted great interest due to their good mechanical strength, thermal stability as well as the strong alkali and acid resistant property compared to other ceramic materials [10]. As far as corrosion studies on the Zr-based thin films are concern, typically, they are hydrophilic in nature and applied either on steel or aluminum. Li *et al.* [11] reported the use of Zr-based thin films for the corrosion protection of mild steel. In their work, they have deposited Zr-based hydrophilic thin films on flat sheets of mild steel by dip-coating process. They have reported that the polarization resistance of the Zr-based thin films was 299 $\Omega.cm^2$ as compared to 40 $\Omega.cm^2$ for as-received steel substrates. The corrosion properties of the Zr-based conversion thin films on aluminum substrates was also reported by Li *et al.* They have reported the polarization resistance of the Zr-based thin films on aluminum to be 47 $k\Omega.cm^2$ as compared to 13 $k\Omega.cm^2$ for the as-received aluminum substrate [12].

In this study, zirconium silicate thin films were fabricated on the aluminum substrates using sol-gel process. Zirconium (IV) n-propoxide was used with TEOS as precursors to prepare thin films with different sol aging times. The morphology, the chemical composition, and the corrosion properties of the thin films were investigated.

6.2 Experimental

6.2.1 Material and specimen preparation

The laminated AA6061-T6 aluminum alloy with the chemical composition of Al 97.9 wt.%, Mg 1.08 wt.%, Si 0.63 wt.%, Mn 0.52 wt.%, Cu 0.32 wt.%, Fe 0.17 wt.%, Ti 0.02 wt.%, and V 0.01 wt.%, was used as substrates for this study. The Al substrates with the size of one by

one inch and without any surface finishing were ultrasonically degreased in a soap solution and cleaned in ethanol and deionized water for 30 min each. Further, the cleaned substrates were dried in air at 70 ˚C.

6.2.2 Preparation of sol-gel thin films

Zirconium silicate thin films were prepared by a sol-gel process on Al. Concurrently, two separate sols, silicon (Si)-based sol, and zirconium (Zr)-based sol were formulated. The Si-based sol was prepared by mixing 10 mL of tetraethylorthosilicate (TEOS) with 10 mL of ethanol, then nitric acid (HNO_3) was dropwise added while continuously stirring the solution. The solution was stirred for 2 h in a sealed beaker at 70˚C. On the other hand, to prepare the Zr-based sol, zirconium (IV)-n-propoxide was used as a precursor. The volume of 2 mL of the Zr precursor was diluted with 10 ml of propanol with continuous stirring for 5 minutes. Thereafter, 0.5 mL of the Si-based sol was gently added into Zr-based sol with stirring. The mixed solution was kept aging at room temperature, and after specific aging times of 1, 24, 48, and 72 h, the solution was deposited on laminated AA6061-T6 aluminum alloy substrates by spin coating and kept drying at 300˚C for 2 h. The preparation procedure has been summarized in Figure 6.1.

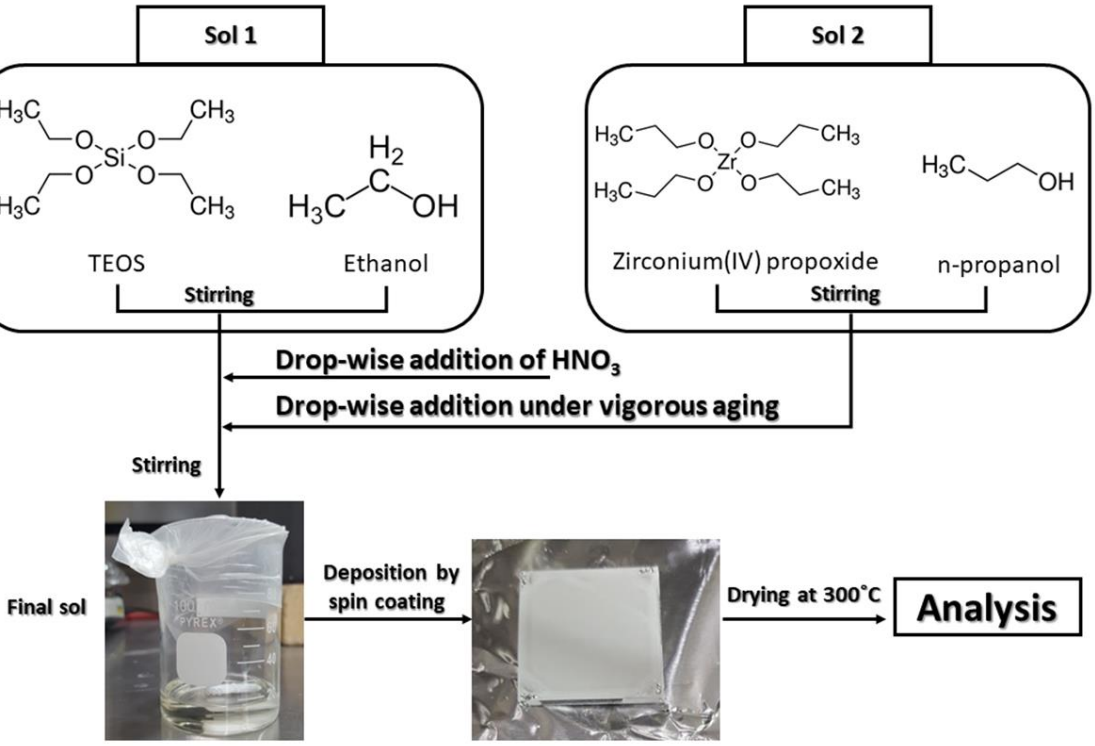

Figure 6.1: Experimental procedure for the preparation of zirconium silicate sol from two separate prepared sols.

6.2.3 Characterization of sol-gel thin films on AA6061

The morphology of the fabricated thin films was observed using scanning electron microscopy (SEM, JEO JSM-6480 LV). The energy dispersive X-ray spectroscopy (EDS) and Attenuated Total Reflectance-Fourier transform infrared (ATR-FTIR, Agilent Technologies Cary 630) spectroscopy was used to analyze the chemical composition of the thin films.

A three electrodes set-up, consisting of a platinum mesh (counter electrode), a silver/silver-chloride (Ag-AgCl) (reference electrode), and the fabricated samples (working electrodes) was employed. The potentiodynamic polarization curves were scanned in a range of -250 mV to 1000

mV with respect to OCP using a scan rate of 2 mV/s. The frequency range of the electrochemical impedance spectroscopy (EIS) study was fixed between 10^{-2} and 10^{5} Hz with an amplitude of 20 mV with respect to the open circuit potential (OCP). All the electrochemical experiments were carried out in 3.5 wt.% NaCl solution with a pH of 5.8 to simulate seawater.

6.3 **Results and discussion**

Figure 6.1 shows the SEM images of the as-received Al and the zirconium silicate thin films fabricated from the Si/Zr molar ratio of 0.5 after the aging time of the sol of 24, 48, and 72 h. Figure 6.1 (a) shows the SEM image of the as-received Al substrate, which exhibits parallel lines due to the rolling process. Furthermore, Figure 6.1 (b) shows the zirconium silicate thin film fabricated after the aging time of the sol of 24 h. The zirconium silicate grains have micro-island shapes with uniform coverage area on the Al substrate. Afterward, Figure 6.1 (c) shows the morphology of the zirconium silicate thin film after the aging time of the sol of 48 h. It can be seen that the coverage area of the zirconium silicate grains increases. Figure 6.1 (d) shows the morphology of the zirconium silicate thin film after the aging time of the sol of 72 h, which has a similar morphology of the zirconium silicate thin film fabricated after the aging time of the sol of 48 h. However, the large time of aging could lead to the formation of dense thin films due to the increase of the viscosity of the sol with time.

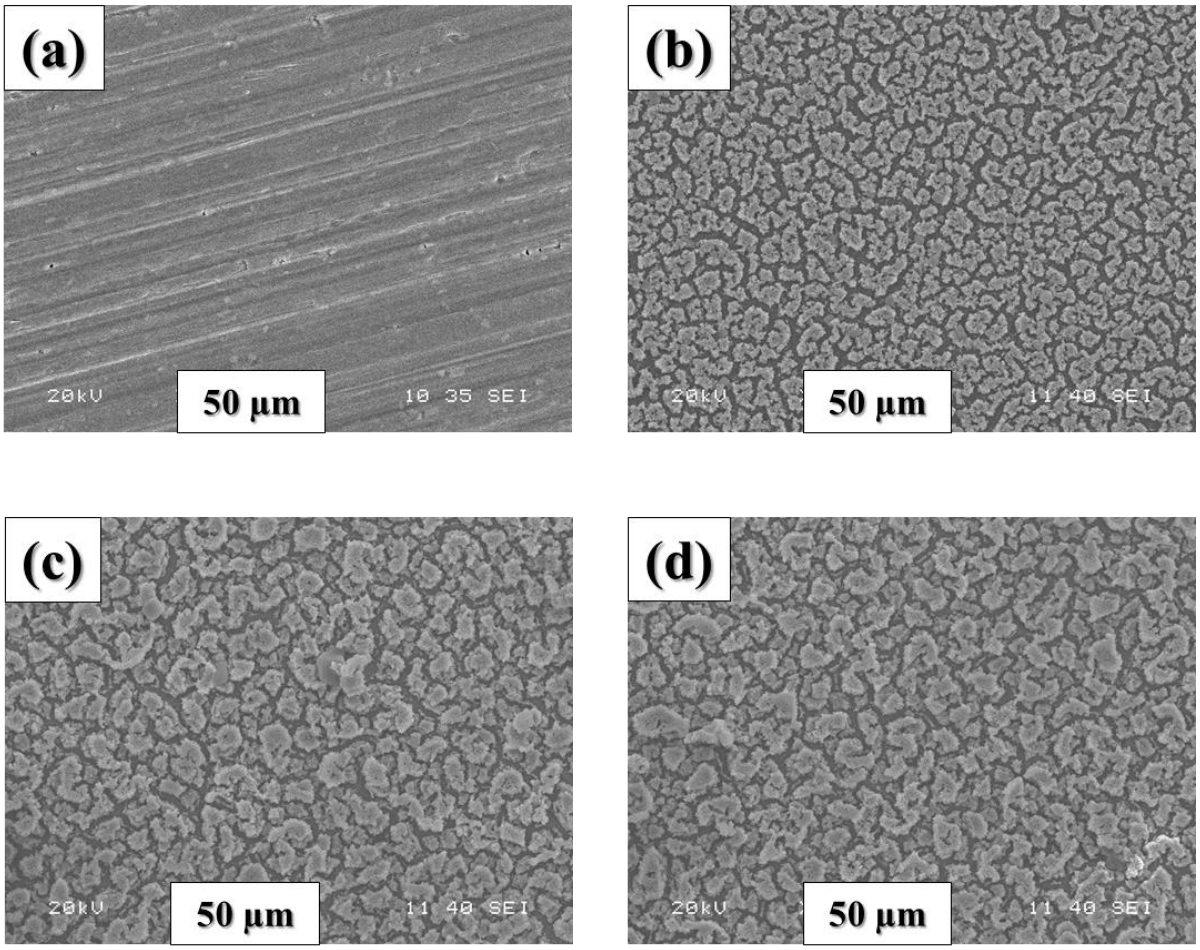

Figure 6.2: SEM images of (a) as-received Al substrate and zirconium silicate thin films after the aging time of the sol of (b) 24, (c) 48 h, (d) and 72 h.

Figure 6.3 shows the EDS pattern of zirconium silicate thin film after 72 h sol aging time. It can be seen from the graph that the thin film contains the elements of O and Si at their respective K_α positions of 0.5 and 1.7 keV. While the L_α peak of Zr is observed at the position of 2.04 keV.

It has to mention that the peak at 148 keV is related to the K_α of Al resulted from the metallic substrate.

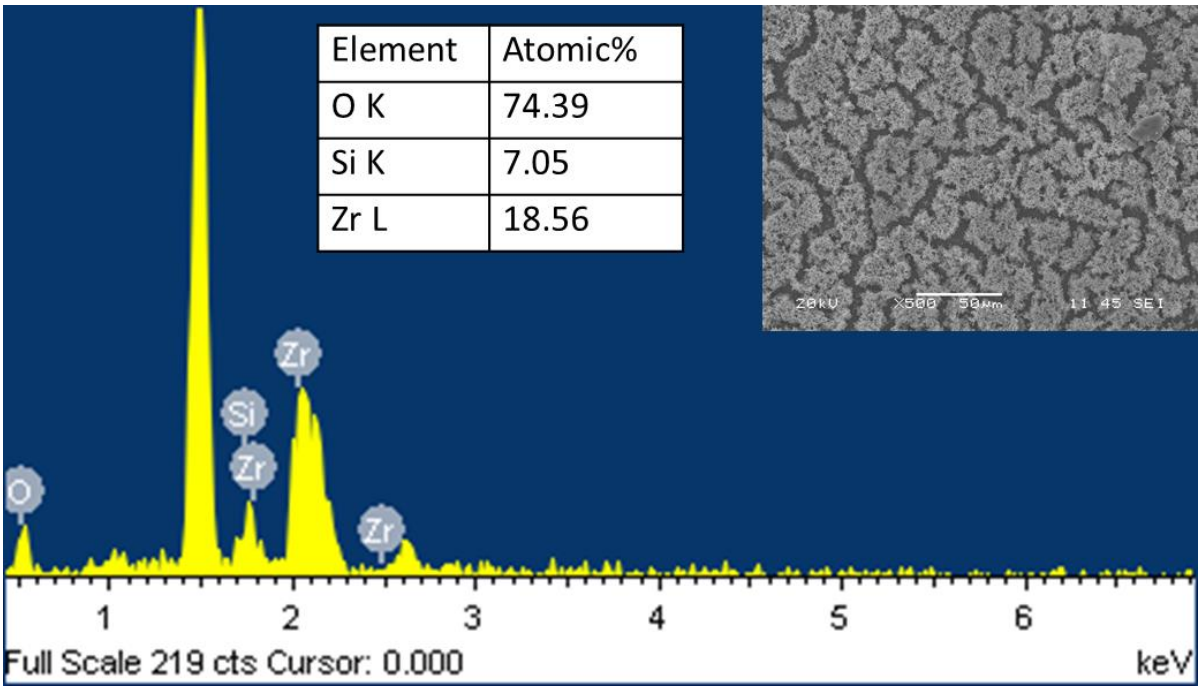

Figure 6.3: EDS spectrum of zirconium silicate thin film after 72 h sol aging time deposited on laminated AA6061-T6 aluminum alloy substrate using a spin coating process. The inset shows the selected EDX inspection field and the table displays the elemental analysis results.

ATR-FTIR analysis has been carried out to identify the functional groups of the investigated thin films. Figure 6.4 (a) shows the ATR-FTIR spectra of zirconium silicate thin films on Al substrates with the aging time of the sol of 1, 24, 48, and 72 h. The first peak observed at 501 cm^{-1} is attributed to the vibration of the Zr-O bending mode, while the peak at 811 cm^{-1} corresponds to the symmetric stretching mode of the Si-O-Si bond. The peak at around 1052 cm^{-1} followed by a shoulder at 1166 cm^{-1} is attributed to the stretching mode of Si-O-Si vibration [17].

The spectrum related to 72 h aging time of the sol indicates a shoulder at 940 cm^{-1} which may be attributed to Si-O-Zr asymmetric stretching vibration resulted from the reaction between Zr-OH

and Si-OH formed by hydrolysis of TEOS [18]. A similar Si-O-Zr bond at the wavenumber range of 920-950 cm^{-1} was reported by Castro *et al.* [19]. Additionally, the absorption peak at the range of 920-950 cm^{-1} has been reported by Brassard *et al.* for the Si-O-Ti linkages in $Ti_xSi_{1-x}O_2$ composition [20]. On the other hand, Figure 6.4 (b) illustrates the effect of aging time of the sol on the peak area at the wavenumber range of 870-1260 cm^{-1}, which is related to Si-O-Si and Si-O-Zr vibrations. It can be seen that with the increase of the aging time of the sol, the area under the peak increases, which indicates that more Si-O-Si and Si-O-Zr bonds are forming leading to a higher thickness of the zirconium silicate thin films [21].

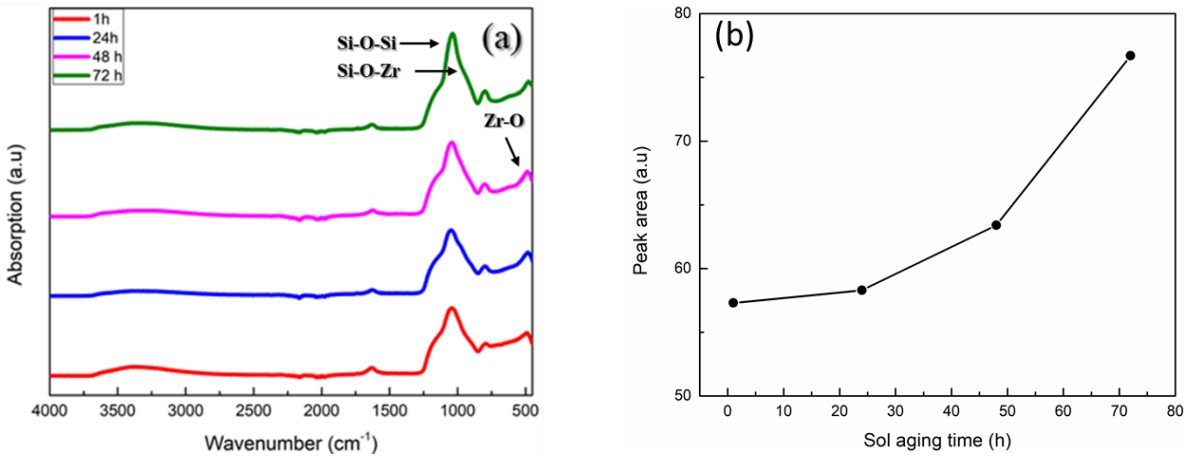

Figure 6.4: (a) ATR-FTIR curves of zirconium silicate thin films on Al substrates by the sol-gel process after the aging times of the sol of 1, 24, 48, and 72 h, (b) presents the variation of the peak area between 870-1260 cm^{-1} with the aging time of the sol.

Figure 6.5 shows the potentiodynamic polarization curves of the as-received Al substrate and zirconium silicate films fabricated after the sol aging times of 1, 24, 48, and 72 h. The corrosion

potential (E_{corr}) and the corrosion current density (I_{corr}) were determined from the extrapolation of the anodic and cathodic Tafel slopes, while the polarization resistance, R_p, was calculated using the Stern-Geary equation, given by the Equation (6-1).

$$R_p = \frac{\beta a \beta c}{2.3 I corr(\beta a + \beta c)} \quad (6\text{-}1)$$

Where, βa and βc are the anodic and cathodic Tafel slopes, respectively.

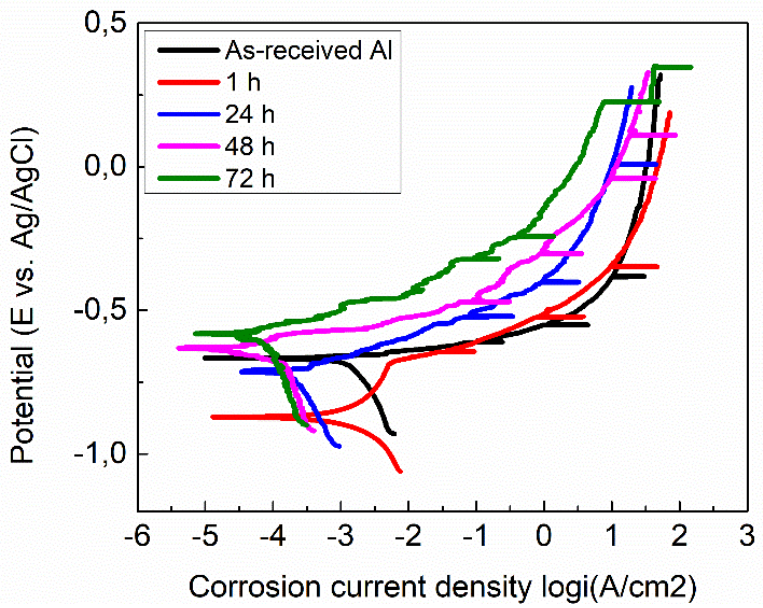

Figure 6.5: Potentiodynamic polarization curves of as-received Al substrate and zirconium silicate thin films on Al substrates by spin coating process after the sol aging times of 1, 24, 48, and 72 h.

Table 6.1 lists the electrochemical parameters obtained from the potentiodynamic polarization curves. The value of the corrosion potential, E_{corr}, the corrosion current density, I_{corr}, and the polarization resistance, R_p, were determined by extrapolation of the Tafel lines. The results of the coated samples were better than those obtained with as-received Al substrate, which resulted from the formation of zirconium silicate protective thin films on Al substrates. The as-received Al substrate exhibited an I_{corr} and R_p of 10.6 $\mu A.cm^{-2}$ and 10 $k\Omega.cm^2$, respectively, while the I_{corr} and the R_p of the zirconium silicate thin film fabricated after aging time of the sol of 1 h were found to be 0.59 $\mu A.cm^{-2}$ and 24 $k\Omega.cm^2$, respectively. It has been demonstrated that larger polarization resistance and a lower corrosion current density indicate higher corrosion protection properties. Furthermore, the I_{corr} and the R_p of the zirconium silicate thin film fabricated after the aging time of the sol of 24 h were found to be 0.3 $\mu A.cm^{-2}$ and 234 $k\Omega.cm^2$, respectively. The enhanced corrosion properties with the aging time could be due to the formation of a dense cross-linked thin film, which reduces the penetration of the corrosive ions to the Al substrate [23].

Table 6.1: Corrosion parameters determined from the potentiodynamic curves measured in 3.5 wt.% NaCl solution at room temperature: Corrosion potential E_{corr}, corrosion current density I_{corr}, and polarization resistance R_p.

Sample	Corrosion potential E_{corr} (mV)	Corrosion current density I_{corr} ($\mu A/cm^2$)	Polarization resistance R_p ($k\Omega.cm^2$)
As-received aluminum	-650	10.6	10
Aged 1 h	-875	0.59	24
Aged 24 h	-656	0.3	234

Aged 48 h	-685	0.07	390
Aged 72 h	-584	0.04	446

Furthermore, the I_{corr} and the R_p of the zirconium silicate thin film fabricated after the aging time of the sol of 48 h were found to be 0.07 $\mu A.cm^{-2}$ and 390 $k\Omega.cm^2$, respectively. Finally, the zirconium silicate thin film fabricated after the aging time of the sol of 72 h exhibited an I_{corr} and R_p of 0.04 $\mu A.cm^{-2}$ and 446 $k\Omega.cm^2$, respectively. Similarly, Rodic *et al.* [18] studied the corrosion properties of a hybrid organic-inorganic coating of zirconium and silicate films on 7075 Al alloy by a sol-gel process. The potentiodynamic polarization tests, performed in Harrison's solution (3.5 g/L $(NH_4)_3SO_4$, 0.5 g/L NaCl, pH 5.2), shows that the increase of the sol aging time increases the corrosion properties of the coating. They concluded that the aging process affects primarily the resistance to localized corrosion since the pitting potential E_{pitt} shifted to more positive values.

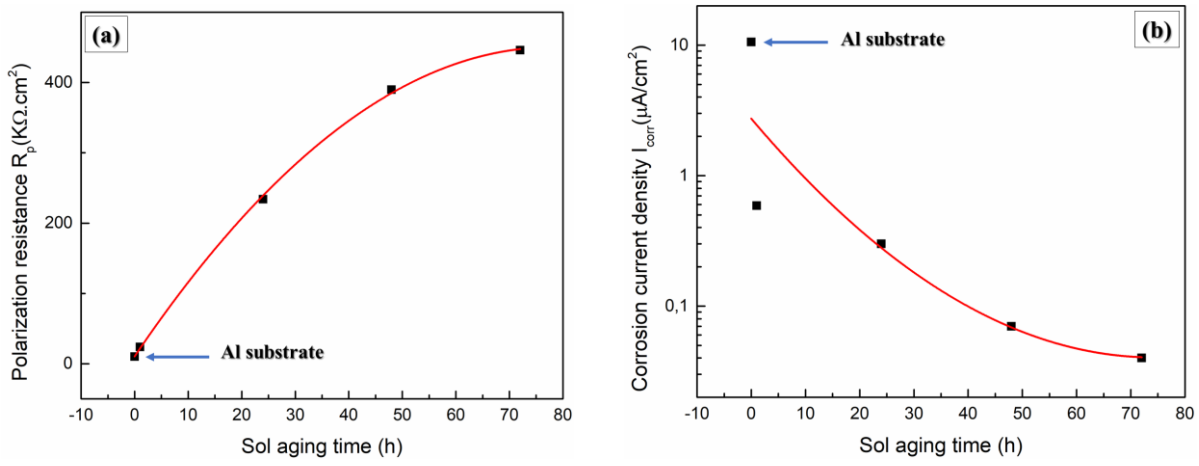

Figure 6.6: The variation of the (a) polarization resistance R_p and the (b) corrosion current density I_{corr} of zirconium silicate thin films on Al substrate with

the sol aging time. The as-received Al substrate was also presented in the two figures.

The variations of R_p and I_{coor} with the sol aging time are illustrated in Figure 6.6 (a) and Figure 6.6 (b), respectively. With the increase of the sol aging time, the R_p of the zirconium silicate thin films increase and their I_{corr} decreases. These results indicate the good properties of zirconium silicate thin films in protecting Al against corrosion.

Furthermore, the effect of the Si/Zr molar ratio on the corrosion properties of the zirconium silicate thin films was studied. The aging time of the sol was fixed at 72 h for the zirconium silicate thin films with different Si/Zr molar ratios. Figure 6.7 shows the SEM images of the as-received Al substrate and the zirconium silicate thin films fabricated with the Si/Zr molar ratio of 0, 0.5 and 5. Figure 6.7 (a) shows the SEM image of the as-received Al substrate, which exhibits parallel lines due to the rolling process. Further, Figure 6.7 (b) presents the SEM image of the zirconium silicate thin film fabricated with the Si/Zr molar ratio of 0 (only zirconium (IV) n-propoxide). This thin film exhibits an island-like morphology, which allows the penetration of the corrosive ions to the Al substrates resulting in a week corrosion property as shown further in Figure 6.9. Furthermore, Figure 6.7 (c) shows the SEM images of the zirconium silicate thin film fabricated with the Si/Zr molar ratio of 0.5. The formed thin film shows similar morphology of the thin film fabricated only from zirconium (IV) n-propoxide. However, a significant increase in the coverage area is observed. On the other hand, the zirconium silicate thin film fabricated from the Si/Zr molar ratio of 5 demonstrates a compact and homogenous morphology as shown in Figure 6.7 (d). The addition of the TEOS promoted the formation of the silica network. Consequently, more active

sites (i.e. O-Si-O, and Si-O-Zr) are available to bond with the Al surface, which increases the Al-O-Si/Zr bond density and enhances the compactness of the formed thin films [23].

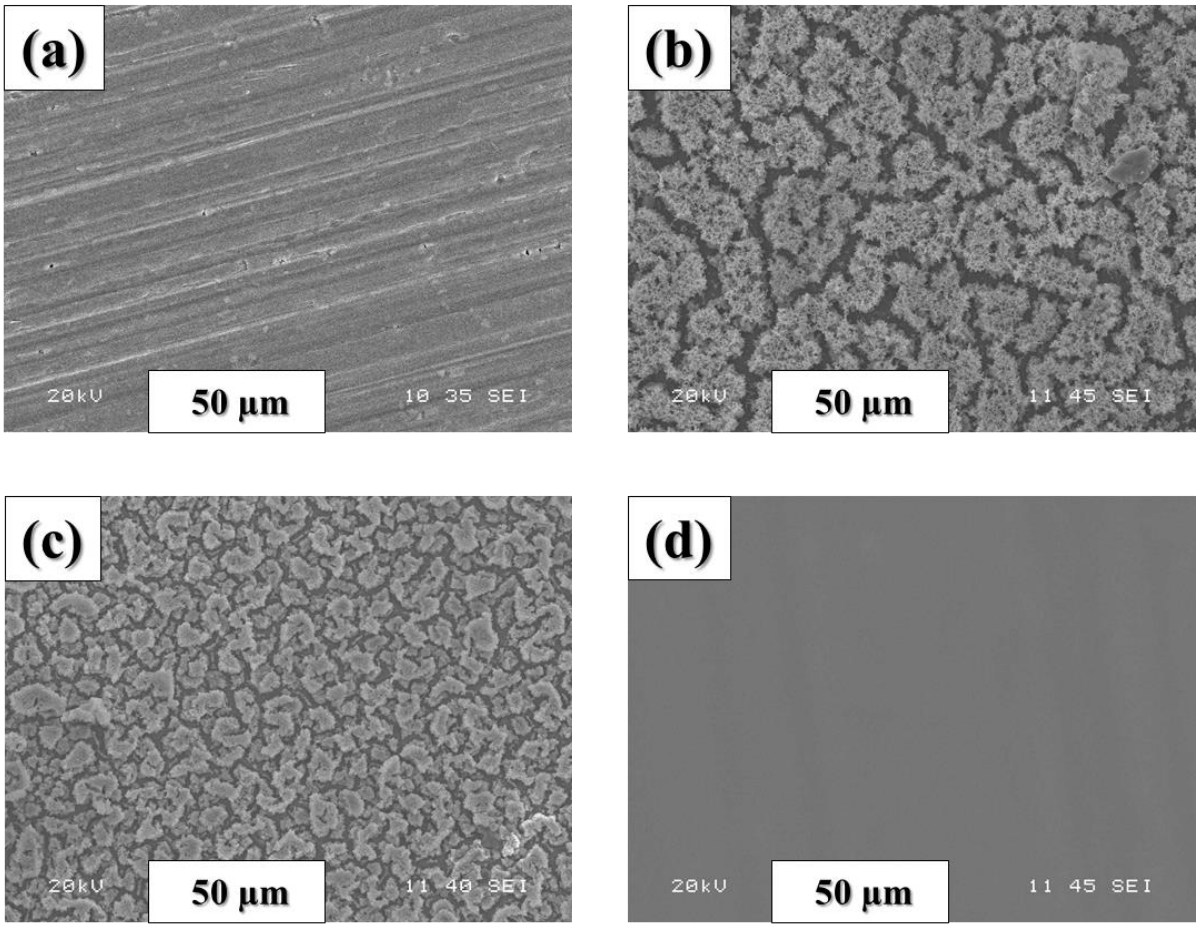

Figure 6.7: SEM images of the as-received Al substrate and the zirconium silicate thin films with the Si/Zr molar ratio of 0, 0.5, and 5.

Figure 6.8 shows the ATR-FTIR spectra of zirconium silicate thin films fabricated with the Si/Zr molar ratio of 0, 0.5, and 5 after the aging time of 72 h. Figure 6.8 (a) shows the ATR-FTIR spectrum of the thin film fabricated from the Si/Zr molar ratio of 0 (only zirconium(IV) n-propoxide). The peak at around 950 cm^{-1} is assigned to the vibration of O-Zr-O [24]. Furthermore, the remarkable peaks at 1440 and 1550 cm^{-1} correspond to the Zr-O-C and COO^{-}-Zr bonds, respectively [23].

Figure 6.8 (b) shows the ATR-FTIR spectrum of the thin film fabricated from the Si/Zr molar ratio of 0.5. The first peak observed at 501 cm^{-1} is attributed to the vibration of the Zr-O bending mode, while the peak at 811 cm^{-1} corresponds to the symmetric stretching mode of the Si-O-Si bond. The peak at around 1052 cm^{-1} followed by a shoulder at 1166 cm^{-1} is attributed to the stretching mode of Si-O-Si vibration [17]. The shoulder at 940 cm^{-1} which may be attributed to Si-O-Zr asymmetric stretching vibration resulted from the reaction between Zr-OH and Si-OH formed by hydrolysis of TEOS [18]. A similar Si-O-Zr bond at the wavenumber range of 920-950 cm^{-1} was reported by Castro *et al.* [19]. Additionally, the absorption peak at the range of 920-950 cm^{-1} has been reported by Brassard *et al.* for the Si-O-Ti linkages in $Ti_xSi_{1-x}O_2$ composition [20].

Figure 6.8 (c) shows the FTIR spectrum of the thin film fabricated from the Zr/Si molar ratio of 5. The peak related to the vibration of Si-O-Si increases with the increase of the Si/Zr molar ratio, which indicates that more Si-O-Si bonds are forming.

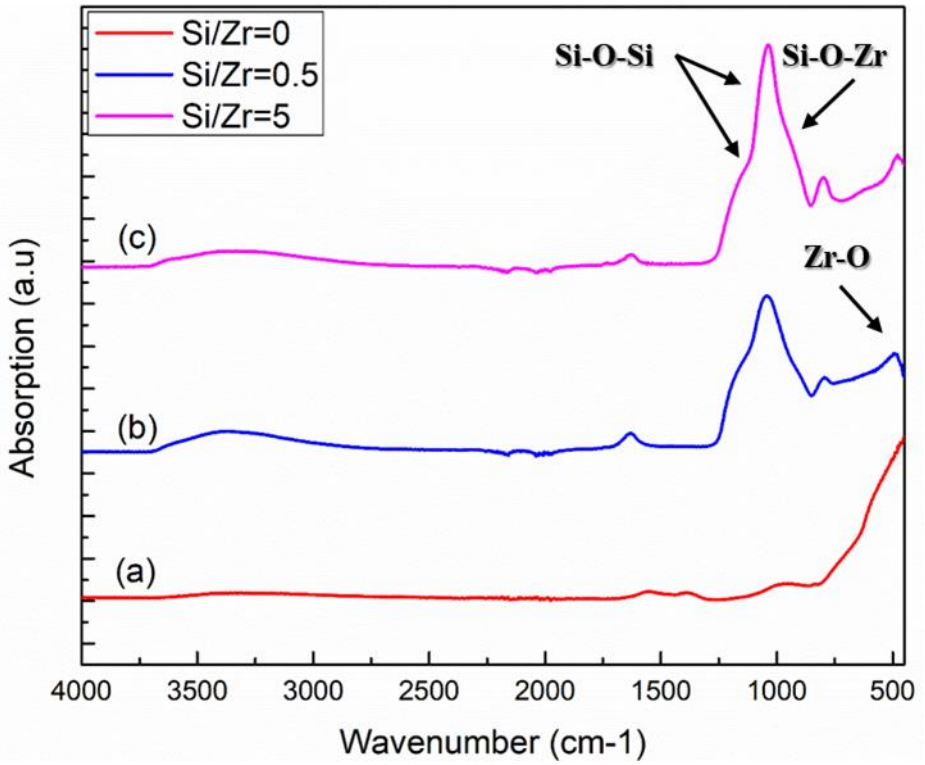

Figure 6.8: ATR-FTIR peaks of zirconium silicate thin films with the Si/Zr molar ratios of (a) 0 (b) 0.5 and (c) 5.

Figure 6.8 shows the potentiodynamic polarization curves (Tafel) of the as-received Al substrate and the zirconium silicate thin films fabricated with the Si/Zr molar ratio of 0, 0.5, and 5 after the aging time of the sol of 72 h.

Table 6.16.2 lists the electrochemical parameters obtained from the polarization curves. The value of the corrosion potential, E_{corr}, the corrosion current density, I_{corr}, and the polarization resistance, R_p, were determined by extrapolation of the Tafel lines. The results of the coated samples were better than those obtained with as-received Al substrate, which resulted from the formation of zirconium silicate protective thin films on Al. The as-received Al substrate exhibited an I_{corr} and

R_p of 10.6 µA.cm^{-2} and 10 kΩ.cm^2, respectively, while the I_{corr} and R_p of the thin film fabricated with the Si/Zr molar ratio of 0 were found to be 0.3 µA.cm^{-2} and 87 kΩ.cm^2, respectively.

Furthermore, the I_{corr} and the R_p of the thin film fabricated with the Si/Zr molar ratio of 0.5 were found to be 0.06 µA.cm^{-2} and 431 kΩ.cm^2, respectively. The enhanced corrosion properties with the Zr/Si molar ratio of 0.5 could be due to the formation of a dense cross-linked thin film, which reduces the penetration of the corrosive ions to the Al substrate [22]. Finally, a further increase in the Si/Zr molar ratio results in an I_{corr} and R_p of 0.05 µA.cm^{-2} and 598 kΩ.cm^2, respectively.

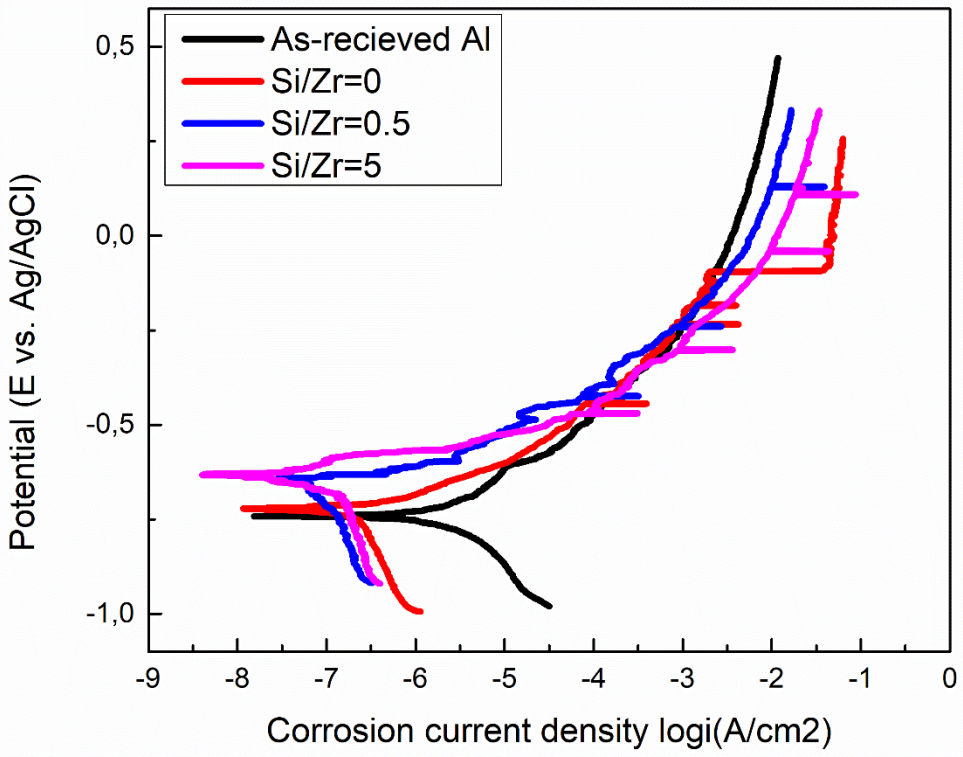

Figure 6.9: Potentiodynamic polarization curves of as-received Al substrate and zirconium silicate thin films with the Si/Zr molar ratio of 0, 0.5 and 5 after the aging time of the sol of 72 h.

Table 6.2: The corrosion potential, E_{corr}, the corrosion current density, I_{corr}, and the polarization resistance, R_p,. of as-received Al substrate and zirconium silicate thin films with the Si/Zr molar ratio of 0, 0.5 and 5 after the aging time of the sol of 72 h.

Sample (Si/Zr molar ratio)	Corrosion potential E_{corr} (mV)	Corrosion current density I_{corr} ($\mu A/cm^2$)	Polarization resistance R_p ($k\Omega.cm^2$)
As-received aluminum	-650	10.6	10
0	-726	0.3	87
0.5	-584	0.06	446
5	-649	0.05	598

6.4 **Conclusion**

The zirconium silicate thin films fabricated by sol-gel process improved the corrosion resistance properties of aluminum. After the aging time of the sol of 72 hours, the polarization resistance of the thin film was found to be 446 $k\Omega.cm^2$ compared to 10 $k\Omega.cm^2$ for as-received Al substrate. The SEM analysis shows the formation of zirconium silicate micro grains with uniform coverage area on the metallic substrate. Finally, the ATR-FTIR studies suggest that the increase of the sol aging time increases the thickness of the thin films, which improves their resistance against corrosion. These results of this study shows promises in reducing the corrosion of aluminum in corrosive environments which can find potential application in many industrial applications.

References

[1] C.J. Donahue, J.A. Exline, Anodizing and Coloring Aluminum Alloys, J. Chem. Educ. 91 (2014) 711–715.

[2] Z. Li, N. Li, D. Wang, D. Ouyang, L. Liu, Low temperature deformation behavior of an electromagnetically bulged 5052 aluminum alloy, Sci. Rep. 6 (2016) 29973.

[3] M. Liang, R. Melchers, I. Chaves, Corrosion and pitting of 6060 series aluminium after 2 years exposure in seawater splash, tidal and immersion zones, Corros. Sci. (2018).

[4] P.E. Hintze, L.M. Calle, Electrochemical properties and corrosion protection of organosilane self-assembled monolayers on aluminum 2024-T3, Electrochim. Acta. 51 (2006) 1761–1766.

[5] J. Zhao, L. Xia, A. Sehgal, D. Lu, R.L. McCreery, G.S. Frankel, Effects of chromate and chromate conversion coatings on corrosion of aluminum alloy 2024-T3, Surf. Coatings Technol. 140 (2001) 51–57.

[6] W.J. Clark, J.D. Ramsey, R.L. McCreery, G.S. Frankel, A Galvanic Corrosion Approach to Investigating Chromate Effects on Aluminum Alloy 2024-T3, J. Electrochem. Soc. 149 (2002) B179.

[7] C. Pellerin, S.M. Booker, Reflections on hexavalent chromium: Health hazards of an industrial heavyweight, Environ. Health Perspect. 108 (2000) 402–407.

[8] H.J. Gibb, P.S. Lees, P.F. Pinsky, B.C. Rooney, Lung cancer among workers in chromium chemical production., Am. J. Ind. Med. 38 (2000) 115–26.

[9] N. Kumar, A. Jyothirmayi, K.R.C.S. Raju, V. Uma, R. Subasri, Silica-Zirconia Self-

Healing Coating on Aluminum, 2013 (2013).

[10] N. Pirhady Tavandashti, S. Sanjabi, T. Shahrabi, Evolution of corrosion protection performance of hybrid silica based sol-gel nanocoatings by doping inorganic inhibitor, Mater. Corros. 62 (2011) 411–415.

[11] Z. Feng, Y. Liu, G.E. Thompson, P. Skeldon, Sol–gel coatings for corrosion protection of 1050 aluminium alloy, Electrochim. Acta. 55 (2010) 3518–3527.

[12] E. Gonzalez, J. Pavez, I. Azocar, J.H. Zagal, X. Zhou, F. Melo, G.E. Thompson, M.A. Páez, A silanol-based nanocomposite coating for protection of AA-2024 aluminium alloy, Electrochim. Acta. 56 (2011) 7586–7595.

[13] A.-P. Romano, M. Fedel, F. Deflorian, M.-G. Olivier, Silane sol–gel film as pretreatment for improvement of barrier properties and filiform corrosion resistance of 6016 aluminium alloy covered by cataphoretic coating, Prog. Org. Coatings. 72 (2011) 695–702.

[14] A.K. Singh, J.K. Singh, Fabrication of zirconia based durable superhydrophobic-superoleophilic fabrics using non fluorinated materials for oil-water separation and water purification, RSC Adv. 6 (2016) 103632–103640.

[15] H. Li, K. Liang, L. Mei, S. Gu, S. Wang, Corrosion protection of mild steel by zirconia sol-gel coatings, J. Mater. Sci. Lett. 20 (2001) 1081–1083.

[16] Q.P. Li, Z.Q. Yan, Q. Xu, B. Zhang, S. Sun, J.G. Liu, C.W. Yan, A high-performance Ti-Zr Based Chromium-Free Conversion Coating on 2024 Aluminum Alloy, Int. J. Electrochem. Sci. 1112 (2016) 10675–1068939. doi:10.20964/2016.12.39.

[17] V. Ramaswamy, Crystalline, Microporous Zirconium Silicates with MEL Structure, J.

Catal.
https://www.academia.edu/24200025/Crystalline_Microporous_Zirconium_Silicates_with_MEL_Structure

[18] P. Rodič, J. Iskra, I. Milošev, A hybrid organic–inorganic sol–gel coating for protecting aluminium alloy 7075-T6 against corrosion in Harrison's solution, J. Sol-Gel Sci. Technol. 70 (2014) 90–103.

[19] Y. Castro, M. Aparicio, R. Moreno, A. Durán, Silica-Zirconia Sol–Gel Coatings Obtained by Different Synthesis Routes, J. Sol-Gel Sci. Technol. 35 (2005) 41–50.

[20] D.K. Sarkar, D. Brassard, M.A. El Khakani, L. Ouellet, Dielectric properties of sol–gel derived high-k titanium silicate thin films, Thin Solid Films. 515 (2007) 4788–4793.

[21] Y. Li, X. Cheng, W. Cao, L. Gong, R. Zhang, H. Zhang, Fabrication of adiabatic foam at low temperature with sodium silicate as raw material, Mater. Des. 88 (2015) 1008–1014.

[22] H.-I. Hsiang, S.-C. Lin, Effects of aging on nanocrystalline anatase-to-rutile phase transformation kinetics, Ceram. Int. 34 (2008) 557–561.

[23] C.J. Fu, W. Zhan, M. Yu, S.M. Li, H. Liu, L. Dong, Influence of Zr/Si Molar Ratio on Structure, Morphology and Corrosion Resistance of Organosilane Coatings Doped with Zirconium(IV) n-propoxide, 2014.

[24] R. Arreche, N. Bellotti, M. Blanco, P. Vázquez, Synthesis and Characterization of Zirconium Oxides for Use as Antimicrobial Additives in Paints, Procedia Mater. Sci. 9 (2015) 627–634.

CHAPTER 7: FACILE ELECTRODEPOSITION PROCESS OF ZIRCONIUM-BASED SUPERHYDROPHOBIC THIN FILMS ON ALUMINUM

CHAPTER 7 : FACILE ELECTRODEPOSITION PROCESS OF ZIRCONIUM-BASED SUPERHYDROPHOBIC THIN FILMS ON ALUMINUM

Abstract

The development of corrosion resistant superhydrophobic thin films on aluminum surfaces has attracted great interest for industrial applications. In the present work, zirconium-based superhydrophobic thin films were fabricated on laminated AA6061-T6 aluminum alloy substrates by a simple electrodeposition process. The thin film coated Al substrate exhibited excellent superhydrophobicity with a higher water contact angle of 165 ± 3˚ compared to the hydrophilic as-received Al substrate with a contact angle of 83 ± 2˚. The surface morphology of the fabricated thin films on Al substrate shows uniform micro-nano porous structures. The polarization resistance of the as-received Al and the zirconium-based superhydrophobic thin films on the Al substrate are 23 kΩ.cm^2 and 788 kΩ.cm^2, respectively. These results show excellent anti-corrosion property of zirconium-based superhydrophobic thin films to provide high corrosion protection for Al substrates.

7.1 **Introduction**

Superhydrophobic surfaces are characterized by apparent water contact angle greater than 150˚ and low contact angle hysteresis [1]. Inspired by nature, studies reveal that the combination of surface roughness and low surface energy material can realize superhydrophobicity [2,3]. Nowadays, superhydrophobic surfaces attract a great deal of interest in various fields of applications due to their self-cleaning, anti-corrosion, anti-icing, and oil-water separation properties [4–7].

Aluminum (Al) alloys have attracted high interest in many applications due to their high strength, low cost and high-performance [8], these materials are used in aerospace, automobile, aircraft, boats, electronic industries, etc. [9,10]. Despite their good properties, Al alloys show weak resistance to corrosion in marine environments resulting from the penetration of chloride ions to the protective oxide film formed on alumina [11,12], which limits their applications. One of the current industrial strategies to protect metals against corrosion by applying superhydrophobic coatings with self-cleaning properties. Such coating provides excellent anti-corrosion properties to protect metal surfaces, especially for Al and its alloys. In that regard, many researchers reported the effect of superhydrophobic protective thin films on the Al surfaces [13-16]. Huang *et al*. [14] reported the synthesis of superhydrophobic thin films on Al alloy substrates, with good corrosion resistance properties, using chemical etching by nitric acid, and an ethanolic stearic acid solution was used for passivation. In another study, Li *et al*. [15] reported the fabrication of superhydrophobic Al surface with a water contact angle of 155.7° using hydrochloric acid followed by potassium permanganate passivation and modification by fluoroalkyl-silane. The surface morphology of the samples showed hierarchical terrace-like structures and a nano-scale

coral-like network of bulge structures. The superhydrophobic behavior of the surfaces was due to nano-microstructural morphology and its low surface energy [16].

A number of materials were used in our group, in the fabrication of superhydrophobic thin films for the corrosion protection of Al alloys, such as cobalt, zinc, copper, and nickel [17–21]. Fan *et al*. reported the fabrication of the Zr-based superhydrophobic thin films via electrodeposition process on carbon fiber fabrics for the separation of the water-oil mixture. and Goutam [24] reported the fabrication of Zr-based superhydrophobic thin films on the cotton fabrics. In their work, the superhydrophobic thin films were synthesized by the immersion of dried cotton fabrics in homogenized fluorinated silyl-functionalized zirconia solution. They have reported that the coated fabrics show good washing durability, water repellency, and self-cleaning ability.

Although zirconium-based materials have several applications, studies on the corrosion protection of Al by zirconium-based materials are less reported. As far as corrosion studies on the Zr-based thin films are concern, typically, they are hydrophilic in nature and applied on different metals. Haibin *et al*. [25] reported the use of Zr-based thin films for the corrosion protection of mild steel. In their work, they have deposited Zr-based hydrophilic thin films on flat sheets of mild steel by dip-coating process. They have reported that the polarization resistance of the Zr-based thin films was 299 $\Omega.cm^2$ as compared to 40 $\Omega.cm^2$ for as-received steel substrates in 1 M HCl solution. Li *et al*. [26] studied the corrosion properties of the Zr-based conversion thin films on Al substrates. They have reported a polarization resistance of 47 $k\Omega.cm^2$ for the Zr-based thin films compared to 13 $k\Omega.cm^2$ for as-received Al substrate.

On the other hand, there have been few works on the corrosion study of zirconium-based superhydrophobic thin films, such as the work done by Chen *et al.* where they fabricate superhydrophobic palmitate film on steel substrates. They reported a corrosion current density

(I_{corr}) of 19.5 µA/cm^2 for the steel substrate compared to 0.92 µA/cm^2 for the superhydrophobic palmitate film. The decrease in I_{corr} values indicates the better corrosion protection provided by the superhydrophobic thin film.

In this work, Zirconium-based thin films were successfully fabricated by one step electrochemical process on Al substrates. The morphology, chemical composition, wettability, and corrosion behavior of the synthesized Zr-based superhydrophobic thin films on Al substrate have been properly investigated.

7.2 **Experimental**

Laminated AA6061-T6 aluminum substrates of 1″ × 2″ with the chemical composition of Al 97.9 wt.%, Mg 1.08 wt.%, Si 0.63 wt.%, Mn 0.52 wt.%, Cu 0.32 wt.%, Fe 0.17 wt.%, Ti 0.02 wt.%, and V 0.01 wt.% were degreased in ultrasonic bath using soap water for 15 minutes, and then cleaned with deionized water and ethanol for 15 minutes. Further, the cleaned substrates were dried on hotplate at 100 °C for 18 hours. A mixture of Zirconium (IV) propoxide (ZrO_x) and ethanolic stearic acid (SA) solution was used as an electrolyte and two cleaned Al substrates separated at a distance of 2 cm were used as electrodes. The electrodeposition time was fixed at 10 minutes under a DC potential of 10 V. Electrolyte with different concentrations were prepared by varying the Zr/SA molar ratios. After the electro-deposition process, the samples were removed carefully from the chemical bath and dried the substrate at 70 °C for 10 hours in an air environment. The surface morphology of the fabricated thin films on Al substrate was characterized using a scanning electron microscope (SEM). The surface chemical composition was studied using Fourier-transform infrared spectroscopy (ATR-FTIR) and energy dispersive X-ray spectroscopy (EDS). The wetting properties of the fabricated thin films on Al substrates were carried out by measuring the static contact angle using a first ten-angstrom contact angle

goniometer. A three electrodes set-up, consisting of a platinum mesh (counter electrode), a silver/silver-chloride (Ag-AgCl) (reference electrode), and the Al samples (working electrodes) was employed for potentiodynamic polarization studies. The polarization curves were recorded at a sweep rate of 2 mV/s in a range of -250 mV to 1000 mV with respect to open circuit potential (OCP). The frequency range of electrochemical impedance spectroscopy (EIS) study was fixed between 10^{-2} and 10^{5} Hz with an amplitude of 20 mV with respect to OCP. All the electrochemical experiments were carried out in 3.5 wt.% NaCl solution (pH of 5.8) to simulate seawater.

7.3 **Results and discussion**

Figure 7.1 (a) shows the SEM image of the as-received Al substrate, which exhibited a surface roughness of 0.41 ± 0.04 µm and a water contact angle (CA) of 83 ± 2˚ (shown in the inset of Figure 7.1 (a)). The as-received Al substrate exhibits parallel streaks which are resulting from the mechanical rolling operations [27]. Figure 7.1 (b) shows the surface morphology of the sample prepared by electrodeposition process in the ethanolic stearic acid bath. The CA of this sample was found to be increased to 100 ± 4˚ and this increase of CA results from the presence of the low surface energy radicals $-CH_2$ and $-CH_3$ on the metallic substrate [28]. Interestingly, the electrodeposition process performed in the electrolyte of the Zr/SA molar ratio of 1 leads to the formation of micro-nano structures on the Al substrate as shown in Figure 7.1 (c). The deposition of these micro-nano structures on the Al substrates under the effect of the electric field increases the CA of the surface to 107 ± 6˚. Further, when the Zr/SA molar ratio increased to a value of 2, as expected, more ZrSA compounds are formed leading to more amounts of deposits and higher coverage of micro-nano structures on the Al surface. This surface exhibits a CA of 114 ± 9˚ as

shown in the inset of Figure 7.1 (d). Figure 7.1 (e) shows the deposition of ZrSA compounds in complete coverage on the Al surface when the Zr/SA molar ratio in the electrolyte reached the value of 4. The morphology of the deposited thin film on the surface exhibits micro-nanostructures. The combination of micro-nanorough compounds and low surface energy stearate radicals transforms the Al surface to a superhydrophobic surface with the highest CA value of 165 ± 3˚. Further increase of Zr/SA molar ratio to 8, decreases the CA of the coated Al substrate to a value of 151 ± 4˚and is shown in Figure 7.1 (f). The decrease in the CA could be explained by the increase of the deposited cluster size, which leads to more micro-sized morphology. These results are supported by the roughness measurements discussed later in Figure 7.4.

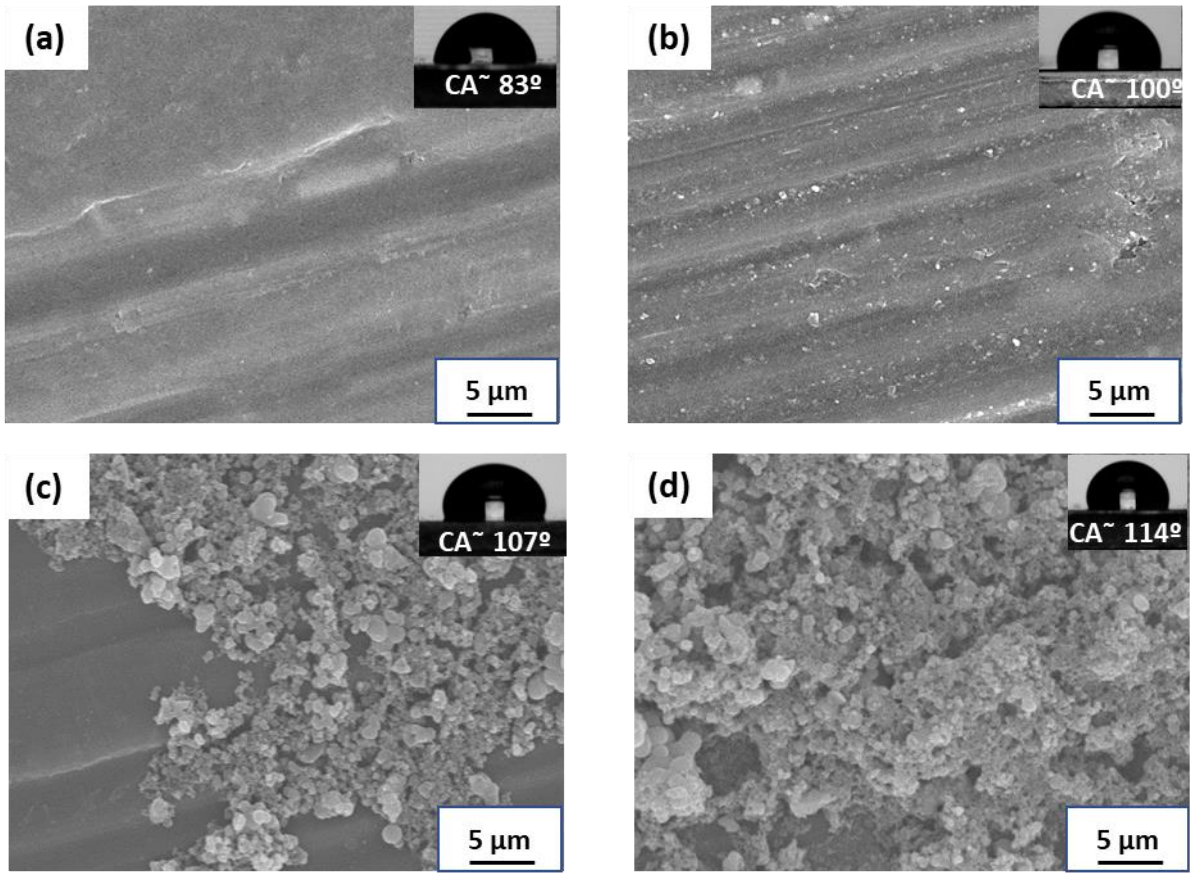

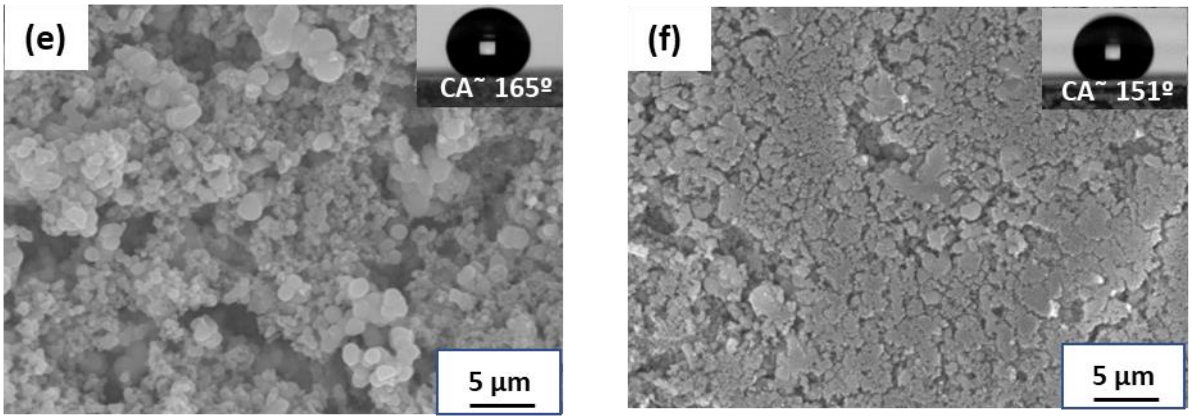

Figure 7.1: SEM images of (a) as-received Al substrate, and ZrSA thin films electrodeposited on the Al substrates with the Zr/SA molar ratio of (b) 0, (C) 1, (d) 2, (e) 4, and (f) 8, with the insets represent the corresponding CA values.

Figure 7.2 shows the EDS of the as-received Al substrate and the fabricated thin films with different Zr/SA molar ratios. The results of the elemental composition analysis are presented in Table 7.1. It can be seen from the EDS graphs that all the thin films contain the elements of C and O with their respective K_α peaks at 0.27 and 0.52 KeV. While the L_α peak of Zr is observed at 2.04 KeV for the thin films fabricated from the Zr/SA molar ratios of 1, 2, 4 and 8. It is to mention that the peak at 1.48 KeV is related to the K_α of Al resulted from the metallic substrate. The EDS for Zr/SA molar ratios of 4 and 8 show no peak related to Al, which is resulted from the higher thickness of the deposited thin films on the Al substrate as shown in Figure 7.4.

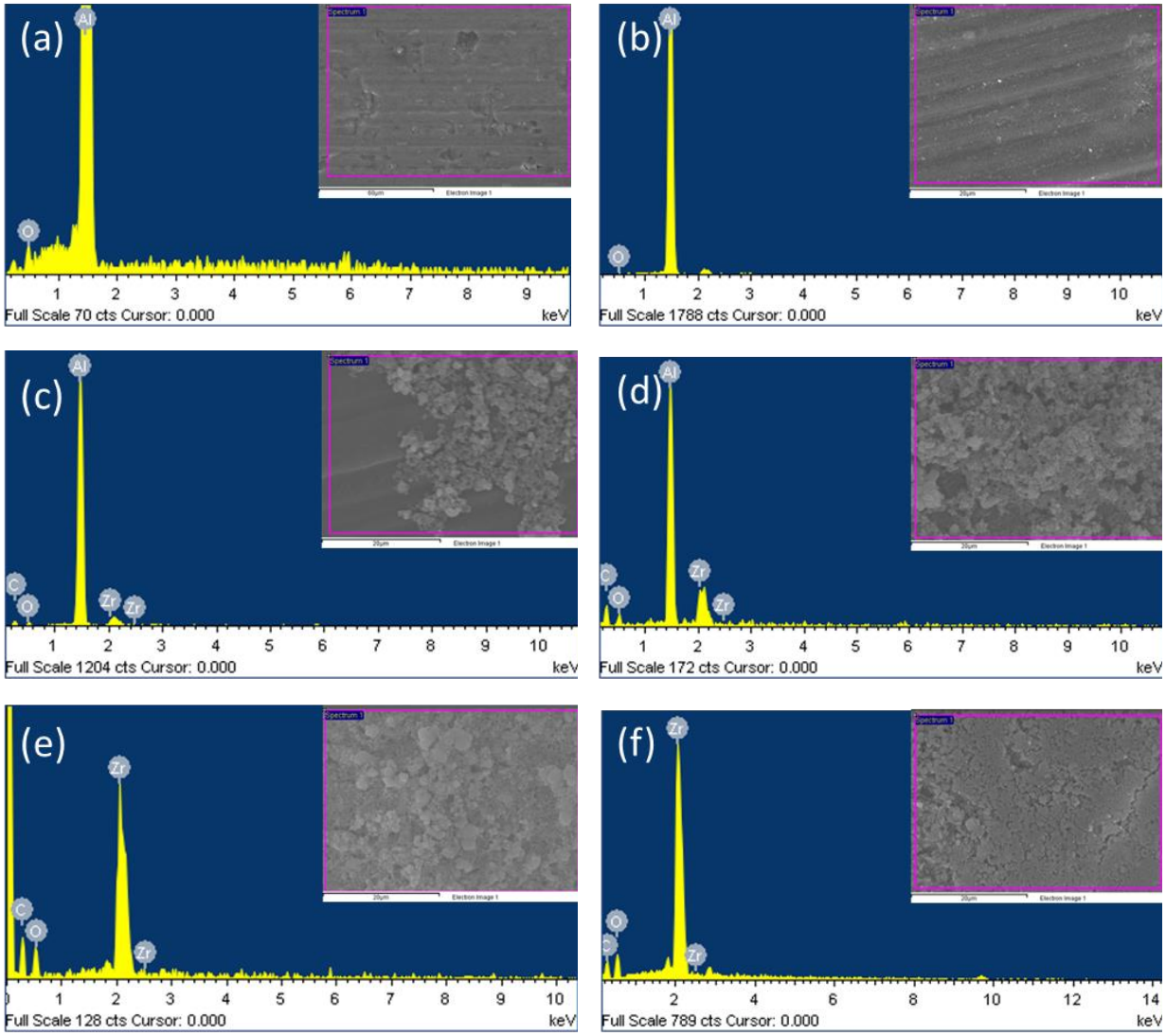

Figure 7.2: EDS spectra of (a) as-received Al substrate, and ZrSA thin films electrodeposited on the Al substrates with the Zr/SA molar ratio of (b) 0, (C) 1, (d) 2, (e) 4, and (f) 8. The insets of the images represent the corresponding SEM images.

The variation of the atomic percentage of zirconium with the Zr/SA molar ratio was illustrated in Figure 7.3 (a). It can be seen from the figure that the increase of Zr/SA molar ratio in the electrolyte leads to the increase of zirconium atomic percentage in the electrodeposited thin films. Furthermore, the variation of the atomic percentage of O/C with the Zr/SA molar ratio has been

presented in Figure 7.3 (b). The atomic ratio of O/C is found to increase with the increase of the Zr/SA molar ratio, which exhibits more zirconium oxide formation on the Al substrate.

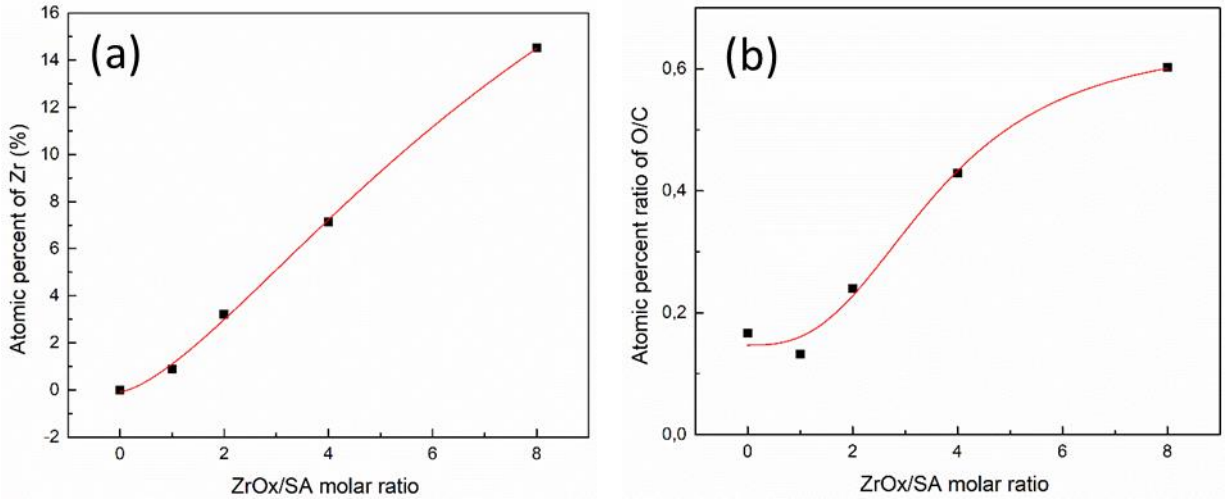

Figure 7.3: The evolution of the atomic percentage of (a) Zr and (b) the atomic percentage ratio of O/C in the fabricated thin films with the Zr/SA ratios of 0, 1, 2, 4 and 8.

Table 7.1: Elemental composition electrodeposited ZrSA thin films on Al substrate with different Zr/SA molar ratios.

Zr/SA molar ratio	Thin films chemical composition (at. %)		
	C	O	Zr
0	85.75	14.24	0
1	87.53	11.58	0.88
2	78.07	18.71	3.21
4	64.99	27.87	7.15
8	53.36	32.13	14.51

Figure 7.4 (a) illustrates the variation of the thickness of the fabricated thin films with Zr/SA molar ratio. With the increase of Zr/SA molar ratio, the thickness of the deposited thin films increases, and this could be explained by the deposition of more amount of ZrSA and zirconium oxide compounds on Al substrate under DC voltage. Furthermore, Figure 7.4 (b) represents the variation of the roughness of the ZrSA thin films. The roughness of the thin film fabricated from the Zr/SA molar ratio of 0 (only SA) is found to be 0.44 ± 0.02 μm compared to 0.41 ± 0.04 μm for as-received Al substrate. Similar roughness values have been reported previously in the literature [29]. Interestingly, the roughness of the thin film fabricated from Zr/SA molar ratio 1 found to be increased to 3.12 ± 0.16 μm, this increase in the roughness is related to the deposition of ZrSA compounds with the micro-nano rough structures on the Al surface. Furthermore, the roughness of the fabricated thin films reaches a maximum value of 8.18 ± 0.17 μm with the Zr/SA molar ratio of 4, which is resulted from the total coverage area of the thin film as shown in the SEM image. A slight decrease of the roughness was observed with the Zr/SA molar ratio of 8,

which could be resulted from the agglomeration of deposited compounds (ZrSA and ZrOx) on the Al surface.

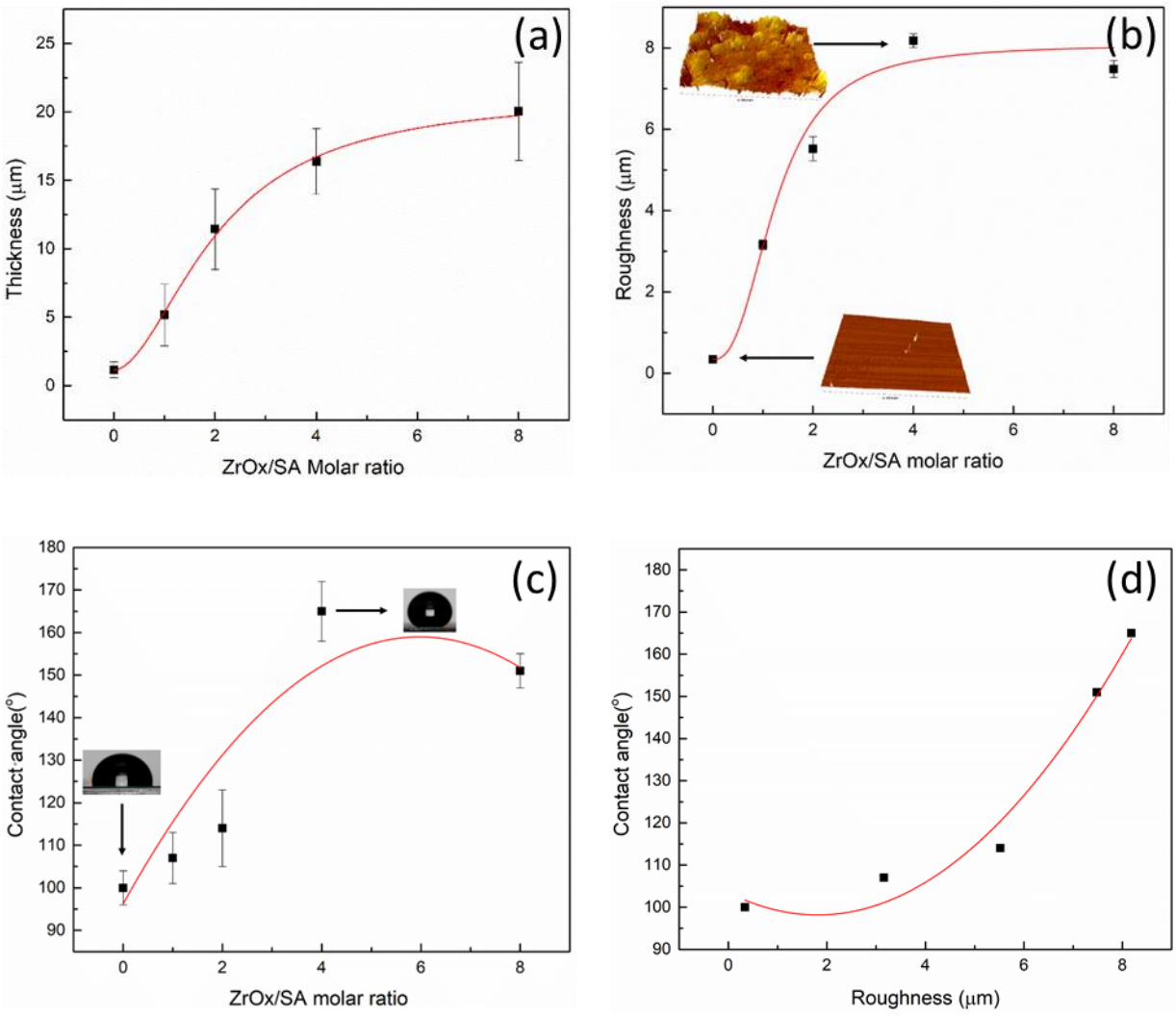

Figure 7.4: (a) The evolution of the thickness (b) the roughness (c) and the CA of the fabricated thin films with the Zr/SA molar ratios of 0, 1, 2, 4 and 8. (d) represents the variation of the CA with the roughness of the fabricated thin films.

Figure 7.4 (c) shows the evolution of the CA values of the fabricated thin films with the Zr/SA molar ratios of 0, 1, 2, 4, and 8. The CA reaches a maximum value of 165 ± 3˚ at the molar ratio of 4, this could be explained by the combination of high surface roughness and low surface energy of the fabricated thin film deposited on Al substrate. Further, a slight decrease of the CA was measured at the Zr/SA molar ratio of 8, which could be related to the decrease of the roughness of the thin film compared to the thin film fabricated from the Zr/SA molar ratio of 4. For better understanding, the variation of the CA of the ZrSA thin films with their roughness was illustrated in Figure 7.4 (d), and the results show that the CA is increasing with the increase of the roughness of the fabricated thin films.

The chemical composition of the ZrSA thin films on Al substrates was studied using ATR-FTIR analysis in the wavelength range of 450-4000 cm^{-1}. Figure 7.5 shows the spectra of the electrodeposited thin films with the Zr/SA molar ratios of 1, 2, 4 and 8. At the high-frequency region, the peaks of the relevant alkyl chain of -CH_2 and -CH_3 can be seen at the wavelength values of 2852, 2921 and 2961cm^{-1}, respectively [2,30]. Due to the presence of these alkyl groups, the surface energy of the electrodeposited ZrSA thin films decreases [31].

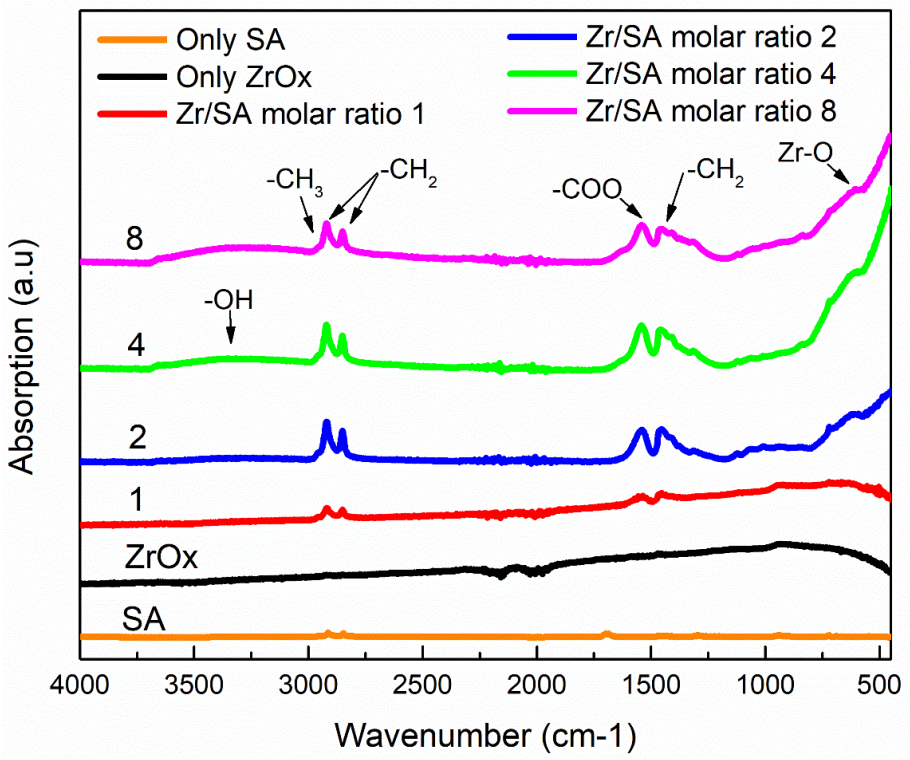

Figure 7.5: ATR-FTIR spectra of superhydrophobic ZrSA thin films with different Zr/SA molar ratios (1, 2, 4 and 8), stearic acid (Only SA), and ZrO_x(without SA) on the Al substrates.

Furthermore, the mid-frequency region exhibits a peak at 1542 cm^{-1}, this peak is related to the formation of COOZr bond in the fabricated thin films [32]. Similarly, the bond formation of COOCo and COOAl at the respective positions of 1550 and 1586 cm^{-1} were reported in our previous works [14,17]. The shift of the COOZr bond towards lower wavenumber compared to COOCo and COOAl bonds is due to the higher atomic number of Zr compared to Co and Al [14]. Another peak around 616 cm^{-1} is observed and that is assigned to Zr-O stretching mode, indicating the presence of zirconium oxide in the chemical composition of the fabricated thin films [33]. The ATR-FTIR spectra of the thin film fabricated from Zr/SA=0 (only SA) and ZrOx (Without SA) separately were presented in Figure 7.5, and no clear peak was observed.

The peak area analysis of the chemical bonds of -CH_3, -CH_2, and Zr-O was performed for the ATR-FTIR spectra of the electrodeposited thin films fabricated from the Zr/SA molar ratio of 0, 1, 2, 4 and 8, and the results are presented in Figure 7.6 (a). The peak area of CH_2 and CH_3 increases with the increase of Zr/SA molar ratio and reaches to a value of 2.28 for the ratio of 4, which indicates that more ZrSA compound is deposited uniformly on the Al surface. A slight decrease of the area was observed for the Zr/SA molar ratio of 8, which could be explained by the decrease in the SA molecules in the electrochemical bath and consequently less deposition on the substrate. On the other hand, the peak area of Zr-O increases gradually with the increase of the Zr/SA molar ratio in the electrolyte, which shows that more zirconium oxide is deposited on the Al substrate under the application of DC voltage of 10 V. Furthermore, Figure 7.6 (b) represents the variation of the peak area ratio of (Zr-O)/(-CH_3,-CH_2). The peak area ratio reaches a maximum value at the Zr/SA molar ratio of 8, indicating that more zirconium oxide (hydrophilic in nature) is deposited on the Al surface, which correlates the decrease of the CA to the value of 151˚ for this sample.

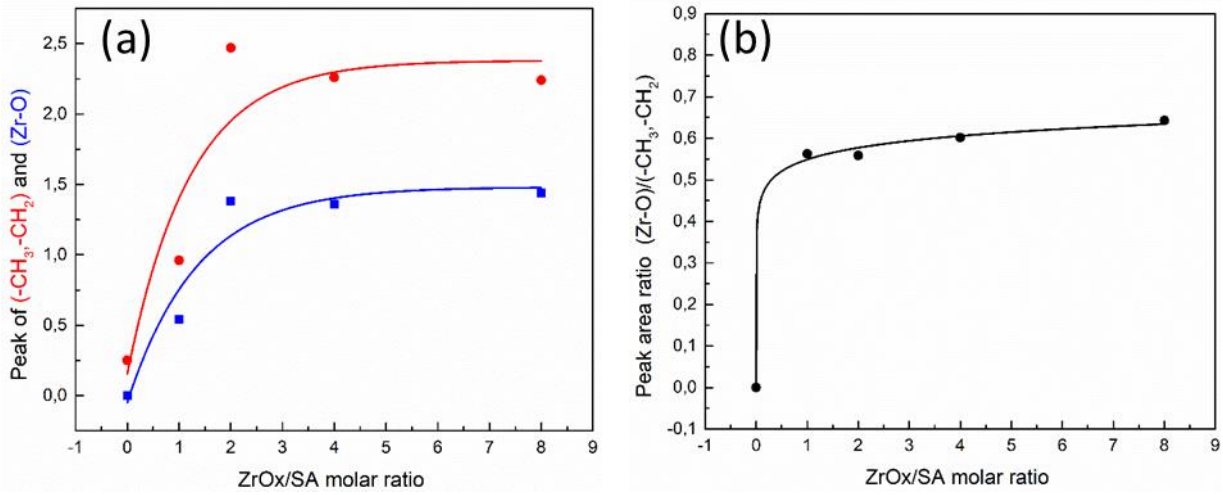

Figure 7.6: The variation of the peak area of (a) $-CH_3$ and CH_2 peaks (red squares), and Zr-O peak (Blue squares), (b) the ratio of peak area of $-CH_3$, CH_2, and Zr-O.

Figure 7.7 (a) shows the potentiodynamic polarization curves (Tafel curves) of the as-received Al substrate and ZrSA thin films deposited substrate. The corrosion potential (E_{corr}) and the corrosion current density (I_{corr}) were determined from the extrapolation of the anodic and cathodic Tafel slopes, while the polarization resistance, R_p, was calculated using the Stern-Geary equation, given by the Equation (7-1).

$$R_p = \frac{\beta a \beta c}{2.3 I corr(\beta a + \beta c)} \qquad (7\text{-}1)$$

Where, βa and βc are the anodic and cathodic Tafel slopes, respectively. The polarization resistance and the corrosion current density of the as-received Al substrate were found to be 22 ± 2 kΩ.cm^2 and 3.6 ± 1 μA/cm^2, respectively. These results are comparable with the existing

literature on the corrosion studies of Al [17]. Furthermore, the R_p and I_{corr} for the thin film of SA (Zr/SA =0) on the Al substrate were found to be 6 ± 22.2 kΩ.cm^2 and 7.2 ± 0.27 µA/cm^2, respectively. This decrease in the anticorrosion property could be due to the dissolution of the protective oxide layer under the effect of SA. Moreover, a similar tendency was observed for the thin film fabricated from the Zr/SA molar ratio of 1. In this case, the R_p and I_{corr} were found to be 22 ± 9 kΩ.cm^2 and 4.46 ± 2µA/cm^2, respectively. Further increase of Zr/SA molar ratio to 2 in the process, a larger R_p of 449 ± 36 kΩ.cm^2 and a lower I_{corr} of 0.41 ± 0.05 µA/cm^2 was observed. This can be correlated by the formation of a uniform ZrSA thin film on the Al substrate as shown in the SEM image (Figure 7.1 (d)). With a further increase in the Zr/SA molar ratio to 4, the R_p value was increased to 686 ± 178 kΩ.cm^2 and I_{corr} value was found to decrease 0.028 ± 0.01 µA/cm^2 for the ZrSA film coated Al substrate. This coating with excellent anti-corrosion properties is also associated with superhydrophobic properties. It was reported that the air trapped in the nanopores of superhydrophobic surfaces acts as a barrier and prevents the penetration of the corrosive ions to the Al substrate [34]. The R_p value increases to a maximum value of 778 ± 102 kΩ.cm^2 for the ZrSA thin film fabricated from the Zr/SA molar ratio of 8, while the corresponding I_{corr} was found to be 0.02 ± 0.01 µA/cm^2. The obtained R_p of this sample is 35 times higher than that obtained for the as-received Al substrate.

The corrosion parameters of the as-received Al substrate and the ZrSA thin film coated substrate are summarized in Table 7.2. The variations of R_p and I_{coor} with the Zr/SA molar ratio were illustrated in Figure 7.7 (b) and Figure 7.7 (c), respectively.

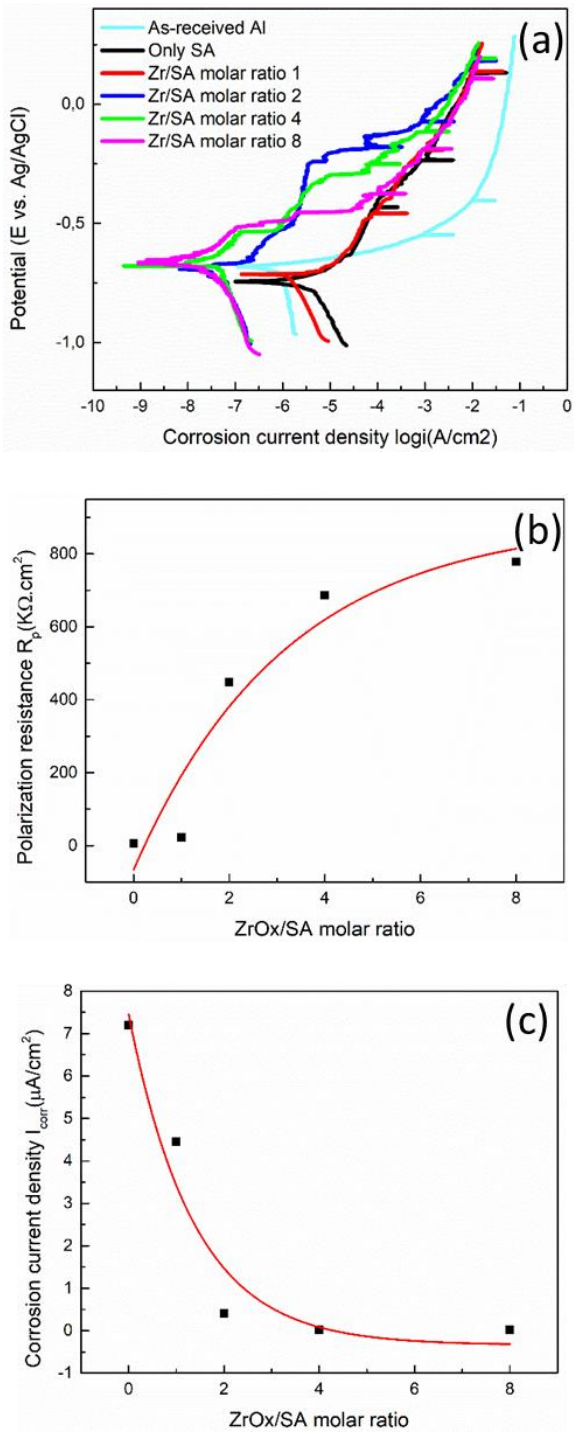

Figure 7.7: (a) Potentiodynamic polarization curves of as-received Al substrate and ZrSA thin films fabricated by electrodeposition process with the Zr/SA molar ratio of 0, 1, 2, 4, and 8. The variation of the (b)

polarization resistance R_p and the (c) corrosion current density I_{corr} with the Zr/SA molar ratio.

Table 7.2: The corrosion parameters and contact angle of as-received Al substrate and fabricated ZrSA thin films on Al substrate with the Zr-SA molar ratios of 0, 1, 2, 4 and 8.

Sample	Corrosion potential E_{corr} (mV)	Corrosion current density I_{corr} ($\mu A/cm^2$)	Polarization resistance R_p ($k\Omega.cm^2$)	CA (˚)
As-received Al	-610± 10	3.6 ± 1	22 ± 2	83 ± 2
Zr/SA=0 (Only SA)	-710 ± 41	7.2 ± 0.27	6 ± 22	100 ± 4
Zr/SA=1	-737 ± 14	4.46 ± 2	22 ± 9	107 ± 6
Zr/SA=2	-696 ± 34	0.41 ± 0.05	449 ± 36	114 ± 9
Zr/SA=4	-683 ± 34	0.028 ± 0.01	686 ± 178	165 ± 3
Zr/SA=8	-704 ± 31	0.02 ± 0.01	778 ± 102	151 ± 4

As a complementary electrochemical technique, the electrochemical impedance spectroscopy (EIS) was used to evaluate the corrosion resistance properties of the fabricated thin films deposited on Al substrates. Figure 7. (a) shows the Bode plot of the as-received Al substrate and the ZrSA superhydrophobic thin film fabricated from the Zr/SA molar ratio of 8. This plot presents the modulus of the impedance |Z| as a function of the frequency. At a high frequency of

1×10^4 Hz, the |Z| value of the as-received Al substrate and the ZrSA superhydrophobic thin film was found to be 21 $\Omega.cm^2$ and 8230 $\Omega.cm^2$, respectively. Similarly, at a low frequency of 1 Hz, the |Z| value for the as-received Al and the ZrSA superhydrophobic thin film was found to be 25 $k\Omega.cm^2$ and 578 $k\Omega.cm^2$, respectively. In the whole frequency range, the superhydrophobic thin film exhibited higher impedance compared to the as-received Al substrate. It has to mention that larger impedance values at lower frequencies are generally related to better corrosion protection [35,36].

Furthermore, in Figure 7. (b), the Bode phase plot of the ZrSA superhydrophobic thin film on Al substrate show two peaks corresponding to two different time constants. The time constant situated at the frequency of 10^4 Hz is related to thin film capacitance, and the time constant at a low frequency of 60 Hz is assigned to the capacitance of the double layer near the metallic substrate. This peak has been shifted toward lower frequency compared to as-received Al (90 Hz), indicating better anticorrosion properties with the fabrication of superhydrophobic thin film on Al.

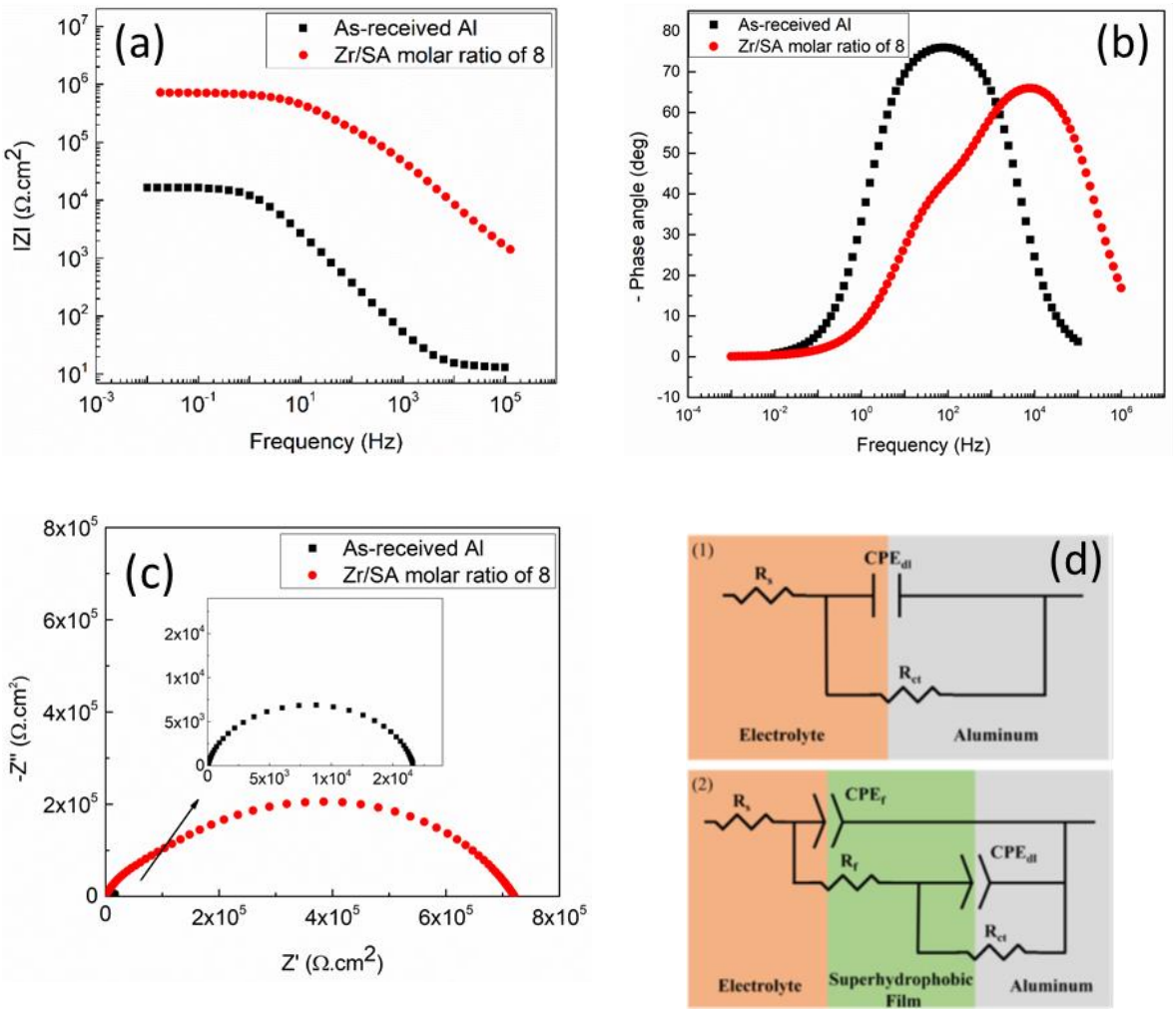

Figure 7.8: EIS measurements for the ZrSA thin films fabricated using the Zr/SA molar ratio of 8 and the as-received Al substrate. (a) The Nyquist plot, (b) Bode modulus, (c) Bode phase and (d) equivalent circuit of (d1) as-received Al substrate and (d2) superhydrophobic thin film.

Figure 7. (c) shows the Nyquist plots of the ZrSA thin films on Al substrate and the as-received Al substrate, which represents the impedance imaginary component Z″ as a function of the real component Z′. The Nyquist plot of the as-received Al is composed of a small semi-circle with a

diameter of 37 kΩ.cm^2, while the superhydrophobic thin film shows a large semi-circle with a diameter of 552 kΩ·cm^2. It has to mention that the diameter of the semi-circle in the Nyquist plots is related to the charge transfer resistance (R_{ct}), which is associated with the corrosion properties of the sample. A high R_{ct} value provides excellent anti-corrosion properties for the superhydrophobic thin film. . Figure 7. (d1) and (d2) represents the electrical equivalent circuits (EECs) of the as-received Al and the ZrSA superhydrophobic thin film. The fitted results obtained using the EECs are summarized in Table 7.3.

Table 7.3: Impedance parameters of the electrical equivalent circuits (EEC) and fitted EIS data of solution resistance (Rs), film resistance (Rf), charge transfer resistance (Rct), constant phase element (CPE).

Sample	R_s ($\Omega \cdot cm^2$)	CPE_f		R_f ($k\Omega \cdot cm^2$)	CPE_{dl}		R_{ct} ($k\Omega \cdot cm^2$)
		Y_f ($\Omega^{-1} \cdot s^n \cdot cm^{-2}$)	n_f		Y_f ($\Omega^{-1} \cdot s^n \cdot cm^{-2}$)	n_f	
Aluminum substrate	22	-	-	-	2.3×10^{-6}	0.9	37
Superhydrophobic thin film	597	1.6×10^{-8}	0.8	1.6×10^{2}	8.6×10^{-8}	0.6	552

The inhibition efficiency (η) of ZrSA superhydrophobic thin film was evaluated using the Equation (7-2).

$$\eta(\%) = \frac{R_{ct} - R_{ct0}}{R_{ct}} \times 100 \qquad (7\text{-}2)$$

Where, R_{ct} is the charge transfer resistance of ZrSA superhydrophobic thin film, and R_{ct0} represents the charge transfer resistance of the Al substrate. In this case, the inhibition efficiency η (%) of the superhydrophobic thin film is 93 % by taking the values of R_{ct} and R_{ct0} of 552 kΩ·and 37kΩ·cm^2 respectively. This result indicates that ZrSA thin film exhibits excellent anti-corrosion properties.

7.4 **Conclusion**

In the current study, Zr-based superhydrophobic thin films were successfully fabricated on laminated AA6061-T6 aluminum alloy substrates using the electrodeposition process. The SEM images of the Zr-based thin film coated substrate show the presence of micro-nano patterned surface. The ATR-FTIR confirms the presence of low surface energy compounds on the ZrSA thin film coated substrates. The synthesized Zr-based superhydrophobic thin films provide much higher water contact angle and polarization resistance as compare to as-received aluminum substrate. The maximum corrosion protection efficiency of 93 % was achieved for Zr-based superhydrophobic thin films. The finding of this study shows good performance of Zr-based superhydrophobic thin films in corrosion protection of aluminum which is beneficial to expand the application of Al and its alloys in a variety of practical fields.

References

[1] D.J. Lee, H.M. Kim, Y.S. Song, J.R. Youn, Water Droplet Bouncing and Superhydrophobicity Induced by Multiscale Hierarchical Nanostructures, ACS Nano. 6 (2012) 7656–7664.

[2] Z. Chen, L. Hao, A. Chen, Q. Song, C. Chen, A rapid one-step process for fabrication of superhydrophobic surface by electrodeposition method, Electrochim. Acta. 59 (2012) 168–171.

[3] M. Alonso Frank, A.R. Boccaccini, S. Virtanen, A facile and scalable method to produce superhydrophobic stainless steel surface, Appl. Surf. Sci. 311 (2014) 753–757.

[4] W. Tong, D. Xiong, N. Wang, C. Yan, T. Tian, Green and timesaving fabrication of a superhydrophobic surface and its application to anti-icing, self-cleaning and oil-water separation, Surf. Coatings Technol. 352 (2018) 609–618.

[5] J. Kuang, Z. Ba, Z. Li, Y. Jia, Z. Wang, Fabrication of a superhydrophobic Mg-Mn layered double hydroxides coating on pure magnesium and its corrosion resistance, Surf. Coatings Technol. 361 (2019) 75–82.

[6] H. Li, S. Yu, J. Hu, X. Yin, Modifier-free fabrication of durable superhydrophobic electrodeposited Cu-Zn coating on steel substrate with self-cleaning, anti-corrosion and anti-scaling properties, Appl. Surf. Sci. (2019).

[7] O. Rius-Ayra, R. Castellote-Alvarez, A.M. Escobar, N. Llorca-Isern, Robust and superhydrophobic coating highly resistant to wear and efficient in water/oil separation, Surf. Coatings Technol. 364 (2019) 330–340.

[8] Q. Zhao, T. Tang, F. Wang, Fabrication of Superhydrophobic AA5052 Aluminum Alloy Surface with Improved Corrosion Resistance and Self Cleaning Property, Coatings. 8 (2018) 390.

[9] C.J. Donahue, J.A. Exline, Anodizing and Coloring Aluminum Alloys, J. Chem. Educ. 91 (2014) 711–715.

[10] Z. Li, N. Li, D. Wang, D. Ouyang, L. Liu, Low temperature deformation behavior of an electromagnetically bulged 5052 aluminum alloy, Sci. Rep. 6 (2016) 29973.

[11] M. Liang, R. Melchers, I. Chaves, Corrosion and pitting of 6060 series aluminium after 2 years exposure in seawater splash, tidal and immersion zones, Corros. Sci. (2018).

[12] P.E. Hintze, L.M. Calle, Electrochemical properties and corrosion protection of organosilane self-assembled monolayers on aluminum 2024-T3, Electrochim. Acta. 51 (2006) 1761–1766.

[13] P.M. Barkhudarov, P.B. Shah, E.B. Watkins, D.A. Doshi, C.J. Brinker, J. Majewski, Corrosion inhibition using superhydrophobic films, Corros. Sci. 50 (2008) 897–902.

[14] Y. Huang, D.K. Sarkar, X. Grant Chen, Superhydrophobic aluminum alloy surfaces prepared by chemical etching process and their corrosion resistance properties, Appl. Surf. Sci. 356 (2015) 1012–1024.

[15] X. Li, Q. Zhang, Z. Guo, T. Shi, J. Yu, M. Tang, X. Huang, Fabrication of superhydrophobic surface with improved corrosion inhibition on 6061 aluminum alloy substrate, Appl. Surf. Sci. 342 (2015) 76–83.

[16] R.A. Alawajji, G.K. Kannarpady, A.S. Biris, Fabrication of transparent superhydrophobic

polytetrafluoroethylene coating, Appl. Surf. Sci. 444 (2018) 208–215.

[17] J. Xiong, D.K. Sarkar, X.-G. Chen, Superhydrophobic honeycomb-like cobalt stearate thin films on aluminum with excellent anti-corrosion properties, Appl. Surf. Sci. 407 (2017) 361–370.

[18] Y. Huang, D.K. Sarkar, X.-G. Chen, Superhydrophobic nanostructured ZnO thin films on aluminum alloy substrates by electrophoretic deposition process, Appl. Surf. Sci. 327 (2015) 327–334.

[19] N. Xu, D.K. Sarkar, X. Grant Chen, H. Zhang, W. Tong, Superhydrophobic copper stearate/copper oxide thin films by a simple one-step electrochemical process and their corrosion resistance properties, RSC Adv. 6 (2016) 35466–35478.

[20] N. Xu, D.K. Sarkar, X.-G. Chen, W.P. Tong, Corrosion performance of superhydrophobic nickel stearate/nickel hydroxide thin films on aluminum alloy by a simple one-step electrodeposition process, Surf. Coatings Technol. 302 (2016) 173–184.

[21] J.D. Brassard, D.K. Sarkar, J. Perron, A. Audibert-Hayet, D. Melot, Nano-micro structured superhydrophobic zinc coating on steel for prevention of corrosion and ice adhesion, J. Colloid Interface Sci. 447 (2015) 240–247.

[22] A.K. Singh, J.K. Singh, Fabrication of zirconia based durable superhydrophobic-superoleophilic fabrics using non fluorinated materials for oil-water separation and water purification, RSC Adv. 6 (2016) 103632–103640.

[23] Y. Fan, Y. He, P. Luo, X. Chen, Z. Yu, M. Li, Facile way in building superhydrophobic zirconium surface for controllable water-oil separation, Mater. Lett. 188 (2017) 115–118.

[24] I. Das, G. De, Zirconia based superhydrophobic coatings on cotton fabrics exhibiting excellent durability for versatile use, Sci. Rep. 5 (2016) 18503.

[25] H. Li, K. Liang, L. Mei, S. Gu, S. Wang, Corrosion protection of mild steel by zirconia sol-gel coatings, J. Mater. Sci. Lett. 20 (2001) 1081–1083.

[26] Q.P. Li, Z.Q. Yan, Q. Xu, B. Zhang, S. Sun, J.G. Liu, C.W. Yan, A high-performance Ti-Zr Based Chromium-Free Conversion Coating on 2024 Aluminum Alloy, Int. J. Electrochem. Sci. 1112 (2016) 10675–1068939.

[27] S. Gheytani, Y. Liang, Y. Jing, J.Q. Xu, Y. Yao, Chromate conversion coated aluminium as a light-weight and corrosion-resistant current collector for aqueous lithium-ion batteries, J. Mater. Chem. A. 4 (2016) 395–399.

[28] J. Tsibouklis, P. Graham, P.J. Eaton, J.R. Smith, T.G. Nevell, J.D. Smart, R.J. Ewen, Poly(perfluoroalkyl methacrylate) Film Structures: Surface Organization Phenomena, Surface Energy Determinations, and Force of Adhesion Measurements, Macromolecules. 33 (2000) 8460–8465.

[29] M. Kadlečková, A. Minařík, P. Smolka, A. Mráček, E. Wrzecionko, L. Novák, L. Musilová, R. Gajdošík, Preparation of Textured Surfaces on Aluminum-Alloy Substrates., Mater. (Basel, Switzerland). 12 (2018).

[30] G. Fonder, F. Laffineur, J. Delhalle, Z. Mekhalif, Alkanethiol-oxidized copper interface: The critical influence of concentration, J. Colloid Interface Sci. 326 (2008) 333–338.

[31] J. Tan, J. Hao, Z. An, C. Liu, Simple Fabrication of Superhydrophobic Nickel Surface on Steel Substrate via Electrodeposition, Int. J. Electrochem. Sci. 12 (2017) 40–49.

[32] B. Li, H. Mou, Y. Li, Y. Ni, Synthesis and thermal decomposition behavior of zircoaluminate coupling agents, Ind. Eng. Chem. Res. 52 (2013) 11980–11987.

[33] W. Li, X. Liu, A. Huang, P.K. Chu, Structure and properties of zirconia (ZrO 2) films fabricated by plasma-assisted cathodic arc deposition, J. Phys. D Appl. Phys. 40 (2007) 2293–2299.

[34] B. Zhang, J. Li, X. Zhao, X. Hu, L. Yang, N. Wang, Y. Li, B. Hou, Biomimetic one step fabrication of manganese stearate superhydrophobic surface as an efficient barrier against marine corrosion and Chlorella vulgaris-induced biofouling, Chem. Eng. J. 306 (2016) 441–451.

[35] R.L. Twite, G.P. Bierwagen, Review of alternatives to chromate for corrosion protection of aluminum aerospace alloys, Prog. Org. Coatings. 33 (1998) 91–100.

[36] P.J. Denissen, S.J. Garcia, Reducing subjectivity in EIS interpretation of corrosion and corrosion inhibition processes by in-situ optical analysis, Electrochim. Acta. 293 (2019) 514–524.

CHAPTER 8

CONCLUSIONS AND FUTURE RECOMMENDATIONS

CHAPTER 8 : CONCLUSIONS AND FUTURE RECOMMENDATIONS

Conclusions

The pursuit to find chromate-free alternatives has led to the development of several thin films and inhibitors that offer a good corrosion protection for aluminum. Therefore, the objective of this work was to investigate the corrosion properties of selected chromate-free thin films and inhibitors on laminated AA6061-T6 aluminum alloy.

In the first part of the thesis, sodium silicate thin films were fabricated on laminated AA6061-T6 aluminum alloy substrates by a simple ultrasonic dip-coating process. ATR-FTIR confirms the presence of Si-O-Si bond with an absorption peak at 1207 cm^{-1} with possible Si-O-Na bond at 943 cm^{-1}. The complementary study by EDS analysis supports the compositions having the elemental percentage of Na, Si, and O of 3.30, 24.48 and 72.22, respectively. The corrosion resistance properties of sodium silicate thin film analyzed by Tafel plots provided the polarization resistance R_p of 593 ± 32 $k\Omega.cm^2$ compared to 10 $k\Omega.cm^2$ for the as-received Al substrate. On the other hand, the corresponding corrosion current density I_{corr} is found to be 0.05 ± 0.01 $k\Omega.cm^{-2}$ for the sodium silicate thin film compared to 10.6 ± 3.3 $k\Omega.cm^{-2}$ for the as-received Al substrate. The obtained results show the ability of sodium silicate thin films to protect Al against corrosion.

In the second part of the thesis, the corrosion properties of laminated AA6061-T6 aluminum alloy were studied by modifying the corrosive electrolyte of NaCl with water-soluble compounds as the inhibitor. Three inhibitors such as sodium silicate (Na_2SiO_3), manganese sulfate monohydrate ($MnSO_4.H_2O$) and ammonium metavanadate (NH_4VO_3) were tested. The R_p of the Al substrate immersed in 0.1 M NaCl solution was found to be 13 $k\Omega.cm^2$. In comparison, the R_p of the Al substrate immersed in 0.1 M NaCl in the presence of the inhibitors of Na2SiO3,

$Na_2SiO_3/MnSO_4.H_2O$, and Na_2SiO_3/NH_4VO_3 was found to be 100, 133 and 679 $k\Omega.cm^2$, respectively. The best result of inhibition was obtained when the mixture of the three inhibitors was used with the Rp of 722 $k\Omega.cm^2$. Subsequently, the image analysis was carried out on the SEM images of the corroded Al substrates with and without inhibitors. The maximum percentage of the corroded area was found to be 5.7 % for Al substrate, and that to be reduced to 0.06 % in the presence of the mixture of the three inhibitors. The inhibition efficiency (η) of the inhibitors was calculated from the corrosion current density, which was found to be 87.5, 92, and 99.5 % for Na_2SiO_3, $Na_2SiO_3/MnSO_4.H_2O$, and Na_2SiO_3/NH_4VO_3, respectively. However, a maximum Efficiency (η) value of 99.9 % was obtained in the presence of the mixed inhibitors of Na_2SiO_3 $/MnSO_4.H_2O$ $/NH_4VO_3$. The synergetic effects between the three inhibitors were studied and the results illustrated that the combination of Na_2SiO_3, $MnSO_4.H_2O$, and NH_4VO_3 provided the best corrosion inhibition properties for Al in aqueous NaCl environments.

Furthermore, the third part of this work deals with the fabrication of zirconium silicate thin films by sol-gel process for the improvement of the corrosion resistance properties of laminated AA6061-T6 aluminum alloy. The corrosion analysis of this part was carried out in the same way as performed in the first part. After the aging time of the sol of 72 hours, the polarization resistance R_p of the thin film was found to be 446 $k\Omega.cm^2$ compared to 10 $k\Omega.cm^2$ for as-received Al substrate. On the other hand, the corrosion current density I_{corr} is found to be 0.06 $k\Omega.cm^{-2}$ for the sodium silicate thin film compared to 10.6 $k\Omega.cm^{-2}$ for the as-received Al substrate. The corrosion protection efficiency was found to 97 % with the increase of the aging time of the sol to 72 h. The SEM analysis shows the formation of zirconium silicate micro grains with uniform coverage area on the metallic substrate. Finally, the ATR-FTIR studies suggest that the increase of the sol aging time increases the thickness of the thin films, which improves their performance.

In the last part of this work, the superhydrophobic zirconium-stearate (ZrSA) thin films were fabricated on laminated AA6061-T6 aluminum alloy substrates using the electrodeposition process. The ATR-FTIR analysis confirms the presence of low surface energy radicals of $-CH_2$ and $-CH_3$ in the ZrSA thin films. Further, the SEM analysis shows the presence of a micro-nano structured features. The combination of this morphology and the low surface energy makes ZrSA superhydrophobic. The polarization resistance, R_p, of the ZrSA thin film was found to be 778 ± 102 $k\Omega.cm^2$ compared to 22 ± 2 $k\Omega.cm^2$ for the as-received Al substrate. The improved corrosion protection properties with the increase of the Zr/SA molar ratio could be explained by the increase of the thickness of the thin films. The maximum corrosion protection efficiency of 97 % was achieved for Zr-based superhydrophobic thin films, which is beneficial to expand the application of Al and its alloys in a variety of practical fields.

Table 8.1 summarizes the corrosion parameters of the studied thin films and inhibitors. The polarization resistances (R_p) in the concentration of 0.6 M of NaCl were found to be 593 $k\Omega.cm^2$, 446 $k\Omega.cm^2$ and 778 $k\Omega.cm^2$ for sodium silicate, zirconium silicate and zirconium-stearate thin films, respectively. On the other hand, the polarization resistance R_p in the concentration of 0.1 M of NaCl was found to be 722 $k\Omega.cm^2$ for inhibitors.

Table 8.1: The corrosion current density $I_{corr,}$ the polarization resistance R_p, and charge transfer resistance R_{ct} of as-received Al, sodium silicate thin film on Al by ultrasonically dip-coating process with the concentration of 1M, Na_2SiO_3, Na_2SiO_3/ $MnSO_4.H_2O$, Na_2SiO_3 /NH_4VO_3, and Na_2SiO_3 /$MnSO_4.H_2O$ /NH_4VO_3 as inhibitors for Al, zirconium silicate thin films on Al by sol-gel process after the aging time of sol of 72 h, and the ZrSA thin films by electrodeposition process with the Zr/SA molar ratio of 8. It is to mention that the electrochemical tests were performed in 0.6 M and 0.1 M NaCl solution for thin films and inhibitors, respectively.

Sample	Corrosion current density I_{corr} ($\mu A.cm^{-2}$)	Polarization rsistance R_p ($k\Omega.cm^2$)	Corrosion efficiency η (%)
As-received Al	10.6	10	-
Sodium silicate thin films	0.05	593	99
Zirconium silicate thin films	0.06	446	97
Zirconium-stearate (ZrSA) thin films	0.02	778	97
Inhibitors	0.002	722	99

Although the results of this work demonstrated that the selected chromate-free thin films provide good corrosion protection for aluminum under laboratory conditions, before proceeding to

industrial applications, the durability of the thin films with respect to prolonged exposure to corrosive environment and their adhesion on the substrates, remains to be evaluated.

Future recommendations

The following part provides a summary of the possible work that could be accomplished in order to develop a deeper understanding on the different coatings and inhibitors studied in this work.

In this work, sodium silicate thin films were prepared using ultrasonic dip-coating process in chapter 4. It was reported in the literature that the ultrasonication process enhances the density of some coatings. Therefore, a deeper study on the density of the sodium silicate coatings under ultrasonication should be involved.

Furthermore, chapter 5 of this work discussed the behavior of sodium silicate (Na_2SiO_3), manganese sulfate monohydrate ($MnSO_4.H_2O$) and ammonium metavanadate (NH_4VO_3) as corrosion inhibitors for aluminum. To improve better understanding, the inhibitors could be tested in different pH and temperature conditions. Furthermore, the aeration during the inhibition experiments was also reported to be an important factor that could influence the efficiency of the inhibitors.

In chapter 6, zirconium silicate thin films provide better corrosion properties with the increase of the sol aging time. Therefore, it will be interesting to analyze the effect of other parameters on the performance of the fabricated thin films, such as the effect of the heat treatment, the number of layers, and the spin coating speed.

Finally, the zirconium-stearate thin films fabricated by electrodeposition process in Chapter 7 of this work exhibits excellent corrosion protection properties. However, their adhesion on the aluminum substrates needs to be improved. One of the suggested solutions is the use of ZrSA extracted powder with industrial coatings, such as Ultra Ever Dry (UED) presented in Appendix

B. Nevertheless, the chemical composition of UED remains confidential, wish makes the understanding of their interaction with ZrSA difficult. Therefore, the development of new methods or additives to improve the adhesion of ZrSA thin films on aluminum remains a challenge.

LIST OF PUBLICATIONS OF CANDIDATE

Journal articles

- Redouane Farid, Karthikeyan Rajan, Dilip Kumar Sarkar, Enhanced corrosion protection of aluminum by ultrasonically dip coated sodium silicate thin films, Surface and Coating Technology, **374** (2019), 355-361.

- Redouane Farid, Dilip Kumar Sarkar, Debasis De, Facile electrodeposition process of zirconium-based superhydrophobic thin films on aluminum, **accepted** by The International Journal of Wettability Science & Technology (IJWST), (2019).

- Redouane Farid, Dilip Kumar Sarkar, Debasis De, Evaluation of the corrosion inhibition performance of non-chromate corrosion inhibitors for aluminum alloy, Submitted to metals, (2019), **under revision.**

- Redouane Farid, Dilip Kumar Sarkar, Debasis De, Zirconium silicate thin films by sol-gel process for corrosion protection of aluminum, (2019), **In preparation.**

Conference papers

- Redouane Farid, Dilip Kumar Sarkar, Sofiene Amira, David Levasseur, Development of Superhydrophobic thin films on aluminum as a corrosion barrier, 6th International Conference & Exhibition on Advanced & Nano Materials, (2018), Quebec City, Canada.

Conference attended (Oral and poster presentations)

- Redouane Farid and Dilip Kumar Sarkar. Étude du comportement anticorrosion des revêtements superhydrophobes sur les alliages de l'aluminium. Oral presentation at 87th ACFAS Congress, 9th may, (2018), Saguenay, Canada.

- Redouane Farid, Dilip Kumar Sarkar, Sofiene Amira, David Levasseur, Zirconium-based thin films for the corrosion protection of aluminum. Oral presentation at La Journée des étudiants du REGAL, (2018), Montreal, Canada.

- Redouane Farid, Dilip. K. Sarkar, Sofiene Amira, David Levasseur, Development of mechanically durable ecologic and corrosion resistance non-chromate coatings for aluminum, Poster presentation at Journée des étudiants du REGAL, 18-19 Juin, (2018), Montreal, Canada.

- Redouane Farid, Dilip. K. Sarkar, Sofiene Amira, David Levasseur, Development of Superhydrophobic thin films on aluminum as a corrosion barrier. Paper presented at the 6th International Conference & Exhibition on Advanced & Nano Materials, 6-8 August, (2018), Quebec City, Canada.

APPENDIX A

A.1. EDS spectra of region 1 and 2 in the showed in Chapter 4, Figure. 4.3.

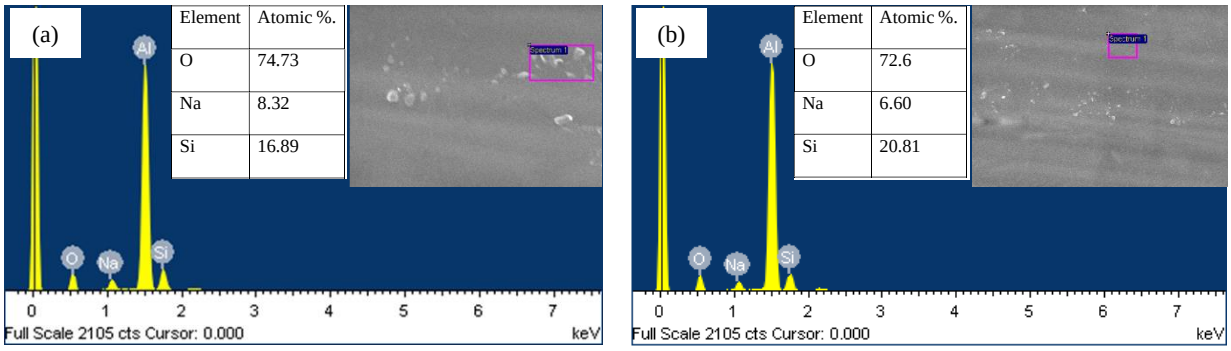

Figure A.1: The EDS spectrum of sodium silicate thin film on the aluminum substrate prepared from 1 M solution. (a) particles, (b) flat area.

A.2. Nucleation sites of sodium silicate on the aluminum substrate

Figure A2 shows that two circles, A and B, are drawn around two intermetallic particles. Apart from the intermetallic particle, several sodium silicate particles are visible inside the circle A. There is no nucleation of sodium silicate on the intermetallic particle in the circle A. On the other hand, in circle B, two distinct sodium silicate particles are visible on the intermetallic particle and a few just beside the intermetallic particle. This observation shows that there are no specific nucleation sites for the sodium silicate particles on the A6061 Al substrate.

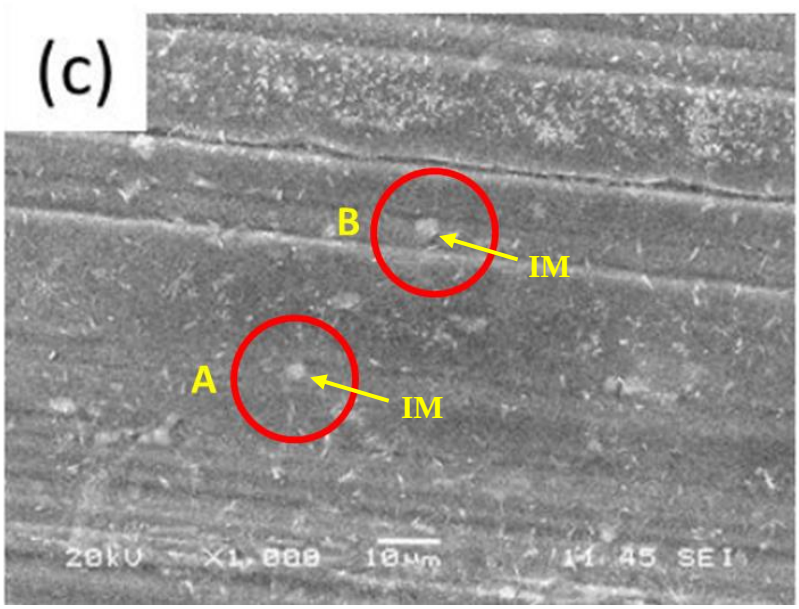

Figure A.2: SEM image of sodium silicate thin film fabricated from the solution concentration of M. A and B are two circles surrounding two intermetallic phases.

APPENDIX B

B.1. Effect of electrodeposition time on Zr-SA thin films

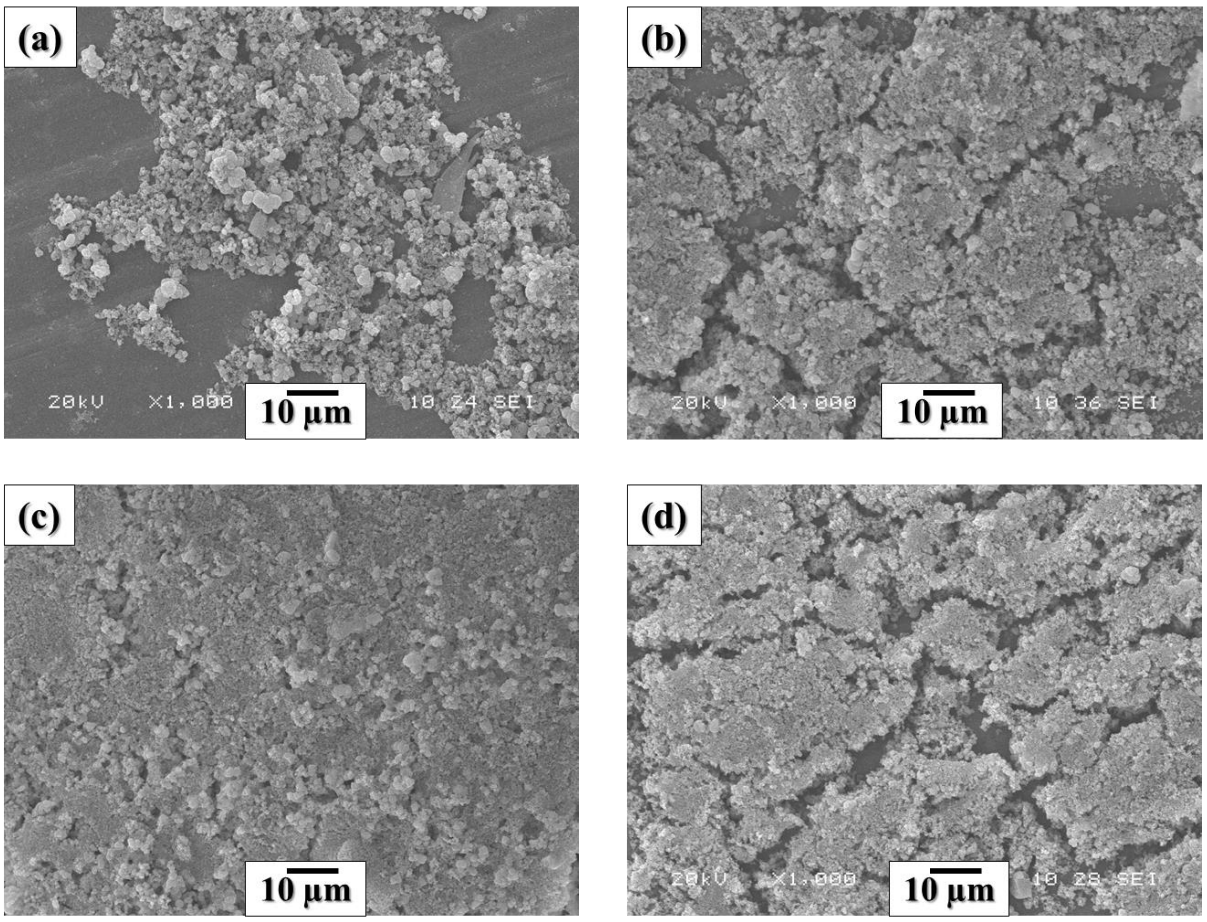

Figure B.1: SEM images of ZrSA thin films on Al substrates with the electrodeposition times of (a) 1, (b) 5, (c) 10, and (d) 15 minutes.

B.2.Study of the durability of thin films fabricated from the mixture of Zr-SA powder and UED top coating

A volume of 10 mL of top coat of ultra ever dry (UED) solution was mixed with 0, 0.01, 0.05, 0.1, and 0.15 g of zirconium-stearic acid (Zr-SA) powder. The obtained solutions of Zr-SA-UED were used to coat clean Al substrates by a spin coating process. After drying, microcracks were created on the thin films surface, then the samples were immersed in 3.5 wt.% NaCl solution as shown in Figure B1.

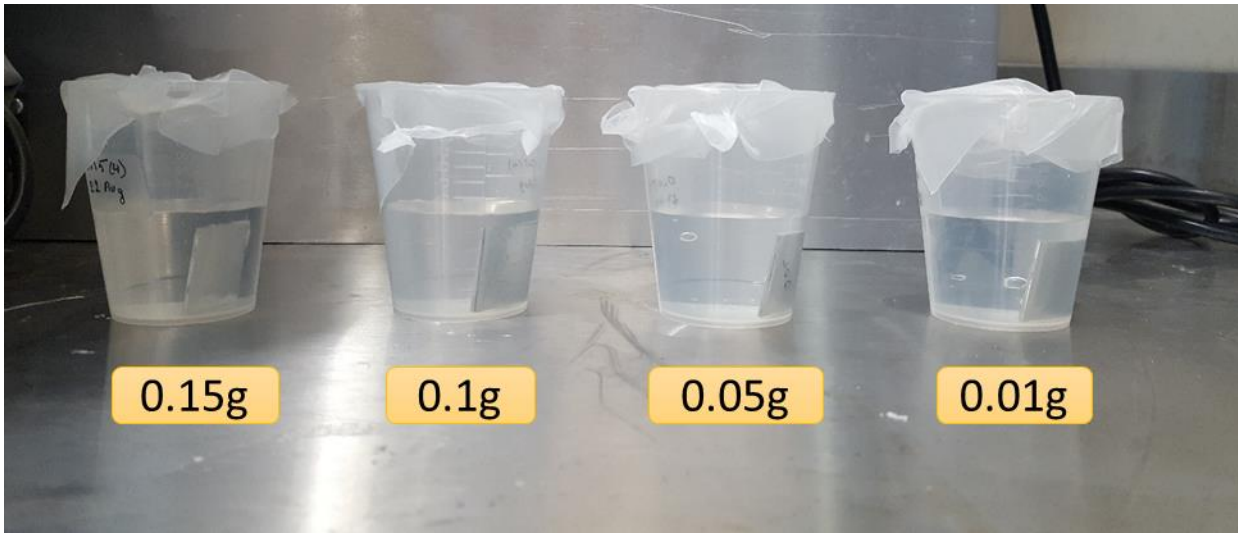

Figure B.2: Zr-SA powder in 10 mL of UED top coating solution deposited on Al substrates by spin coating process with the Zr-SA powder weight of 0.01, 0.05, 0.1, and 0.15 g.

The evolution of the width of the microcracks was studied using optical microscopy for 15 days, and the results are presented in Figure B3 and Figure B4.

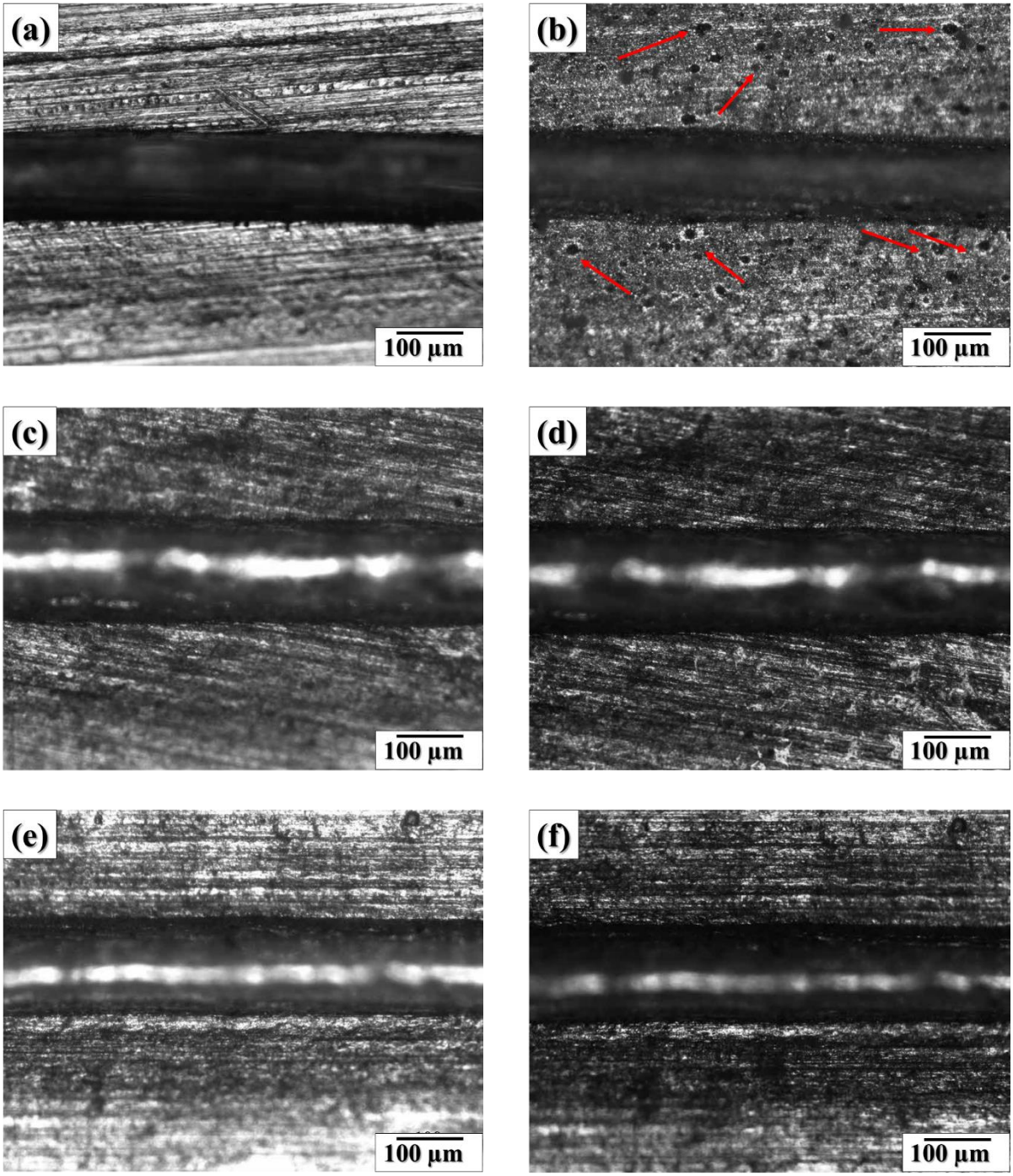
(a)
100 µm
(b)
100 µm
(c)
100 µm
(d)
100 µm
(e)
100 µm
(f)
100 µm

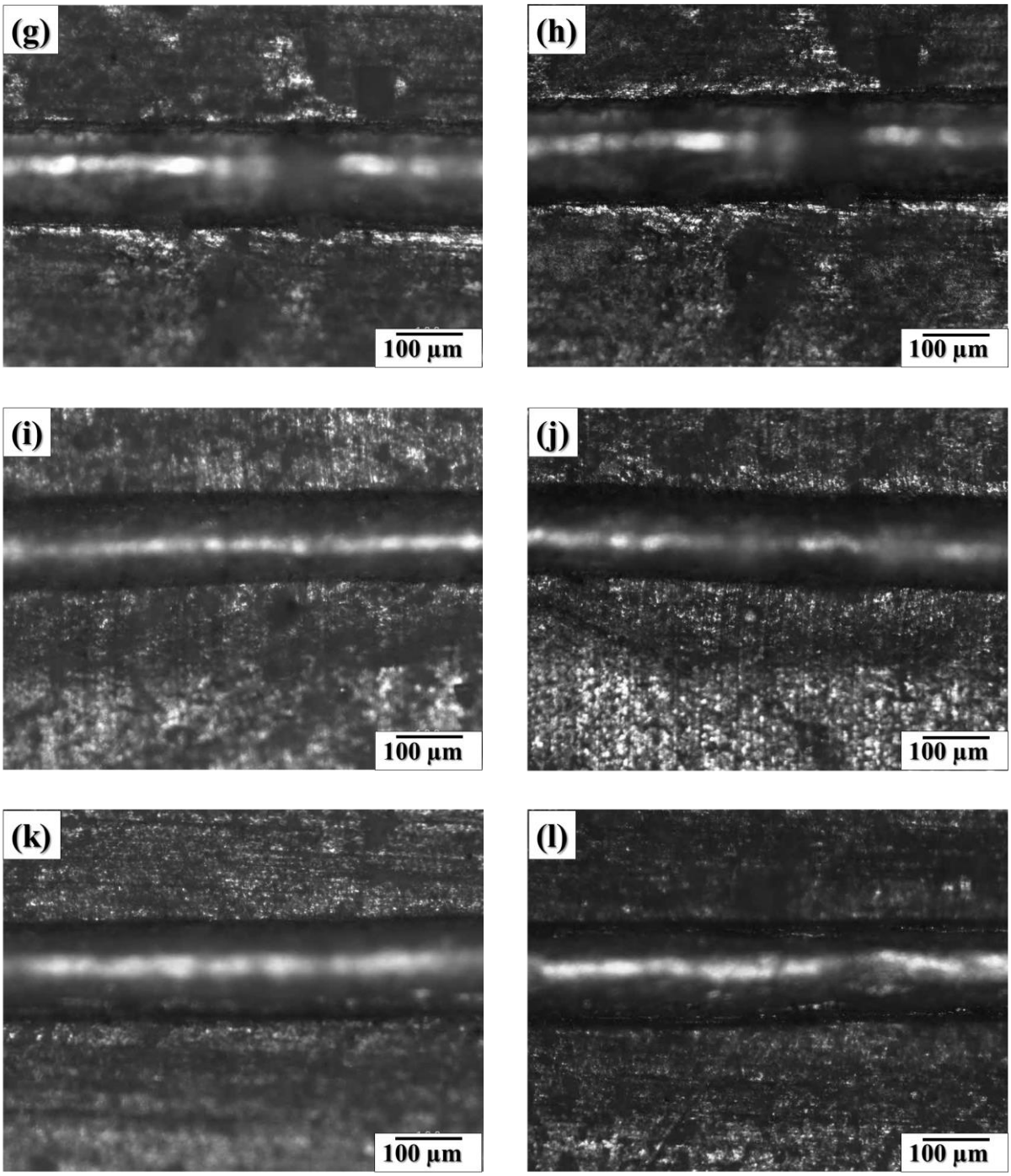

Figure B.3: Optical images of scratched regions of as-received Al substrate (a) before and (b) after immersion in 3.5 wt.% NaCl for 15 days. (c-j) images represents the Zr-SA powder in 10 mL of UED top coating solution deposited on Al substrates by spin coating process with the Zr-SA powder weight of (c,d) 0, (e,f) 0.01, (g,h) 0.05, (i,j) 0.1, and (k,l) 0.15. Left images represent

the samples before immersion, and right images represent samples after immersion in 3.5 wt.% NaCl solution for 15 days.

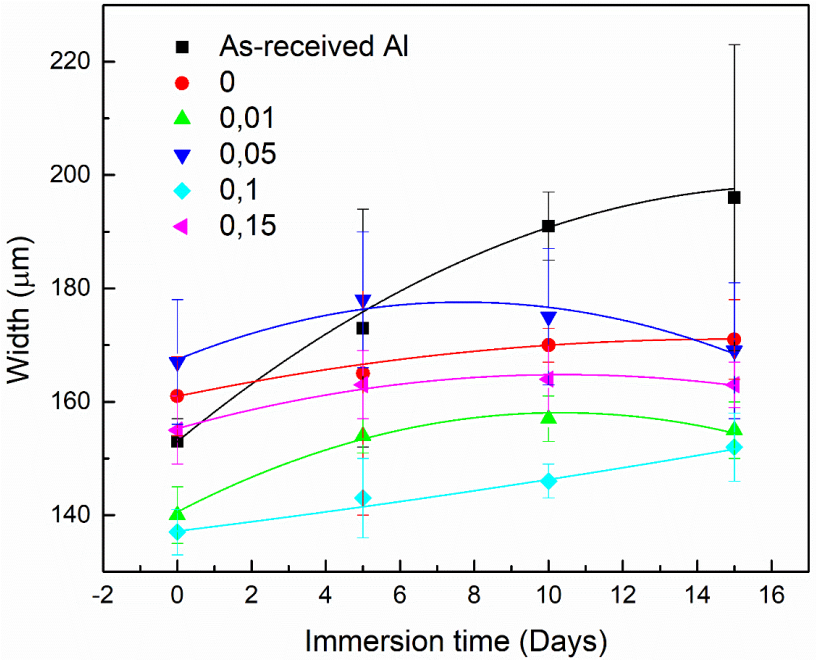

Figure B.4: The variation of the crack width with the immersion time of Zr-SA-UED thin films in 3.5 wt.% NaCl solution.